Title

Precipitation Cluster Distributions: Current Climate Storm Statistics and Projected Changes Under Global Warming

Author

Quinn, Kevin Martin

Publication Date

2016

Peer reviewed|Thesis/dissertation

UNIVERSITY OF CALIFORNIA

Los Angeles

Precipitation Cluster Distributions: Current Climate Storm Statistics and Projected Changes Under Global Warming

A dissertation submitted in partial satisfaction of the
requirements for the degree of Doctor of Philosophy
in Atmospheric and Oceanic Sciences

by

Kevin Martin Quinn

2016

ABSTRACT OF THE DISSERTATION

Precipitation Cluster Distributions: Current Climate Storm Statistics and Projected Changes Under Global Warming

by

Kevin Martin Quinn

Doctor of Philosophy in Atmospheric and Oceanic Sciences
University of California, Los Angeles, 2016
Professor J. David Neelin, Chair

The total amount of precipitation integrated across a precipitation cluster (contiguous precipitating grid cells exceeding a minimum rain rate) is a useful measure of the aggregate size of the disturbance, expressed as the rate of water mass lost or latent heat released, i.e. the power of the disturbance. Probability distributions of cluster power are examined during boreal summer (May-September) and winter (January-March) using satellite-retrieved rain rates from the Tropical Rainfall Measuring Mission (TRMM) 3B42 and Special Sensor Microwave Imager and Sounder (SSM/I and SSMIS) programs, model output from the High Resolution Atmospheric Model (HIRAM, roughly 0.25- 0.5^0 resolution), seven 1- 2° resolution members of the Coupled Model Intercomparison Project Phase 5 (CMIP5) experiment, and National Center for Atmospheric Research Large Ensemble (NCAR LENS). Spatial distributions of precipitation-weighted centroids are also investigated in observations (TRMM-3B42) and climate models during winter as a metric for changes in mid-latitude storm tracks. Observed probability distributions for both seasons are scale-free from the smallest clusters up to a cutoff scale at high

cluster power, after which the probability density drops rapidly. When low rain rates are excluded by choosing a minimum rain rate threshold in defining clusters, the models accurately reproduce observed cluster power statistics and winter storm tracks. Changes in behavior in the tail of the distribution, above the cutoff, are important for impacts since these quantify the frequency of the most powerful storms. End-of-century cluster power distributions and storm track locations are investigated in these models under a "business as usual" global warming scenario. The probability of high cluster power events increases by end-of-century across all models, by up to an order of magnitude for the highest-power events for which statistics can be computed. For the three models in the suite with continuous time series of high resolution output, there is substantial variability on when these probability increases for the most powerful precipitation clusters become detectable, ranging from detectable within the observational period to statistically significant trends emerging only after 2050. A similar analysis of National Centers for Environmental Prediction (NCEP) Reanalysis 2 and SSM/I-SSMIS rain rate retrievals in the recent observational record does not yield reliable evidence of trends in high-power cluster probabilities at this time. Large impacts to mid-latitude storm tracks are projected over the West Coast and eastern North America, with no less than 8 of the 9 models examined showing large increases by end-of-century in the probability density of the most powerful storms, ranging up to a factor of 6.5 in the highest range bin for which historical statistics are computed. However, within these regional domains, there is considerable variation among models in pinpointing exactly where the largest increases will occur.

The dissertation of Kevin Martin Quinn is approved.

Alexander Dean Hall

Jasper F. Kok

Dennis P. Lettenmaier

J. David Neelin, Committee Chair

University of California, Los Angeles

2016

Table of Contents

List of Figures

List of Tables

Acknowledgments

The journey towards earning a PhD has been like nothing else I have done. To pursue my dream of earning a PhD, I left my previous job in the middle of a recession…so to my wife Katie who has stood by my side and been the breadwinner while I have been in school, thank you, as I definitely would not be here today without the love and support of you and family. To my son Connor, born 3 months after I began my PhD program…thank you for being an absolute joy and inspiration to me.

I must also thank my adviser and coauthor, David Neelin, for his infinite patience, support, and mentorship. I also want to thank my research group and office mates, for their comraderie and help along the way: Neil Berg, Daniel Walton, Marla Schwartz, Ross Cheung, Ling Qi, Mei Gao, Rose Tseng, Omar Nava, David Gonzales, Kathleen Schiro, Yi-Hung Kuo, Xuan Ji, Baird Langenbrunner, and Katrina Hales-Garcia. And I must extend my appreciation to my committee as well: Alex Hall, Jasper Kok, and Dennis Lettenmaier. I am also very grateful for the assistance Joyce Meyerson has provided along the way.

Finally, Chapters 2 and 3 have been submitted as two separate papers to Journal of Climate for publication, and are currently under peer review. This research has been supported in part by the National Science Foundation (NSF Grant AGS-434 1540518) and National Oceanic and Atmospheric Administration (NOAA Grants 435 NA14OAR4310274 and NA15OAR4310097).

Kevin Martin Quinn

2009 **M.S. Meteorology**
The Naval Postgraduate School

2003 **B.S. Atmospheric Science**
Cornell University

Professional Experience

UCLA Graduate Student Researcher	2013-2016
National Weather Service	2010-2013
US Air Force/California Air National Guard	2003-2016

Fellowships and Awards

UCLA Graduate Dean's Scholar Award	2013-2015
UCLA AOS Fellowship	2013
US Air Force Commendation Medal, 1 Oak Leaf Cluster	2006 and 2010
US Army Commendation Medal	2007
US Air Force ROTC Scholarship	1999-2003

Publications

Quinn, K. and J. D. Neelin, 2016: Distributions of tropical precipitation cluster power and their changes under global warming: Part I. (Under peer review by Journal of Climate)

Quinn, K. and J. D. Neelin, 2016: Distributions of tropical precipitation cluster power and their changes under global warming: Part II. (Under peer review by Journal of Climate)

1 General Introduction

Metrics of extreme precipitation intensity are projected to increase across all emissions pathways in the Coupled Model Intercomparison Project Phase 3 (CMIP3) and CMIP5 experiments (Tebaldi et al. 2006; Kharin et al. 2007, 2013; Sillmann et al. 2013). However, at a global scale, uncertainties in changes to extreme precipitation appear in both observational studies (e.g., Easterling et al. 2000; Alexander et al. 2006; Kharin et al. 2007, 2013; Lenderink and van Meijgaard 2008; Allan et al. 2010) and modeling studies (e.g., Tebaldi et al. 2006; Kharin et al. 2007, 2013; Allan and Soden 2008; Allan et al. 2010; Sillmann et al. 2013). At smaller scales, extreme precipitation event frequency and intensity also show large regional variability (e.g., Beniston et al. 2007; Kay and Washington 2008; Seneviratne et al. 2012; Vizy and Cook 2012; Haensler et al. 2013; Stocker et al. 2013; Barros et al. 2014; Sylla et al. 2015). For example, California lies in between the mid-latitude region where precipitation extremes are projected to increase and the subtropical region where precipitation extremes are projected to decrease, with a large area in between where the sign of the change is unknown (e.g. Meehl et al. 2007; Neelin et al. 2013).

Because of the potential socioeconomic impacts associated with precipitation extremes, it is important to assess for changes in changes in the frequency and intensity of organized convection and storm tracks. For example, there is growing evidence in climate change research that overall global tropical cyclone frequency will decrease under global warming (e.g., Emanuel et al. 2008; Knutson et al. 2008, 2010, 2013; Bender et al. 2010), but the intensity of tropical cyclones will increase, both as a measure of rain rate and hurricane

category (e.g., Webster et al. 2005; Emanuel et al. 2008; Gualdi et al. 2008; Knutson et al. 2008, 2013; Bender et al. 2010). As for changes in mid-latitude storm tracks, Hall et al. (1994) and Yin (2005) note increased baroclinicity and a poleward shift of mid-latitude storm tracks across coupled climate model simulations.

A number of observational studies at small scales have used cluster-based measures to analyze storm behavior. For example, Skok et al. (2013) uses satellite-retrieved rain rates from the Tropical Rainfall Measuring Mission (TRMM-3B42) to employ space-time clusters to investigate tropical cyclone precipitation statistics. Wood and Field (2011) and Peters et al. (2009) examine cloud cluster area probability distributions, Peters et al. (2012) analyze distributions of precipitation integrated over contiguous precipitating clusters, and Peters et al. (2010) examine distributions of precipitation integrated over temporal events, noting in each case that probability density tends to exhibit a scale-free power law range, with a sharp cutoff after which the probabilities of clusters with large area and high power decrease more rapidly.

Given the uncertainties surrounding extreme precipitation projections, there is a need for substantiating measures of extreme precipitation, such as precipitation integrated across a cluster of contiguous precipitating grid cells, in future climate simulations. In this dissertation, statistical and spatial distributions of precipitation integrated across a cluster are investigated on a global scale for the first time as i) potentially useful methods of characterizing the current statistics of extreme precipitation events over the Tropics and mid-latitudes and ii) a method of quantifying changes in the frequency and spatial distribution (i.e., the storm track) of the most powerful storms under global warming.

This dissertation attempts to answer following questions. First, using satellite-retrieved rain rate data from the TRMM-3B42 and Special Sounder Microwave Imager/Sounder (SSM/I-

SSMIS) datasets, what is the state of extreme precipitation (as measured by cluster power) in current climate? Second, can the High Resolution Atmosphere Model (HIRAM) and a suite of 7 coupled climate models from the Coupled Model Intercomparison Project Phase 5 (CMIP5) experiment accurately reproduce observed cluster power statistics? Third, how does the frequency of the most powerful precipitation clusters change under global warming? Fourth, have there been statistically significant changes to the frequency of the most powerful storms in current climate, and when do such changes become statistically significant in this model suite? Fifth, how does the spatial distribution (i.e. storm tracks) of the most intense precipitation clusters change during winter under global warming?

As for the structure of the dissertation, in Chapter 2, we establish a baseline of observed cluster power behavior over the Tropics in recent climate, and assess the skill of the HIRAM in capturing observed cluster power statistics. We then analyze for changes in the frequency of the most intense storms relative to recent climate under a "business as usual" global warming scenario, and test a possible physical mechanism behind such changes. In Chapter 3, we check for detectability of statistically significant changes in the frequency of the most intense precipitation clusters in recent climate using SSM/I-SSMIS rain rates and data from the observationally-constrained National Centers for Environmental Prediction (NCEP) 2 Reanalysis model. We also compare results from our analysis of HIRAM output to cluster power distributions from the set of 7 comparatively high resolution coupled atmosphere/ocean CMIP5 models, examining first for projected changes to cluster power under the Representative Concentration Pathway (RCP) 8.5 scenario, then investigating when changes first become statistically significant compared to recent climate. In Chapter 4, we analyze cluster power distributions over boreal winter, first establishing an observed baseline of cluster

power statistics and spatial patterns of the most intense storms over the Northern Hemisphere. We then i) assess the ability of the HIRAM and the same suite of 7-CMIP5 models used in Chapter 2 to capture observed cluster power statistics, ii) check for changes to the frequency of the most powerful precipitation clusters by end-of-century, iii) analyze the spatial distribution of such changes, and iv) review output from 10 simulations from the National Center for Environmental Research Large Ensemble Community Project (NCAR LENS) to evaluate the impact of internal variability on the statistics. Each chapter serves as a stand-alone paper, with an introduction, explanation of data and methods, analysis, discussion of results, and references. References for the papers cited in the general introduction to the dissertation are distributed among the reference sections for Chapters 2-4.

2 Distributions of Tropical Precipitation Cluster Power and Their Changes Under Global Warming: Part I

2.1 Abstract

The total amount of precipitation integrated across a precipitation cluster (contiguous precipitating grid cells exceeding a minimum rain rate) is a useful measure of the aggregate size of the disturbance, expressed as the rate of water mass lost or latent heat released, i.e. the power of the disturbance. The probability distribution of cluster power is examined over the Tropics using Tropical Rainfall Measuring Mission (TRMM) 3B42 satellite-retrieved rain rates and global climate model output. Observed distributions are scale-free from the smallest clusters up to a cutoff scale at high cluster power, after which the probability drops rapidly. After establishing an observational baseline, precipitation from the High Resolution Atmospheric Model (HIRAM) at two horizontal resolutions (roughly 0.5 and 0.25°) are compared. When low rain rates are excluded by choosing a minimum rain rate threshold in defining clusters, the model accurately reproduces observed cluster power statistics at both resolutions. The most powerful precipitation clusters are found in the tail region, so changes in tail behavior have a great influence on the frequency of the most powerful storms. Middle and end-of-century cluster power distributions are investigated in HIRAM in simulations with prescribed sea surface temperatures and greenhouse gas concentrations from a "business as usual" global warming scenario. The probability of high cluster power events increases strongly by end-of-century, by roughly a factor of 20 for the highest-power events for which statistics can be computed. Clausius-Clapeyron scaling accounts for only a fraction of the increased probability of high cluster power events.

2.2 Introduction

Extremes of precipitation intensity are projected to change across all global warming scenarios in the Coupled Model Intercomparison Project Phase 3 (CMIP3) and CMIP5 experiments (Tebaldi et al. 2006; Kharin et al. 2007, 2013; Sillmann et al. 2013). Tebaldi et al. (2006) review historical and future simulations from a suite of 9 coupled global climate models across multiple emissions scenarios, finding a clear signal of increased precipitation intensity emerging by end-of-century over the globe. Kharin et al. (2007 and 2013) also analyze a suite of coupled climate models for consistency in projections of extreme precipitation spanning the CMIP3 and CMIP5 experiments, finding shorter wait times for extreme precipitation events by end-of-century relative to historical climate, and that the intensity of extreme precipitation events increases at a rate of 6% per °C of warming across both CMIP3 and CMIP5 experiments. Additionally, Sillmann et al. (2013) find that several metrics of precipitation extremes increase proportional to warming.

Uncertainties regarding changes in precipitation extremes emerge in both observations (e.g., Easterling et al. 2000; Alexander et al. 2006; Kharin et al. 2007, 2013; Lenderink and van Meijgaard 2008; Allan et al. 2010) and in global-scale simulations of extreme precipitation in recent climate and future climate (e.g., Tebaldi et al. 2006; Kharin et al. 2007, 2013; Allan and Soden 2008; Allan et al. 2010; Sillmann et al. 2013). Kharin et al. (2007) hypothesize that, over the Tropics, uncertainty in simulated extreme precipitation results from limitations in the representation of associated physical processes in climate models. Additionally, simulated precipitation extremes from an ensemble of 19 CMIP3 models are lower than observed precipitation extremes from 1987-2004 (Allan and Soden 2008). At regional scales, a survey of climate model studies using multiple approaches (e.g., multi-model ensembles, downscaling)

suggests that projected changes to extreme precipitation event frequency and intensity also exhibit large regional variability (e.g., Beniston et al. 2007; Kay and Washington 2008; Seneviratne et al. 2012; Vizy and Cook 2012; Haensler et al. 2013; Stocker et al. 2013; Barros et al. 2014; Sylla et al. 2015).

Characterizing changes in the frequency and intensity of organized convection, including in tropical cyclones, is important because of their potential socio-economic impacts. Many studies into tropical cyclone changes under global warming suggest that overall global tropical cyclone frequency will decrease by end-of-century (e.g., Emanuel et al. 2008; Knutson et al. 2008, 2010, 2013; Bender et al. 2010), though tropical cyclone intensity is projected to increase, both measured by higher rain rates and hurricane category (e.g., Webster et al. 2005; Emanuel et al. 2008; Gualdi et al. 2008; Knutson et al. 2008, 2013; Bender et al. 2010). Changes in tropical cyclone intensity under global warming are further investigated in climate model simulations by Knutson et al. (2013), Villarini et al. (2014), and Wehner et al. (2015). Decreases in the total number of tropical cyclones but increases in intense tropical cyclones in future climate under global warming are described in Knutson et al. (2013) and Wehner et al. (2015). Rainfall rates associated with tropical cyclones are projected to increase (Knutson et al. 2013; Villarini et al. 2014; Wehner et al. 2015), scaling with the Clausius-Clapeyron (CC) relationship in some regions (Knutson et al. 2013; Villarini et al. 2014), but exceeding results expected under CC-scaling near centers of tropical cyclones (Knutson et al. 2013; Wehner et al. 2015). More generally, changes in convective organization, as noted in observations by Tan et al. (2015), may be important to changes in precipitation extremes.

Work to better understand processes of convective organization (e.g., Leary and Houze 1979; Houze 1982; Houze 1989; Mapes and Houze 1993; Houze 2004) in current climate

includes studies of the self-aggregation of tropical convection over smaller domains (e.g., Bretherton et al. 2005; Muller and Held 2012; Khairoutdinov and Emanuel 2013; Wing and Emanuel 2014; Wing and Cronin 2015). The aggregation of convection into clusters has been shown to be sensitive to: hydrometeor parameterization (Bretherton et al. 2005); Coriolis forcing (Bretherton et al. 2005); low cloud distribution (Muller and Held 2012); SST changes (Khairoutdinov and Emanuel 2013); and advection of moist static energy (Wing and Cronin 2015). Additionally, Wing and Emanuel (2014) note that processes that initiate the aggregation of convective cells into clusters (e.g., atmospheric water vapor absorbing shortwave radiation, surface heat flux) are different than processes that maintain aggregation once it has already occurred (e.g., longwave radiation feedback). Cluster aggregation processes at smaller scales appear to continue into idealized large domains in modeling studies (Holloway et al. 2012; Bretherton and Khairoutdinov 2015; Arnold and Randall 2015).

Observational studies of tropical precipitation clusters over large domains include Mapes et al. (2009), Peters et al. (2009, 2010, 2012), Wood and Field (2011), and Skok et al. (2013). In Skok et al. (2013), space-time clusters are defined to analyze precipitation statistics associated with tropical cyclones, using satellite-retrieved precipitation estimates from the Tropical Rainfall Measuring Mission (TRMM-3B42). Mapes et al. (2009) examines cluster lifecycle and size distributions using IR and scatterometer data sets over the Tropics, noting that small clusters with brief lifespans constitute the vast majority of oceanic precipitation clusters. Wood and Field (2011) and Peters et al. (2009, 2010, 2012) analyze storm cluster organization using a variety of observational datasets, noting that probability distributions of cluster cloud area (Peters et al. 2009; Wood and Field 2011), precipitation integrated across contiguous precipitating clusters (cluster power, Peters et al. 2012) or precipitation integrated

across temporal events (Peters et al. 2010) follow a long, scale-free power law, with a distinct cutoff, i.e. a more rapid drop in frequency of occurrence, at large cluster area and high power. Cluster power behavior above the cutoff is different than behavior below the cutoff, in part because different physical processes drive daily tropical convection and tropical cyclones (Peters et al. 2010, 2012). Furthermore, Peters et al. (2012) noted that tropical cyclones provide significant contributions to the tail in the large event regime.

There is a need for the validation of rainfall simulations in climate models, especially extreme events in quantities likely important for changes under global warming, such as measures of organized convection. Distributions of precipitation integrated across a cluster over the Tropics are thus examined here for the first time as i) a potentially a useful measure both as a metric of model simulation in current climate and ii) as a measure of changes in tropical disturbances in simulations of future climate. This integrated precipitation can be described as cluster power (defined here as the instantaneous latent heat release integrated over a cluster of contiguous precipitating grid cells). Distributions and tail sensitivity to the most powerful precipitation clusters at a global scale are examined in satellite observations with full spatial coverage and compared to climate model simulations for the first time, examining the relationship between cluster power and rain rate across a global domain. We first establish an observational baseline using satellite-retrieved precipitation data to test its usefulness for comparison to climate model output at two resolutions. Second, we assess how reliably a high resolution climate model can simulate historical cluster power distributions. Lastly, we apply output from future runs of the same model to examine mid- and end-of-century simulated cluster power distributions, quantifying the influence of global warming on cluster power

behavior. These results for a high-resolution model set the stage for further examination of lower resolution coupled models from the CMIP5 archive in Chapter 3.

2.3 Data and methods

2.3.1 Observational data

Satellite-retrieved rain rate data from the Tropical Rainfall Measuring Mission (TRMM-3B42) program are used to build a baseline of cluster power behavior. Data from sensors onboard the TRMM spacecraft are merged with data from other satellites to provide gap-free TRMM-3B42 rain rate data over oceans and land, and are available beginning in 1998 (Huffman et al. 2007; TRMM 2015). These data have units of millimeters per hour and are available every three hours over a 0.25^0 x 0.25^0 latitude-longitude grid. For consistency with our comparisons in Chapters 3 and 4, we analyze twice daily TRMM-3B42 time slices at 00 UTC and 12Z UTC. To calculate cluster power, precipitating grid cells meeting a minimum rain rate threshold are first aggregated into distinct clusters. From there, cluster power is expressed as the instantaneous latent heat release integrated over a cluster in units of gigawatts by multiplying rain rates by the latent heat of condensation (2.5×10^6 J kg^{-1}), which relates cluster power to the Earth's energy budget. Cluster power can also be expressed equivalently in terms of a mass budget as the integrated mass of water lost per hour (kg H_2O hr^{-1}) with 1 GW equal to 1.4×10^6 kg H_2O hr^{-1} lost.

2.3.2 Climate model data

Precipitation data from the Geophysical Fluid Dynamics Laboratory (GFDL) High Resolution Atmospheric Model (HIRAM) at two horizontal resolutions are incorporated into

this study: HIRAM-C360 (25 km) and HIRAM-C180 (50 km) (Zhao et al. 2009, 2010, 2012; Chen and Lin 2011; Held and Zhao 2011; Merlis et al. 2013; Villarini et al. 2014; GFDL 2015). HIRAM output is derived from the historical Atmospheric Model Intercomparison Project (AMIP, 1979-2008) and future (SST2030, 2026-2035 and SST2090, 2086-2095) experiments, incorporating prescribed sea surface temperatures (SSTs) from the Hadley dataset for the historical period, and greenhouse gas and SST anomalies from the GFDL-Earth System Model 2 (ESM2) for future runs. Precipitation data are given at three hourly intervals in units of precipitation flux (kg m^{-2} s^{-1}), though to stay consistent with the TRMM-3B42 retrieval, instantaneous HIRAM cluster power snapshots from only 00 UTC and 12 UTC with rain rates meeting a minimum threshold are aggregated into distinct clusters. These clusters then have their rain rates converted to instantaneous latent heat release per grid cell, using the same method as the TRMM-3B42 dataset. Next, we compare AMIP output with satellite-retrieved data to assess its accuracy in simulating historical conditions. After establishing an accurate AMIP baseline, we then use these AMIP simulations for the comparison with future climate simulations, with C360 data directly compared to observed data due to their comparable spatial resolution.

2.3.3 Domain

Cluster power distributions over two domains are shown to illustrate the extent to which cluster power behavior is influenced by domain size: the Tropics, and the northern Atlantic-East Pacific. The Tropics domain is centered over the Equator, stretching across the Earth from 30^0S to 30^0N. The Atlantic-East Pacific domain is a subset of the Tropics, extending from the Equator to 30^0N and from 140^0W across the Americas and Atlantic Ocean

to 0^0E, chosen to include major regions of tropical storm formation. Although two domains are shown here, we examined cluster power distributions over other domains and obtained similar results.

On average, 69 percent of all named tropical cyclones that form each year occur in the Northern Hemisphere (Landsea and Delgado 2015). This study considers 1 May to 30 September, to focus on the period of greatest tropical cyclone activity in the Northern Hemisphere.

2.4 Analysis

2.4.1 Cluster power distributions: observations

Previous cluster studies have analyzed cluster quantities such as cloud area above a certain reflectivity threshold (Wood and Field 2011), storm cluster area and duration using IR imagery and scatterometer data (Mapes et al. 2009), and cluster area and power using satellite radar and passive microwave imagery (Peters et al. 2009, 2012). In the case of radar imagery, these have been for narrow swaths, limited by the radar swath width. In Fig. 2.1-2.3 we form an observational baseline for cluster power using satellite-retrieved rain rate data, evaluating the merged satellite TRMM-3B42 retrieval at a global scale over land and ocean, so statistics are not limited by swath width. Figure 2.1 examines TRMM-3B42 cluster power distributions for multiple rain rate thresholds at a global scale, and Fig. 2.2 presents TRMM-3B42 distributions over the smaller Atlantic-East Pacific domain. In Fig. 2.3 we characterize typical cluster size and morphology by analyzing mapped clusters at the 0.1 mm hr^{-1} and 0.7 mm hr^{-1} rain rate thresholds across the Tropics.

Across the Tropics at multiple rain rate thresholds (Fig. 2.1), TRMM-3B42 cluster power distributions follow a long, scale-free power law, similar to Peters et al. (2012), which noted an exponent of -1.87 in the TRMM radar 2A25 retrieval. The exponent here (as estimated from the slope of the least squares best-fit line over the power law range at the 0.7 mm hr^{-1} rain rate threshold in Fig. 2.1) is -1.50. In Fig. 2.1, the cutoff that terminates the power law range for all rain rate thresholds lies at approximately 10^5 GW, with the frequency of the highest-power clusters for all distributions falling off more rapidly after the cutoff. This cutoff also appears to be insensitive to rain rate threshold. Note that the cluster power of the lowest power bin depends on rain rate threshold, simply because the minimum cluster power is a function of the minimum rain rate considered and the grid cell size. Cluster power distributions must begin at a threshold-dependent minimum power and are shifted slightly because this affects the normalization of the probability distribution.

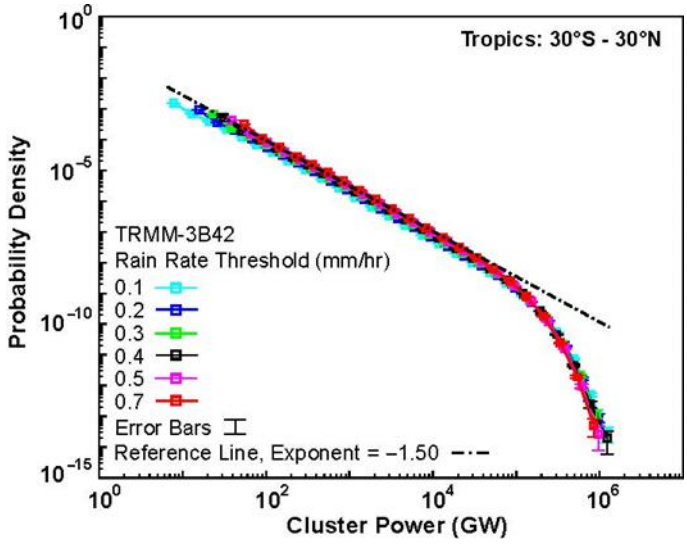

Fig. 2.1: Probability distributions of cluster power, i.e., precipitation integrated over clusters of contiguous pixels exceeding the specified rain rate threshold, expressed in units of latent heat release (gigawatt). Clusters are calculated from the TRMM-3B42 precipitation product, over the Tropics, May-September 1998-2008. The least squares best-fit exponent before the cutoff (fit over the scale-free range up to 10^5 GW for the 0.7 mm hr^{-1} threshold) is -1.50.

TRMM-3B42 cluster power distributions over the Atlantic-East Pacific (Fig. 2.2) closely parallel the distributions for the Tropics, with similar least squares best-fit exponents (-1.42 versus -1.50), cutoff value (10^5 GW), and insensitivity to rain rate threshold. At the highest-power bin for the Atlantic-East Pacific, domain size has a modest impact on the size of the largest possible clusters due to longitudinal boundaries. For example, at a probability density of 10^{-11}, the cluster power difference between the Atlantic-East Pacific and Tropics cluster power distributions is approximately 0.75 x 10^5 GW.

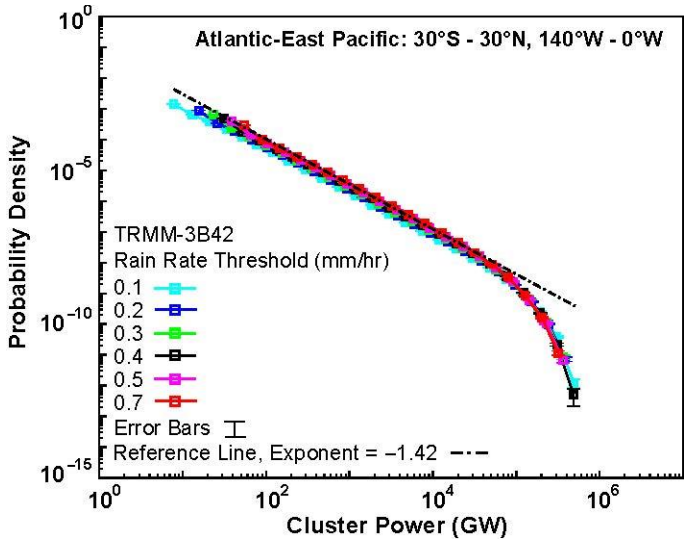

Fig. 2.2: Same as in Fig. 2.1, except for the Atlantic-East Pacific. The least squares best-fit exponent before the cutoff is -1.42.

Intriguingly, the form of the cluster power probability distribution is similar to what occurs for temporal clusters, i.e. accumulations of precipitation over events, in a simple prototype model (Stechmann and Neelin 2011, 2014) that also exhibits a power law range with approximately exponential cut off. The exponent of that simple configuration, -1.5, is close to the exponent for precipitation integrated over spatial clusters here. An apparent exponent of -1.2 or steeper, depending on convective parameters, was noted for the power law range in cluster area distributions in a similar simple model (Hottovy and Stechmann 2015), but no

quantitative prototype appears to exist yet for integrated cluster precipitation. For continuity with previous literature, probability distributions for cluster area are shown for reference in Fig. A1 of the Appendix for Chapter 2). Similar to the power distributions, an approximately power-law range is found for cluster area, extending from the minimum area ($7x10^8$ m^2) to a qualitatively similar cutoff at around $3x10^{11}$ m^2, with exponent of approximately -1.7. The cutoff for area distributions exhibits slightly more dependence on rain rate threshold. We choose the integrated precipitation/power for the cluster for the remainder of this work because of its greater physical importance due to the correspondence to total water loss/latent heat release from the cluster.

Figure 2.3 displays typical satellite-retrieved cluster morphology at the lowest and highest minimum rain rate thresholds considered in this study (0.1 mm hr^{-1} and 0.7 mm hr^{-1}) for a sample of days in 2003 and 2004. Most clusters at the 0.1 mm hr^{-1} rain rate threshold with high cluster power ($\geq 10^5$ GW) resemble tropical cyclones, mesoscale convective systems, ITCZ-like clusters, or the tail ends of mid-latitude fronts that occasionally pass between 20^0 and 30^0N/S. At the 0.7 mm hr^{-1} rain rate threshold, overall structure of most clusters remains the same, with only some trimming on the edges of the largest clusters. Figure A2 of the Appendix for Chapter 2 shows an example for the Atlantic-East Pacific domain. Our analysis of cluster morphology from this sample of mapped precipitation clusters further suggests little variation in cluster power behavior across rain rate thresholds in the observational dataset.

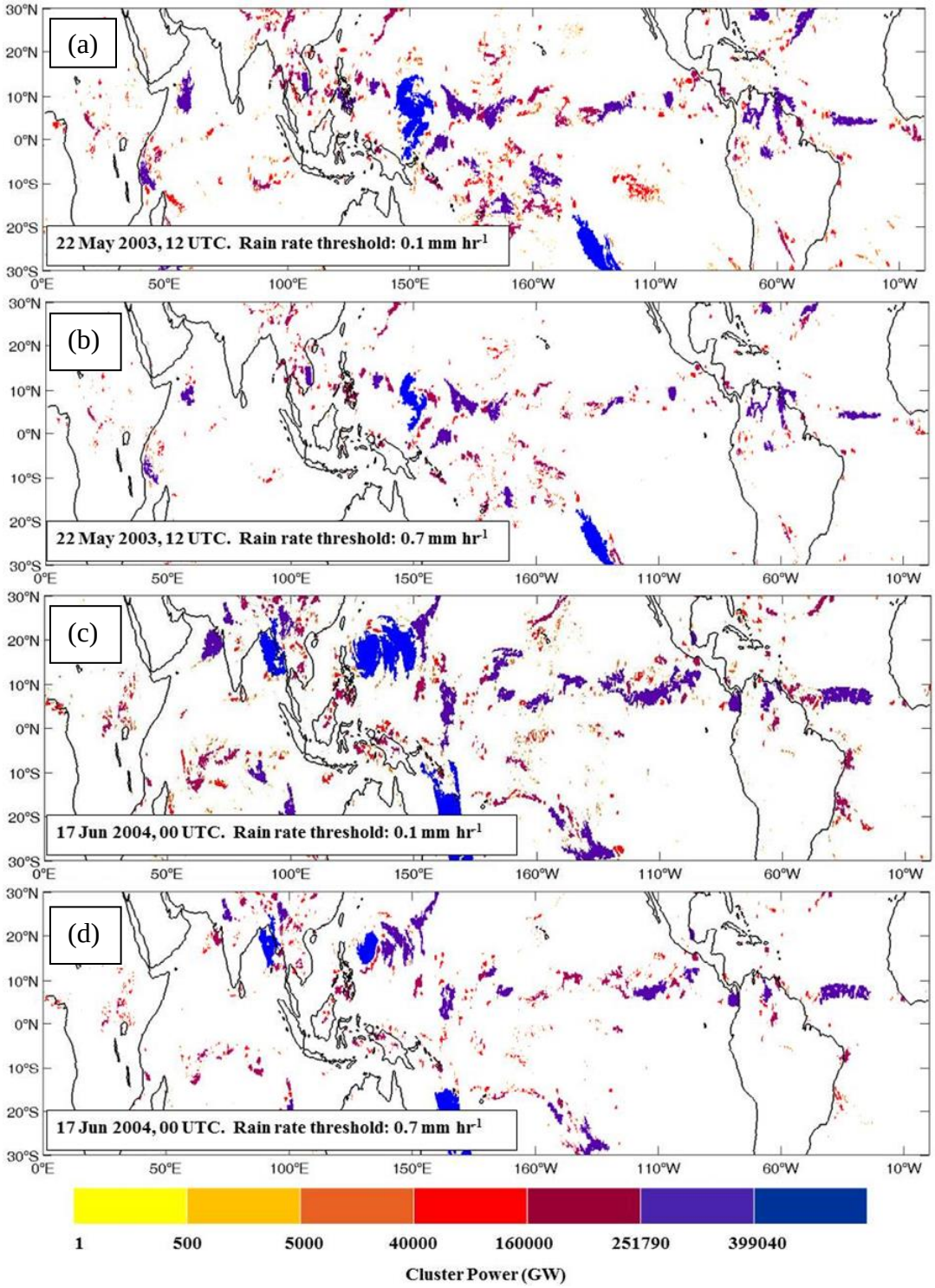

Fig. 2.3: Examples of precipitation clusters from selected TRMM-3B42 time slices for rain rate thresholds 0.1 mm hr^{-1} (Fig. 2.3a and Fig. 2.3c) and 0.7 mm hr^{-1}(Fig. 2.3b and Fig. 2.3d), as indicated. The spatial distribution of each cluster is shown with the power integrated over the cluster given by the color bar.

2.4.2 Cluster power distributions: historical HIRAM output

Figures 2.4-2.6 quantify how the HIRAM at two horizontal resolutions approximates observed cluster power behavior. Figures 2.4-2.5 compare HIRAM cluster power distributions at multiple rain rate thresholds, and Fig. 2.6 overlays HIRAM-C360 and TRMM-3B42 cluster power distributions at two rain rate thresholds. We also compare HIRAM cluster power distributions with a simple model prototype at two rain rate thresholds (Fig. 2.6), investigating whether or not the HIRAM captures the atmospheric dynamics behind the spatial autocorrelation (e.g., the formation of clusters) of precipitation between neighboring grid cells.

Like the TRMM-3B42 dataset (Fig. 2.1), HIRAM cluster power distributions (Fig. 2.4-2.5) are also scale-free along a power law range, have a cutoff around 10^5 GW, and display little sensitivity to rain rate threshold along the power law range. Additionally, HIRAM distribution least squares best-fit exponents (for the 0.7 mm hr^{-1} threshold) range from -1.36 to -1.39, similar to the TRMM-3B42 analysis (-1.50/-1.42, Fig. 2.1-2.2). The lower resolution simulation (C180) has a shorter scale-free region due to coarser resolution resulting in a larger minimum cluster area and hence larger minimum cluster power. Otherwise, its scale-free power law range and cutoff closely parallel that from the higher resolution simulation (Fig. 2.5).

Tail behavior sensitivity to rain rate threshold is quantified in Fig. 2.4. While TRMM-3B42 distributions exhibit little sensitivity, HIRAM distributions do exhibit substantial sensitivity above the cutoff for low rain rate thresholds. At rain rate thresholds below 0.3 mm hr^{-1}, the cutoff shifts towards higher power. This finding is consistent with previous findings that global climate models can overestimate light precipitation coverage (e.g., Dai 2006). Tails converge at rain rate thresholds greater than 0.2 mm hr^{-1}, suggesting that it is important to

exclude low rain rates from clusters and that higher minimum rain rate thresholds are more robust for comparison with observations. For an illustration of the spatial behavior of modeled precipitation clusters, refer to Appendix for Chapter 2 Fig. A3-A4.

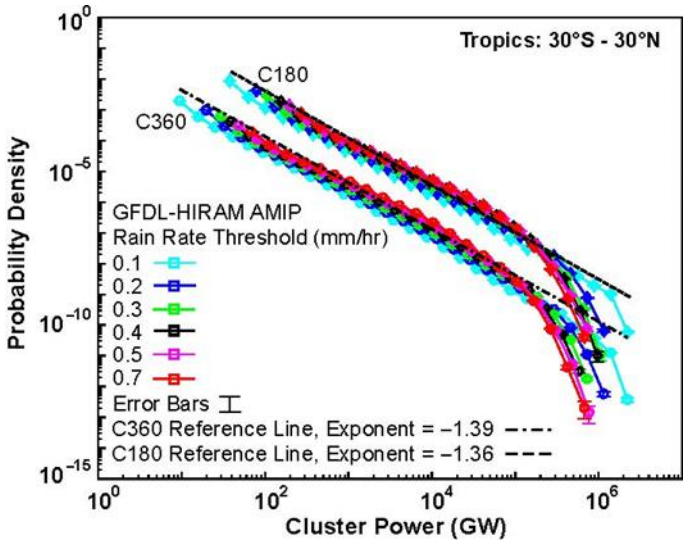

Fig. 2.4: Same as Fig. 2.1, but for GFDL-HIRAM AMIP simulations at two resolutions (C180 and C360). For readability, HIRAM-C180 AMIP distributions have been shifted up vertically by a decade. The least squares best-fit exponent before the cutoff is -1.36 for HIRAM C180 and -1.39 for HIRAM-C360.

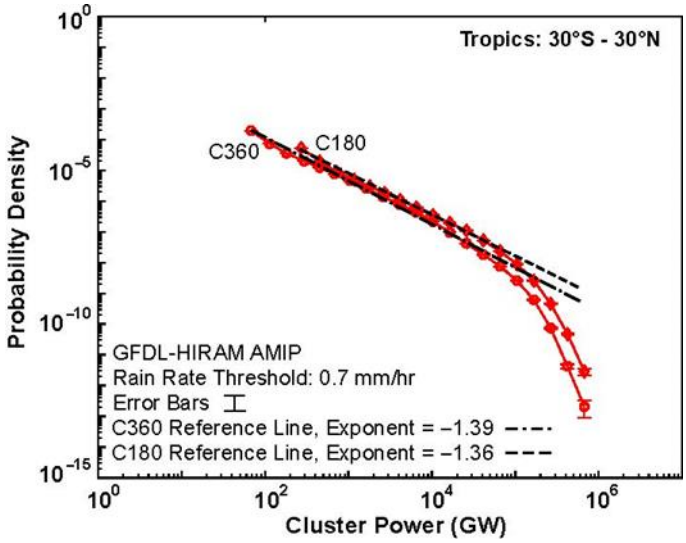

Fig. 2.5: Same as in Fig. 2.4, but comparing modeled cluster power probability distributions between resolutions for the 0.7 mm hr^{-1} rain rate threshold, with no vertical shift of the HIRAM C180 distribution.

The comparison between TRMM-3B42 and HIRAM-C360 cluster power distributions in Fig. 2.6 shows that, in general, the tail of the modeled power distribution at the 0.7 mm hr^{-1} rain rate threshold more closely parallels the TRMM-3B42 distribution. Although their least squares best-fit exponents are slightly different (-1.39 for HIRAM-C360, Fig. 2.4, -1.50 for TRMM-3B42, Fig. 2.1), and the tail of the TRMM-3B42 distribution is longer, the tails for both distributions at high power are very similar.

We also ask how HIRAM-C360 cluster power distributions compare to distributions from a simple model prototype (Fig. 2.6), helping assess whether HIRAM can simulate the atmospheric dynamics driving the formation of precipitation clusters. Our simple model prototype is analogous to a statistical null hypothesis model, in that we compare HIRAM-C360 cluster power distributions to simple model prototype cluster power distributions in which the spatial autocorrelation between grid cells has been removed. To build a simple model prototype and remove the spatial autocorrelation, we select rain rate values for each grid cell from random time steps, thereby preserving rain rate probabilities while removing spatial autocorrelation (except aspects associated with spatial variations of probability in the inhomogeneous basic state). In this study, simple model prototypes at rain rate thresholds of 0.3 mm hr^{-1} and 0.7 mm hr^{-1} are built and compared to HIRAM-C360 output, using HIRAM-C360 data from 1 May-30 September 1979-1999. Model data are chosen in lieu of satellite data due to a longer time series available for random sampling. The simple model prototype distributions clearly have different structures than the observed/HIRAM distributions; the power law range, if present, is too short to be clearly seen, and distinct cutoffs occur at relatively low cluster power. This comparison suggests that the features of the cluster

probability density function captured by HIRAM are not easily obtained, implying that HIRAM reasonably simulates nontrivial atmospheric dynamics behind cluster formation.

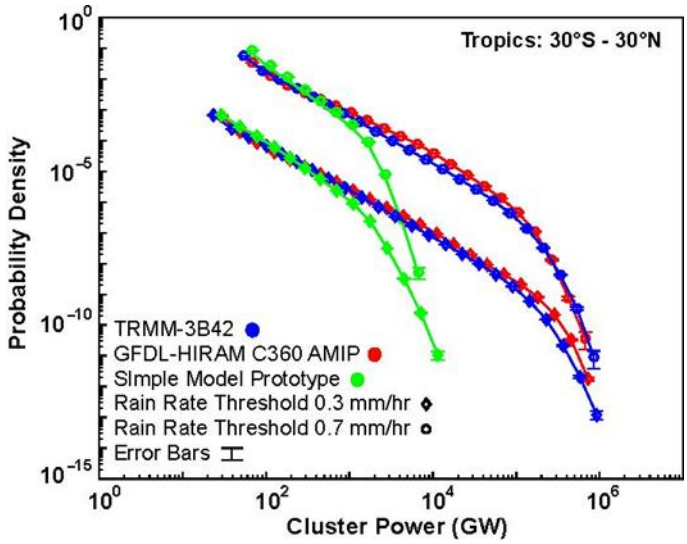

Fig. 2.6: Observed (TRMM-3B42) and modeled (HIRAM-C360 AMIP) Tropics cluster power probability distributions for May-September 1998-2008 for rain rate thresholds 0.3 mm hr^{-1} and 0.7 mm hr^{-1}. Also plotted are cluster probability distributions at each rain rate threshold from a simple prototype created by random selections from 1979-1999 HIRAM-C360 AMIP data that preserve probability distributions at each point but not spatial correlations (see text). The distributions for the 0.7 mm hr^{-1} rain rate threshold have been shifted up vertically by two decades to improve readability.

2.4.2 Cluster power distributions: future HIRAM output

Changes in the frequency of high cluster power events (e.g., tropical cyclones) may have large societal repercussions. As a result, we examine changes in future cluster power distributions (Fig. 2.7-2.9) by comparing historical (AMIP), mid-century (SST2030), and end-of-century (SST2090) cluster power distributions at the 0.7 mm hr^{-1} rain rate threshold used in this study. Historical, mid-century, and end-of-century distributions are very similar to each other before the cutoff, following the same long, scale-free power law range (Fig. 2.7). By end-of-century, there is a clear signal in both simulations that indicates a shift towards higher power in the tail region, implying more frequent intense precipitation clusters (Fig. 2.7). This

increase (for the highest three bins for which statistics can be calculated) ranges from a factor of 3.34, 9.95, and 20.39, respectively (Fig. 2.8a) for the highest resolution simulation by end-of-century. Additionally, if instead of considering changes to the probabilities of fixed bins, we consider how the tail of the distribution *extends*, the probability corresponding to the highest-power bin in the historical period shifts to higher power — for the end-of-century this probability occurs for a power that has increased by approximately a factor of 1.6 relative to current climate (Fig. 2.8a). Other studies (e.g., Knutson et al. 2013; Villarini et al. 2014; Wehner et al. 2015) have compared changes in modeled rain rates under global warming scenarios with changes expected under Clausius-Clapeyron (CC) scaling of humidity, so to test a possible physical explanation for the increased probability of intense precipitation clusters by end-of-century, we examine changes to cluster power distributions under a realistic global warming scenario. The difference in mean global temperature between HIRAM-C360 SST2090 and AMIP experiments is +2.16 K, within the range of temperature increase projected by Stocker et al. (2013). Assuming a 7% increase in relative humidity per 1 K warming under the CC relationship, this represents a possible 15.12% increase in precipitation under global warming. Given this warming, we multiply HIRAM-C360 AMIP rain rates (at the 0.7 mm hr^{-1} threshold) by a factor of 1.15, re-cluster (keeping the same threshold), and then re-analyze this CC-scaled dataset, comparing its distribution of cluster power to HIRAM-C360 AMIP and SST2090 distributions.

The application of a CC-scaling factor to the HIRAM-C360 AMIP dataset does increase frequency of the most powerful precipitation clusters and shift the tail region of the CC-scaled dataset towards higher power compared to the original HIRAM-C360 AMIP dataset (Fig. 2.8b). However, this application appears to only account for a fraction of the increased

probability of the most intense precipitation clusters, suggesting that the increased probability of the most intense precipitation clusters by end-of-century is significantly higher than that expected based on a simple CC-scaling of precipitation intensity. Knutson et al. (2013) and Wehner et al. (2015) also found that rain rate increases surrounding the cores (e.g., within 200 km) of intense tropical cyclones under global warming exceed rain rate increases that would be expected solely under CC scaling of precipitation, hypothesizing a link between this exceedance and the dynamics driving the intensity around the cores of intense tropical cyclones.

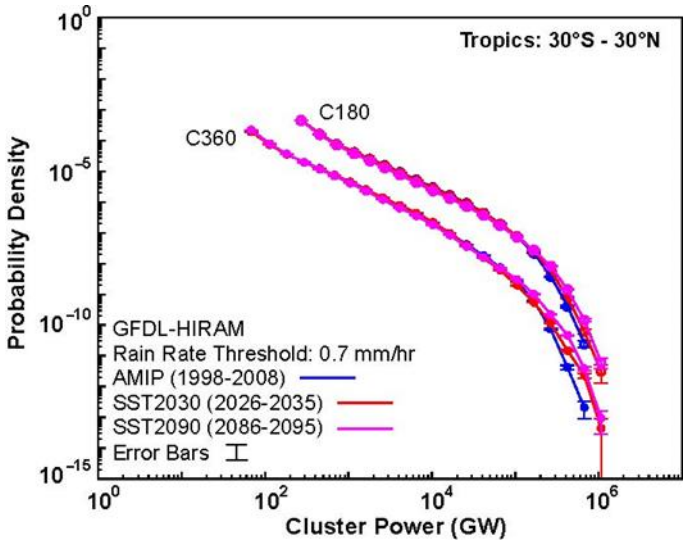

Fig. 2.7: Same as Fig. 2.4, displaying a comparison of HIRAM cluster power probability distributions at two resolutions for historical (AMIP, May-September 1998-2008) and future (SST2030/2090, May-September 2026-2035/2086-2095) simulations for the 0.7mm hr^{-1} rain rate threshold. HIRAM-C180 cluster power distributions have been shifted up vertically by a decade for readability.

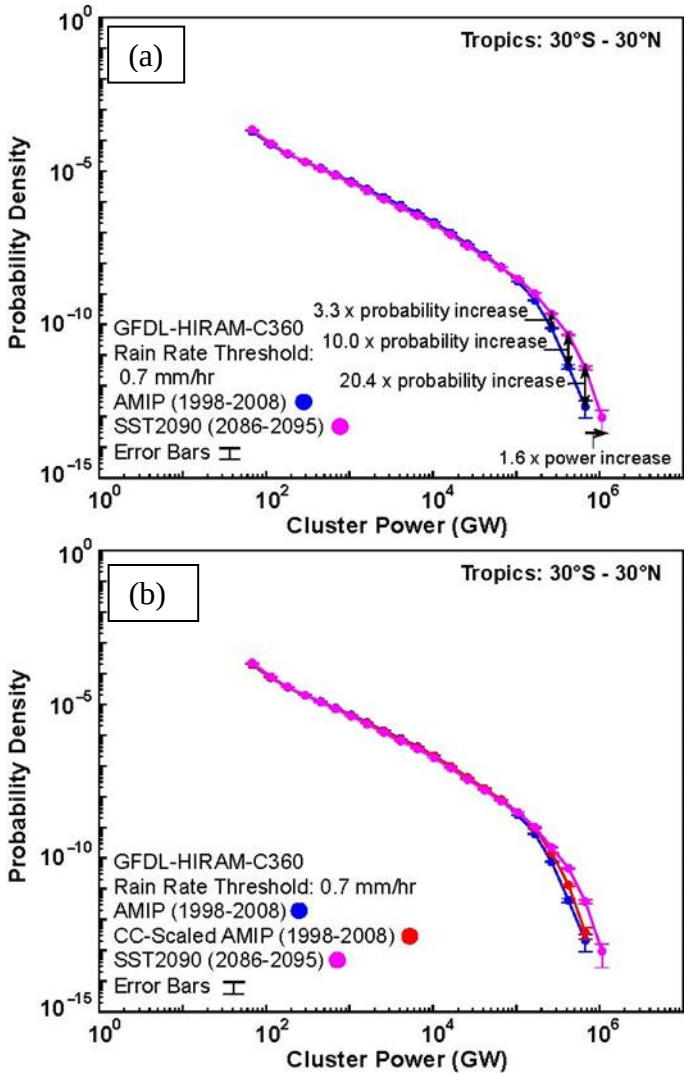

Fig. 2.8: As in Fig. 2.7, Fig. 2.8a displays the change in the distribution of cluster power between historical (AMIP) and future (SST2090) simulations for the 0.7mm hr^{-1} rain rate threshold using the higher resolution HIRAM (C360), with probability increase factors displayed for selected bins above the cutoff (vertical arrows). Horizontal arrow shows the estimated power increase for the probability value at the highest bin that can be estimated in current climate. Figure 2.8b is the same as Fig. 2.8a, with an additional comparison to the AMIP dataset with a CC-scaling factor applied (see text).

Lastly, visual inspection of 4,000 TRMM-3B42 and HIRAM-C360 AMIP cluster power maps suggests that the synoptic meteorology of the storms represented in the model is generally consistent with those in the observations and, further, that the meteorological features in the SST2090 simulation are not qualitatively different from those in the present climate, despite the differences in probability of large clusters. The western Pacific (e.g., the

Philippines) is qualitatively a region of substantial impact from storms (particularly tropical storms and typhoons) with cluster power in the highest three bins. Figure 2.9 shows an illustration of storms for the historical and end-of-century periods in HIRAM. Both periods exhibit qualitatively similar meteorology, with a higher frequency of storms from this high-power bin, especially common over the western Pacific.

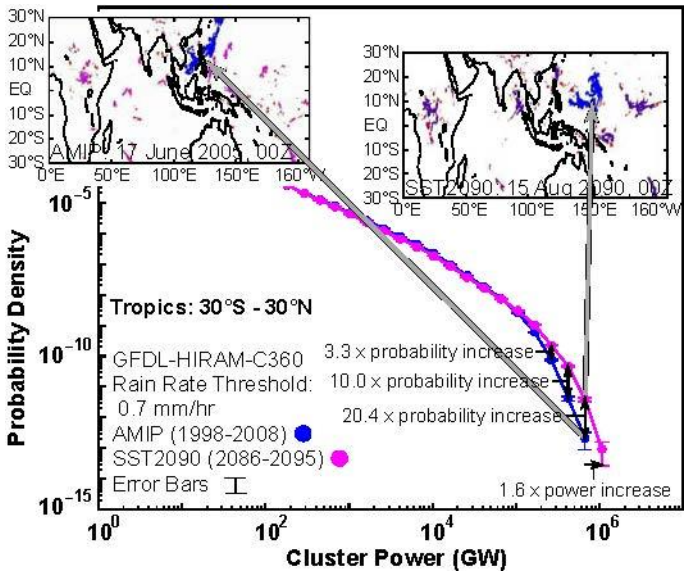

Fig. 2.9: Same as Fig. 2.8a with insets showing examples of clusters from AMIP and SST2090 simulations from a high-cluster-power bin from the historical period.

2.5 Discussion

Observed precipitation cluster area and power distributions have been shown to exhibit a power law range, with cutoffs at large cluster area and high cluster power (Peters et al. 2009, 2012). Cluster power here is defined as the precipitation integrated over contiguous precipitating grid cells (for precipitation above a minimum threshold). Here we typically express the cluster power in units of latent heat release, but it is equivalent up to a factor given

by the latent heat of condensation to a rate of water mass loss over the cluster. Cluster power distributions from the Tropics (30^0N - 30^0S) using precipitation data from the TRMM-3B42 satellite retrieval are compared to TRMM-3B42 cluster power distributions from the smaller Atlantic-East Pacific domain. Observed cluster power distributions for both domains follow a long, scale-free power law between 10 – 10^5 GW, and a rapid drop off in the frequency of precipitation clusters with high cluster power thereafter. In units of mass loss, the cutoff near 10^5 GW is equivalent to approximately 10^{12} kg hr^{-1}. The phenomena leading to these clusters range from convective phenomena at the grid cell scale (approximately 25 km) and mesoscale clusters through ITCZ disturbances and tropical cyclones. The cutoff at high power is largely independent of rain rate in the observations, and here is found in a data set not limited by swath width, or land versus ocean retrievals. This suggests that some set of physical factors within the tropical climate system and the meteorology of storm aggregation must lead to the existence of the cutoff.

HIRAM simulations at both resolutions for the historical period accurately reproduce observed distributions at the 0.7 mm hr^{-1} rain rate threshold, with similar least squares best-fit exponents over the power law range (-1.5 for TRMM-3B42, -1.39/-1.36 for HIRAM-C360/C180). At both model resolutions, the cutoff at high power is correctly produced near 10^5 GW, suggesting that model resolution has little impact on simulating cluster power. However, HIRAM cutoff values are sensitive to rain rate threshold, due to overly widespread occurrence of low rain rates, but agree well provided the threshold is not too low.

To help differentiate the HIRAM simulation of the atmospheric dynamics driving the aggregation of neighboring contiguous precipitating grid cells from simpler processes that might be hypothesized to account for some of the effects, we construct a simple model

prototype. Specifically, we remove the spatial autocorrelation between grid cells (randomizing the time step from which the rain rate sample is drawn) while preserving rain rate probabilities for each grid cell using HIRAM-C360 data from 1979-1999. We then run the same clustering and binning procedures as run on the observed and HIRAM datasets at two rain rate thresholds. Although clusters created by choosing values randomly at different grid points can in principle yield power law ranges under certain conditions, the resulting simple model prototype cluster power distributions behave very differently (e.g., do not exhibit a long power law range) than the observed and HIRAM distributions. This implies that the atmospheric dynamics driving cluster distributions in HIRAM are more complex than simply yielding reasonable probabilities of precipitation. The long scale-free range in both observations and HIRAM but not in the simplest prototype suggests that the length and slope of the scale-free range, as well as the apparent change dynamical regimes in the cutoff, constitute interesting targets for explanation in modeling of cluster aggregation.

Because the cutoff affects the probability of the highest cluster power events, potentially very important for human impacts, changes to cluster power distributions under global warming are examined. HIRAM cluster power distributions at both resolutions from the future SST2030 and SST2090 experiments have the same long, scale-free range as historical HIRAM output, but the cutoff tends to shift toward higher power. A natural simple hypothesis to compare against for the increased probability of more intense storms by end-of-century, is a CC-scaling of the precipitation to factor in the simplest impacts of temperature on humidity. Specifically, a CC-scaling factor of 7% increase per degree of warming under the projected change to mean global temperature (2.16 K, calculated using HIRAM-C360 AMIP and SST2090 temperature data) was applied to the HIRAM-C360 AMIP dataset before running the

same clustering and binning procedures. The resulting cluster power distribution with this hypothetical CC-scaled precipitation lies between the original AMIP and SST2090 cluster power distributions, indicating that the change in future cluster power distributions considerably exceeds expectations based on a simple CC-scaling of rain rates.

The shift of the cutoff toward higher cluster power in the warmer climate has a substantial impact on the frequency of occurrence of the largest storms. Examining the high-power part of the distribution using bin widths for which the three highest bins span a factor of 4 in storm power (2×10^5 GW to 8×10^5 GW), the change in probability increases monotonically through this range. The probability of high cluster power events from the three highest-power bins beyond the historical cutoff increases by a factor of roughly 3 for the third highest bin to a factor of 20 for the highest bin for which cluster power statistics can be computed. Geographically, this increase becomes especially apparent over the western Pacific, where many of the largest clusters occur.

Appendix for Chapter 2

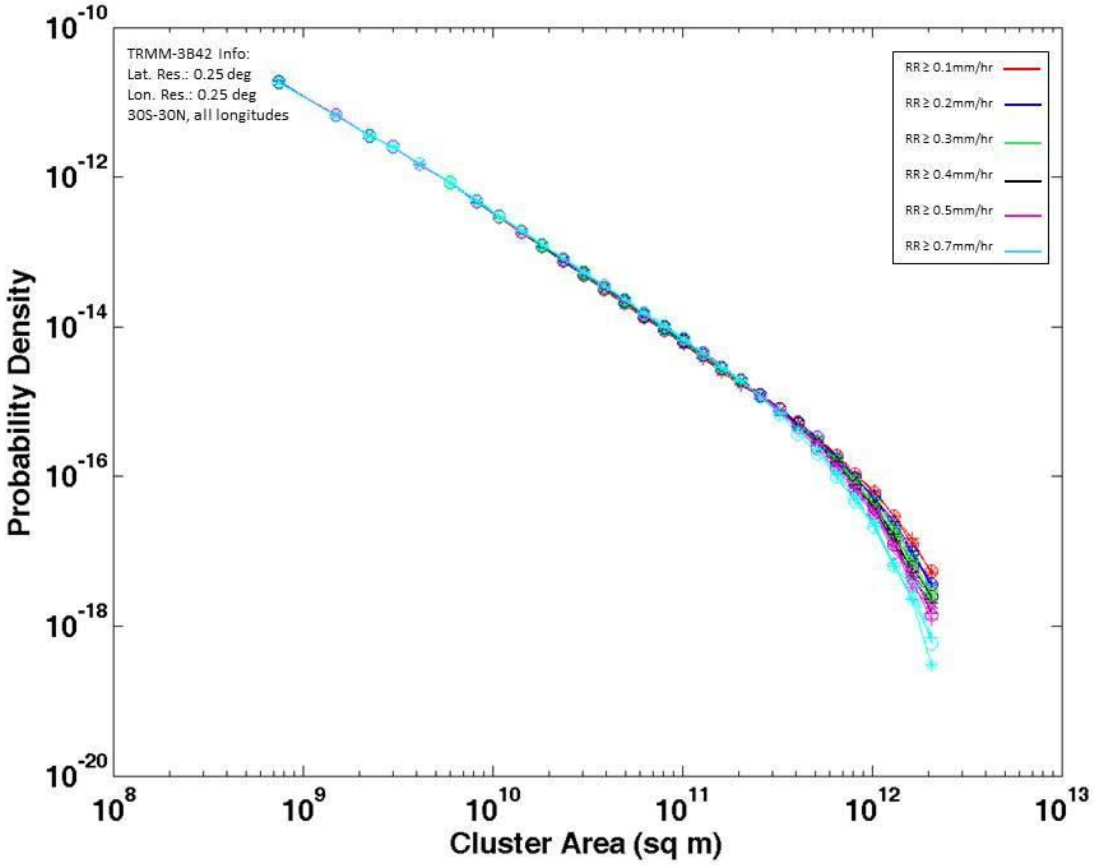

Fig. A1: Similar to Fig. 2.1 of the main text, but for probability of cluster area, i.e., area (m^2) of cluster of contiguous pixels exceeding the specified rain rate threshold, and for a shorter sample of years (2004-2007). Distributions are displayed for individual years to provide a sense of reproducibility.

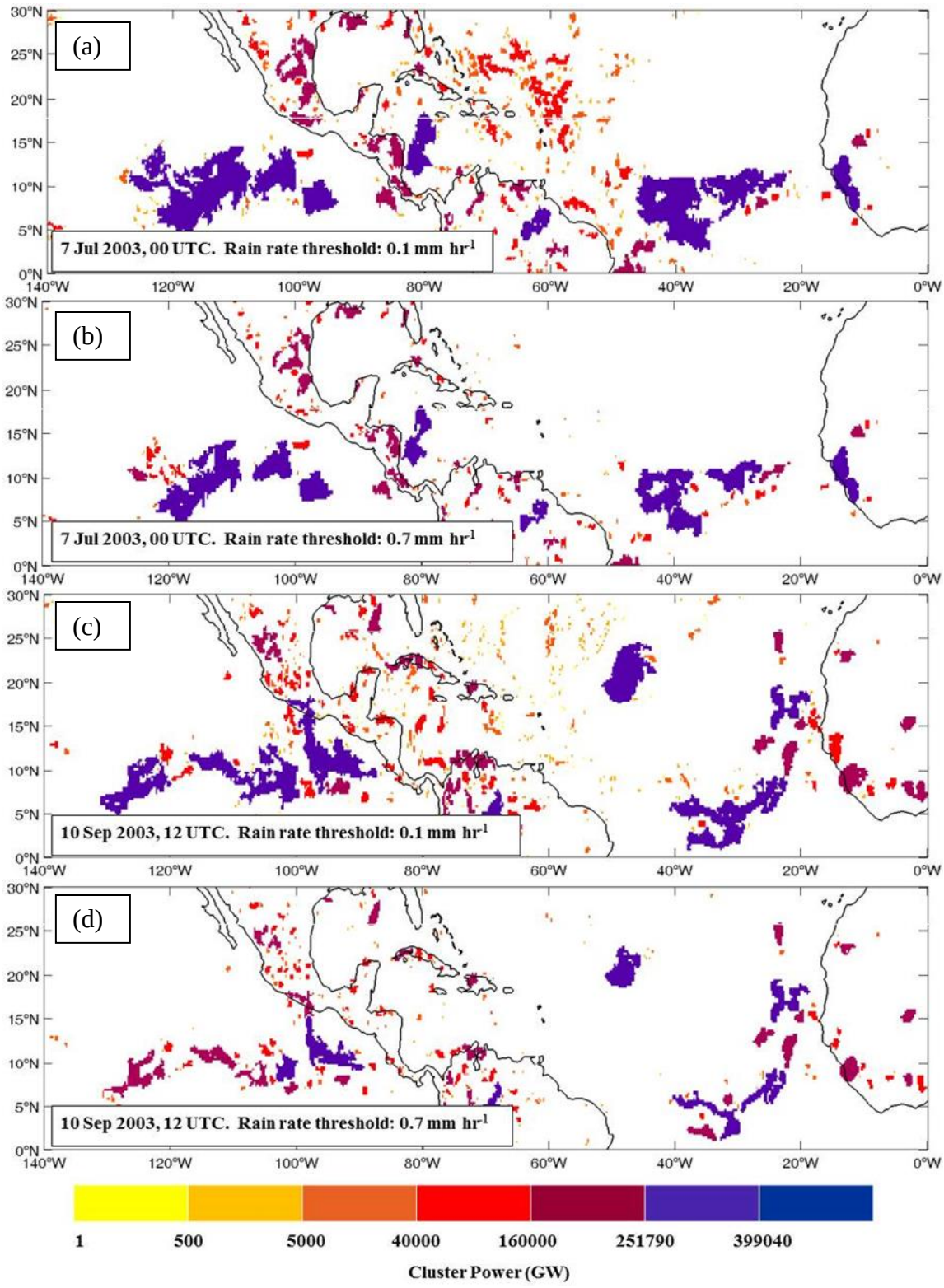

Fig. A2: Similar to Fig. 2.3 of the main text, but for the Atlantic-East Pacific.

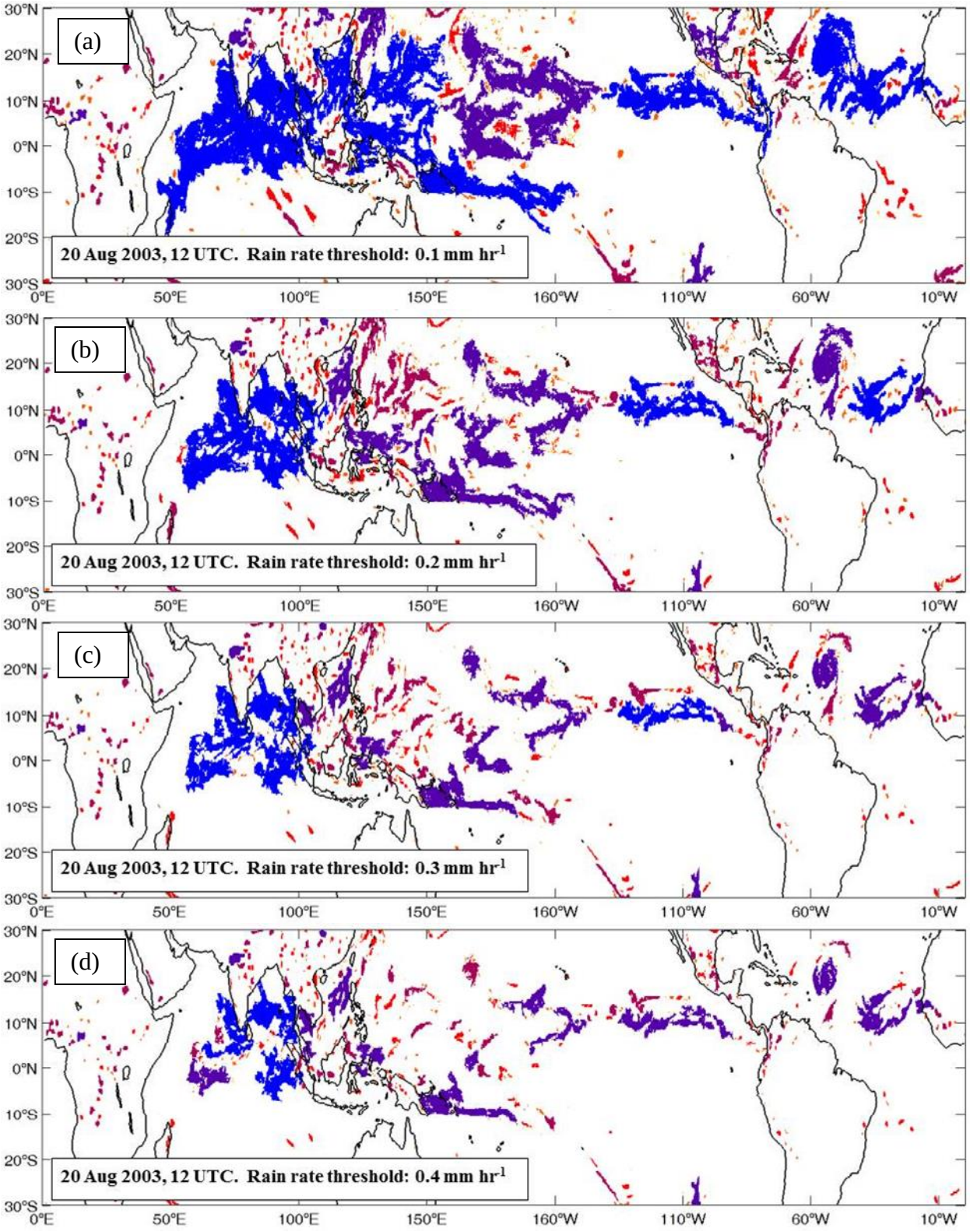
(a)
20 Aug 2003, 12 UTC. Rain rate threshold: 0.1 mm hr-1
(b)
20 Aug 2003, 12 UTC. Rain rate threshold: 0.2 mm hr-1
(c)
20 Aug 2003, 12 UTC. Rain rate threshold: 0.3 mm hr-1
(d)
20 Aug 2003, 12 UTC. Rain rate threshold: 0.4 mm hr-1
30°N
20°N
10°N
0°N
10°S
20°S
30°S
0°E
50°E
100°E
150°E
160°W
110°W
60°W
10°W

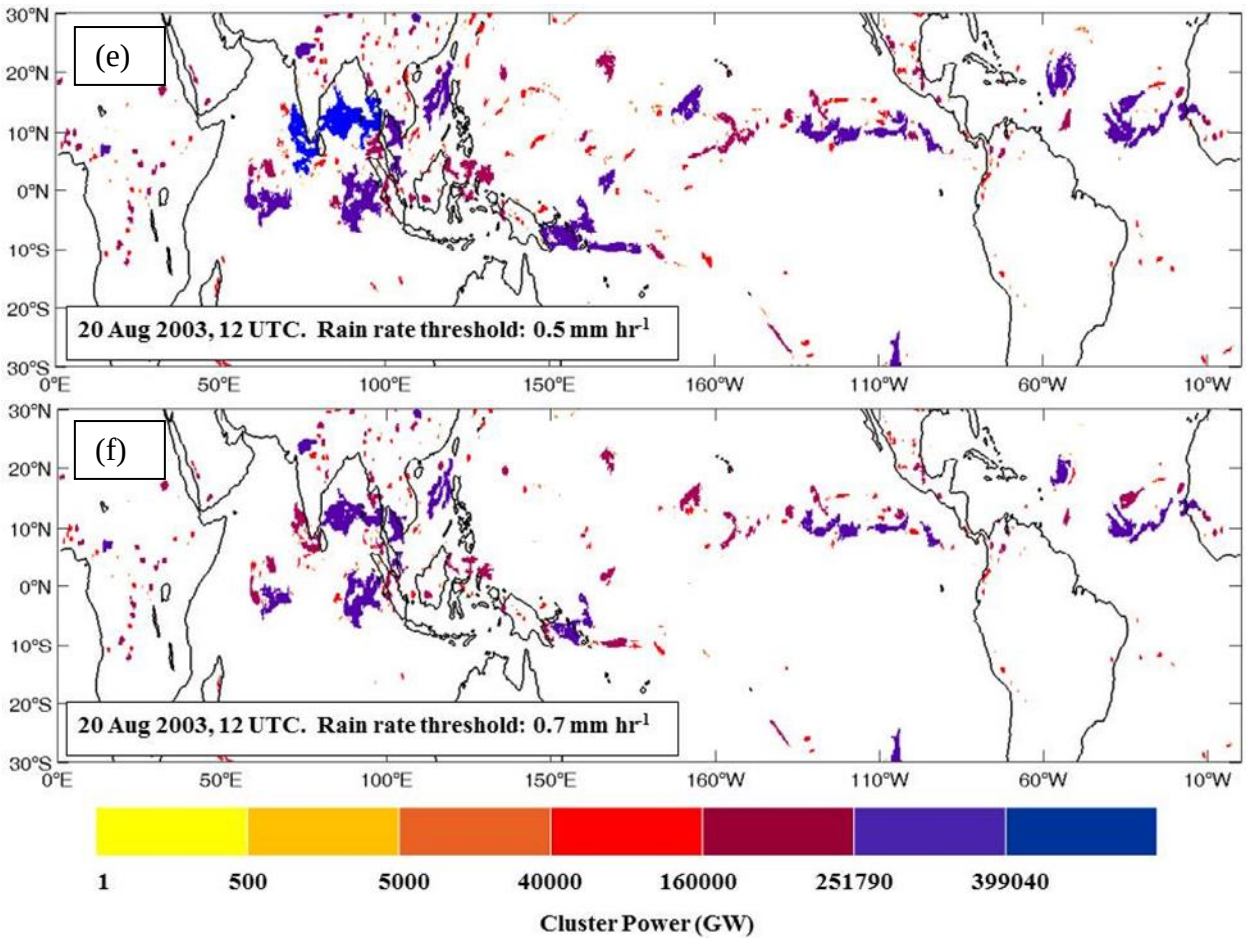

Fig. A3: A comparison of precipitation cluster morphology from a selected HIRAM-C360 AMIP time slice for rain rate thresholds 0.1 mm hr^{-1} to 0.7 mm hr^{-1}, as indicated.

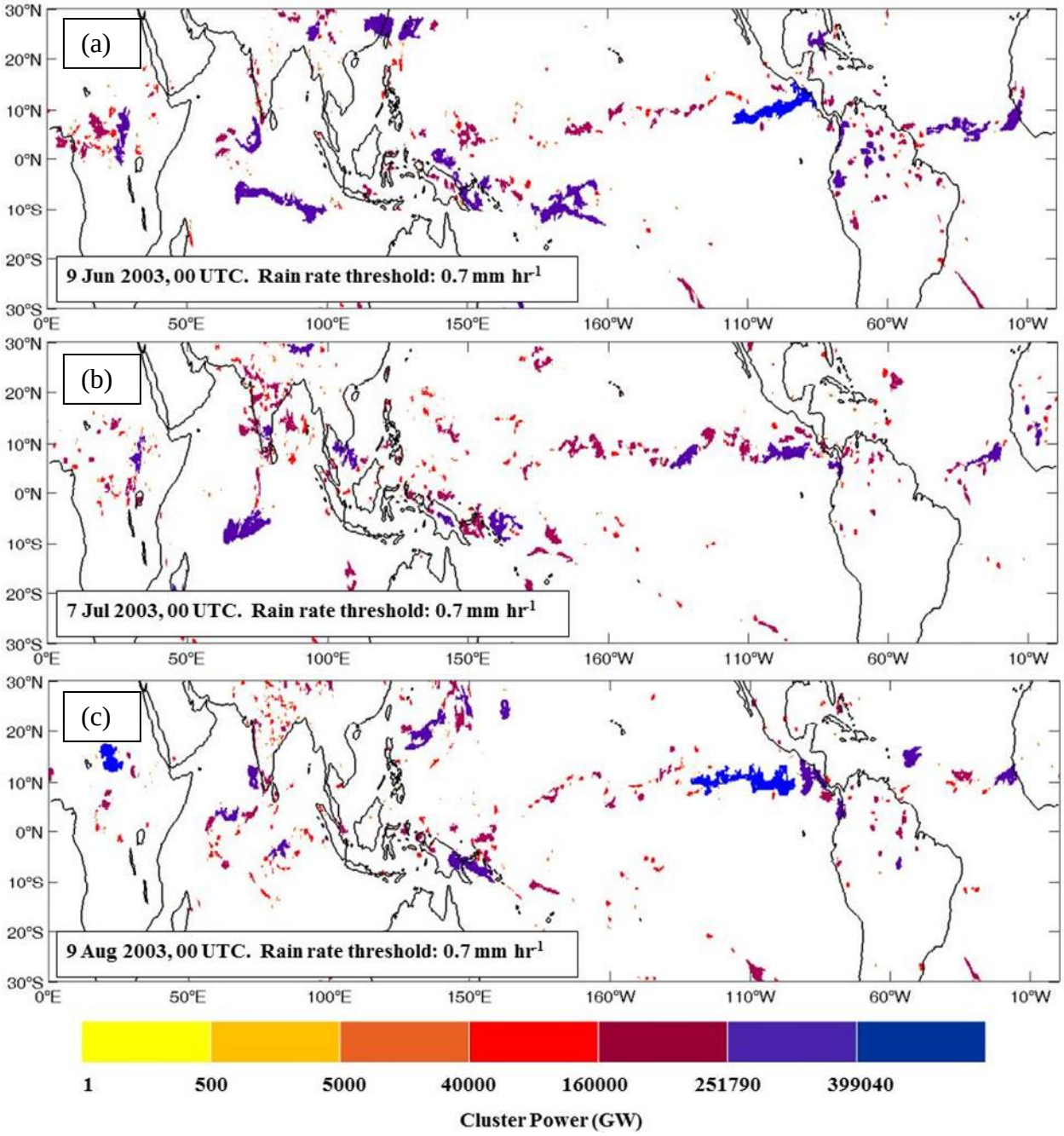

Fig. A4: Similar to Fig. 2.3 of the main text, but from selected HIRAM-C360 AMIP time slices for 0.7 mm hr^{-1} rain rate threshold.

References

Alexander, L. V., and Coauthors, 2006: Global observed changes in daily extremes of temperature and precipitation. *J. Geophys. Res. Atmos.*, **111**, D05109, doi: 10.1029/2005JD006290.

Allan, R. P., and B. J. Soden, 2008: Atmospheric warming and the amplification of precipitation extremes. *Science*, **321**, 1481-1484.

——, B. J. Soden, V. O. John, W. Ingram, and P. Good, 2010: Current changes in tropical precipitation. Environ. Res. Lett., **5**, 1-7, doi:10.1088/1748-9326/5/2/025205.

Arnold, N. P., and D. A. Randall, 2015: Global-scale convective aggregation: Implications for the Madden-Julian Oscillation. *J. Adv. Model. Earth Syst.*, **7**, 1499-1518, doi:10.1002/2015MS000498

Barros, V. R., and Coauthors, 2014: IPCC, 2014: *Climate Change 2014: Impacts, Adaptation, and Vulnerability. Part B: Regional Aspects. Contribution of Working Group II to the Fifth Assessment Report of the Intergovernmental Panel on Climate Change*. Cambridge University Press, 688 pp.

Bender, M. A., T. R. Knutson, R. E. Tuleya, J. J. Sirutis, G. A. Vecchi, S. T. Garner, and I. M. Held, 2010: Modeled impact of anthropogenic warming on the frequency of intense Atlantic hurricanes. *Science*, **327**, 454–458.

Beniston, M., and Coauthors, 2007: Future extreme events in European climate: an exploration of regional climate model projections. *Climatic Change*, **81(1)**, 71-95.

Bretherton, C. S., P. N. Blossey, and M. Khairoutdinov, 2005: An energy-balance analysis of deep convective self-aggregation above uniform SST. *J. Atmos. Sci.*, **62**, 4273-4292.

——, and M. Khairoutdinov, 2015: Convective self-aggregation feedbacks in near-global cloud-resolving simulations of an aquaplanet. *J. Adv. Model. Earth Syst.*, **7**, 1765-1787, doi: 10.1002/2015MS000499

Chen, J. H., and S. J. Lin, 2011: The remarkable predictability of inter-annual variability of Atlantic hurricanes during the past decade. *Geophys. Res. Lett.*, **38**, L11804, doi:10.1029/2011GL047629.

Dai, A., 2006: Precipitation characteristics in eighteen coupled climate models. *J. Climate*, **19**, 4605-4630, doi:10.1175/JCLI3884.1.

Easterling, D. R., G. A. Meehl, C. Parmesan, S. A. Chagnon, T. R. Karl, and L. O. Mearns, 2000: Climate extremes: Observations, modeling, and impacts. *Science*, **289**, 2068-2074, doi: 10.1126/science.289.5487.2068.

Emanuel, K. A., R. Sundararajan, and J. Williams, 2008: Hurricanes and global warming: Results from downscaling IPCC AR4 simulations. *Bull. Amer. Meteor. Soc.*, **89**, 347–367.

Geophysical Fluid Dynamics Laboratory (GFDL), 2015: Global atmospheric models. Accessed 30 November 2015. [Available online at http://www.gfdl.noaa.gov/atmospheric-model.]

Gualdi, S., E. Soccimarro, and A. Navarra, 2008: Changes in tropical cyclone activity due to global warming: Results from a high-resolution coupled general circulation model. *J. Climate*, **21**, 5204–5228.

Haensler, A., F. Saeed, D. Jacob, 2013: Assessing the robustness of projected precipitation changes over central Africa on the basis of a multitude of global and regional climate projections. *Climatic Change*, **121(2)**, 349-363.

Held, I. M. and M. Zhao, 2011: The response of tropical cyclone statistics to an increase in CO2 with fixed sea surface temperatures. *J. Climate*, **24**, 5353-5364, doi:10.1175/JCLI-D-11-00050.1.

Holloway, C. E., S. J. Woolnough, and G. M. Lister, 2012: Precipitation distributions for explicit versus parametrized convection in a large-domain high-resolution tropical case study. *Quart. J. Roy. Meteor. Soc.*, **138**, 1692–1708, doi:10.1002/qj.1903.

Hottovy, S., and S. N. Stechmann, 2015: A spatiotemporal stochastic model for tropical precipitation and water vapor dynamics. *J. Atmos. Sci.*, **72**, 4721-4738, doi:10.1175/JAS-D-15-0119.1.

Houze, R. A., 1982: Cloud clusters and large-scale vertical motions in the tropics. *J. Meteorol. Soc. Japan*, **60(1)**, 396-410.

——, 1989: Observed structure of mesoscale convective systems and implications for large-scale heating. *Quart. J. Roy. Meteor. Soc.*, **115**, 425-461.

——, 2004: Mesoscale convective systems, *Rev. Geophys.*, **42**, RG4003, doi:10.1029/2004RG000150.

Huffman, G. J., and Coauthors, 2007: The TRMM multisatellite precipitation analysis (TMPA): Quasi-global, multiyear, combined-sensor precipitation estimates at fine scales. *J. Hydrometeor.*, **8**, 38–55, doi:10.1175/JHM560.1.

Kay, G., and R. Washington, 2008: Future southern African summer rainfall variability related to a southwest Indian Ocean dipole in HadCM3. *Geophys. Res. Lett.*, **35**, L12701, doi: 10.1029/2008GL034180.

Kharioutdinov, M., and K. A. Emanuel, 2013: Rotating radiative-convective equilibrium simulated by a cloud-resolving model. *J. Adv. Model. Earth Syst.*, **5**, 816-825, doi: 10.1002/2013MS000253

Kharin, V. V., F. W. Zwiers, X. Zhang, and G. C. Hegerl, 2007: Changes in temperature and precipitation extremes in the IPCC Ensemble of Global Coupled Model Simulations. *J. Climate*, **20**, 1419–1444, doi:10.1175/JCLI4066.1.

——, and M. F. Wehner, 2013: Changes in temperature and precipitation extremes in the CMIP5 ensemble. *Climatic Change*, **119.2**, 345-357, doi:10.1007/s10584-013-0705-8.

Knutson, T. R., J. J. Sirutis, S. T. Garner, G. A. Vecchi, and I. M. Held, 2008: Simulated reduction in Atlantic hurricane frequency under twenty-first-century warming conditions. *Nat. Geosci.*, **1**, 359–364.

——, and Coauthors, 2010: Tropical cyclones and climate change. *Nat. Geosci.*, **3**, 157–163.

——, and Coauthors, 2013: Dynamical downscaling projections of twenty-first-century Atlantic hurricane activity: CMIP3 and CMIP5 model-based scenarios. *J. Climate*, **26(17)**, 6591-6617, doi:10.1175/JCLI-D-12-00539.1.

Landsea, C., and S. Delgado: TCFAQ E10) What Are the Average, Most, and Least Tropical Cyclones Occurring in Each Basin. Hurricane Research Division, Atlantic Oceanographic and Meteorological Laboratory, National Oceanic and Atmospheric Administration. Accessed 19 June 2015. [Available online at http://www.aoml.noaa.gov.hrd/tcfaq/E10.html.]

Leary, C. A., and R. A. Houze, 1979: The structure and evolution of convection in a tropical cloud cluster. *J. Atmos. Sci.*, **36**, 437–457, doi:10.1175/1520-0469(1979)036<0437:TSAEOC>2.0.CO;2.

Lenderink, G., and E. Van Meijgaard, 2008: Increase in hourly precipitation extremes beyond expectations from temperature changes. *Nature Geosci.,* **1(8)**, 511-514.

Mapes, B., and R. A. Houze, 1993: Cloud clusters and superclusters over the oceanic warm pool. *Mon. Wea. Rev.*, **121**, 1398-1415.

——, R. Milliff, and J. Morzel, 2009: Composite life cycle of maritime tropical mesoscale convective systems in scatterometer and microwave satellite observations. *J. Atmos. Sci.*, **66**, 199–208, doi:10.1175/2008JAS2746.1.

Merlis, T. M., M. Zhao, and I. M. Held, 2013: The sensitivity of hurricane frequency to ITCZ changes and radiatively forced warming in aquaplanet simulations. *Geophys. Res. Lett.*, **40**, 4109-4114, doi:10.1002/grl.50680.

Muller, C. J., and I. M. Held, 2012: Detailed Investigation of the self-aggregation of convection in cloud-resolving simulations. *J. Atmos. Sci*., **69**, 2551–2565, doi:10.1175/JAS-D-11-0257.1.

Peters, O., J. D. Neelin, and S. W. Nesbitt, 2009: Mesoscale convective systems and critical clusters. *J. Atmos. Sci.,* **66.9**, 2913-2924, doi:10.1175/2008JAS2761.1.

——, A. DeLuca, A. Corral, J. D. Neelin, and C. E. Holloway, 2010: Universality of rain event size distributions. *Journal of Statistical Mechanics: Theory and Experiment*, **11**, 1-15, doi:10.1088/1742-5468/2010/11/P11030.

——, K. Christensen, and J. D. Neelin, 2012: Rainfall and Dragon-Kings. *The European Physical Journal Special Topics*, **205.1**, 147-158, doi:10.1140/epjst/e2012-01567-5.

Seneviratne, S.I., and Coauthors, 2012: Changes in climate extremes and their impacts on the natural physical environment. *Managing the risks of extreme events and disasters to advance climate change adaptation*. Cambridge University Press, 121 pp.

Sillmann, J., V. V. Kharin, X. Zhang, F. W. Zwiers, and D. Bronaugh, 2013: Climate extremes indices in the CMIP5 multimodel ensemble: Part 1. Model evaluation in the present climate. *J. Geophys. Res. Atmos.*, **118**, 1716-1733, doi:10.1002/jgrd.50203.

——, 2013: Climate extremes indices in the CMIP5 multimodel ensemble: Part 2. Future climate projections. *J. Geophys. Res. Atmos.*, **118**, 2473–2493, doi:10.1002/jgrd.50188.

Skok, G., J. Bacmeister, and J. Tribbia, 2013: Analysis of tropical cyclone precipitation using an object-based algorithm. *J. Climate*, **26**, 2563-2579, doi:10.1175/JCLI-D-12-00135.1.

Stechmann, S. N., and J. D. Neelin, 2011: A stochastic model for the transition to strong convection. *J. Atmos. Sci.*, **68**, 2955-2970, doi:10.1175/JAS-D-11-028.1.

——, 2014: First-passage-time prototypes for precipitation statistics. *J. Atmos. Sci.*, **71**, 3269-3291, doi:10.1175/JAS-D-13-0268.1.

Stocker, T. F., and Coauthors, 2013: *Climate Change 2013: The Physical Science Basis. Contribution of Working Group I to the Fifth Assessment Report of the Intergovernmental Panel on Climate Change*. Cambridge University Press, 1535 pp.

Sylla, M. B., F. Giorgi, J. S. Pal, P. Gibba, I. Kebe, and M. Nikiema, 2015: Projected changes in the annual cycle of high-intensity precipitation events over west Africa for the late twenty-first century. *J. Climate*, **28**, 6475–6488, doi:10.1175/JCLI-D-14-00854.1.

Tan, J., C. Jakob, W. B. Rossow, and G. Tselioudis, 2015: Increases in tropical rainfall driven by changes in frequency of organized deep convection. *Nature*, **519**, 451-460, doi:10.1038/nature14339.

Tebaldi C., K. Hayhoe, J. M. Arblaster, and G. A. Meehl, 2006: Going to the extremes: An intercomparison of model-simulated historical and future changes in extreme events. *Climate Change*, **79**, 185–211. doi:10.1007/s10584-006-9051-4.

Tropical Rainfall Measuring Mission Project (TRMM), 2015: Daily TRMM and Others Rainfall Estimate (3B42 V7 derived), version 7. Goddard Space Flight Center Distributed Active Archive Center (GSFC DAAC). Accessed 01 July 2015. [Available online at http://disc.sci.gsfc.nasa.gov/datacollection/TRMM_3B42_daily_V7.html.]

Villarini, G., D. Lavers, E. Scoccimarro, M. Zhao, M. Wehner, G. Vecchi, T. Knutson, and K. Reed, 2014: Sensitivity of tropical cyclone rainfall to idealized global scale forcings. *J. Climate*, **27**, 4622-41, doi:10.1175/JCLI-D-13-00780.1.

Vizy, E. K., and K. H. Cook, 2012: Mid-twenty-first-century changes in extreme events over northern and tropical Africa. *J. Climate*, **25**, 5748–5767, doi:10.1175/JCLI-D-11-00693.1.

Webster, P. J., G. J. Holland, J. A. Curry, and H.-R. Chang, 2005: Changes in tropical cyclone number, duration, and intensity in a warming environment. *Science*, **309**, 1844– 1846.

Wehner, M., M. Prabhat, K. A. Reed, D. Stone, W. D. Collins, and J. Bacmeister, 2015: Resolution dependence of future tropical cyclone projections of CAM5.1 in the U.S. CLIVAR hurricane working group idealized configurations. *J. Climate*, **28**, 3905-3925, doi: 10.1175/JCLI-D-14-00311.1.

Wing, A. A., and K. A. Emanuel, 2014: Physical mechanisms controlling self-aggregation of convection in idealized numerical modeling simulations. *J. Adv. Model. Earth Syst.*, **6**, 59–74, doi:10.1002/2013MS000269.

——, and T. W. Cronin, 2015: Self-aggregation of convection in long channel geometry. *Quart. J. Roy. Meteor. Soc.*, **142**, 1-15, doi:10.1002/qj.2628.

Wood, R., and P. R. Field, 2011: The distribution of cloud horizontal sizes. *J. Climate*, **24**, 4800-4816, doi:10.1175/2011JCLI4056.1.

Zhao, M., I. M. Held, S. J. Lin, and G. A. Vecchi, 2009: Simulations of global hurricane climatology, interannual variability, and response to global warming using a 50-km resolution GCM. *J. Climate*, **22**, 6653-6678, doi:10.1175/2009JCLI3049.1.

——, I. M. Held, and G. A. Vecchi, 2010: Retrospective forecasts of the hurricane season using a global atmospheric model assuming persistence of SST anomalies. *Mon. Wea. Rev.*, **138**, 3858-3868, doi:10.1175/2010MWR3366.1.

——, and I. M. Held, 2011: An analysis of the effect of global warming on the intensity of Atlantic hurricanes using a GCM with statistical refinement. *J. Climate*, **23**, 6382-6393, doi:10.1175/2010JCLI3837.1.

——, 2012: TC-permitting GCM simulations of hurricane frequency response to sea surface temperature anomalies projected for the late-twenty-first-century. *J. Climate*, **25**, 2995-3009, doi: 10.1175/JCLI-D-11-00313.1.

3 Distributions of Tropical Precipitation Cluster Power and Their Changes Under Global Warming: Part II

3.1 Abstract

Distributions of precipitation cluster power (latent heat release rate integrated over contiguous precipitating pixels) are examined in 1-2° resolution members of the Coupled Model Intercomparison Project Phase 5 (CMIP5) climate model ensemble. These approximately reproduce the power law range and large event cutoff seen in observations and the High Resolution Atmospheric Model (HIRAM) at 0.25-0.5° in Chapter 2. Under the Representative Concentration Pathway (RCP) 8.5 global warming scenario, the change in the probability of the most intense precipitation clusters appears in all models and is consistent with HIRAM output, increasing by up to an order of magnitude relative to historical climate. For the three models in the ensemble with continuous time series of high resolution output, there is substantial variability on when these probability increases for the most powerful precipitation clusters become detectable, ranging from detectable within the observational period to statistically significant trends emerging only after 2050. A similar analysis of National Centers for Environmental Prediction (NCEP) Reanalysis 2 and Special Sensor Microwave Imager and Sounder (SSM/I and SSMIS) rain rate retrievals in the recent observational record does not yield reliable evidence of trends in high-power cluster probabilities at this time. However, the results suggest that maintaining a consistent set of overlapping satellite instrumentation with improvements to SSM/I-SSMIS rain rate retrieval inter-calibrations would be useful for detecting trends in this important tail behavior within the next couple of decades.

3.2 Introduction

Characterizing the current state of organized tropical convection and projected changes under global warming is important due to the potentially large socioeconomic impacts associated with such changes. A survey of studies examining Coupled Model Intercomparison Project Phase 3 (CMIP3) and CMIP5 coupled climate models shows a projected increase in extreme precipitation event frequency and intensity by the end of the 21st Century (e.g., Tebaldi et al. 2006; Kharin et al. 2007, 2013; Sillmann et al. 2013), though uncertainties emerge in both observational (e.g., Easterling et al. 2000; Alexander et al. 2006; Kharin et al. 2007, 2013; Lenderink and Van Meijgaard 2008; Allan et al. 2010) and global scale modeling research (e.g., Tebaldi et al. 2006; Kharin et al. 2007, 2013; Allan and Soden 2008; Allan et al. 2010; Sillmann et al. 2013) in recent and future climate. One potential source of uncertainty in extreme precipitation projections is an inadequate representation of important physical processes associated with convection in climate models (e.g., Kharin et al. 2007) including convective organization (e.g., Tan et al. 2015). With the advent of high spatial and temporal space-borne passive microwave imagers, much has been learned about convective organization based on satellite retrieved precipitation products (e.g., Huffman et al. 2007; Allan and Soden 2008; Allan et al. 2010), though such platforms are not without limitations (e.g., McCollum and Ferraro 2003; Hilburn and Wentz 2008; Bowman et al. 2009; Allan et al. 2010; Chen et al. 2013). There is thus a need for studies that examine measures of convective organization in observations, in comparison to models and in terms of their potential changes under global warming.

In Chapter 2, we build an observational baseline of tropical precipitation integrated over contiguous clusters using high resolution satellite data with complete spatial coverage.

This is motivated by previous observational studies of cluster behavior in various space or time measures (Mapes et al. 2009; Peters et al. 2009, 2010, 2012; Wood and Field 2011; Skok et al. 2013). The integrated precipitation over a cluster can equivalently be expressed as an integrated latent heat release or cluster power. The probability distribution of cluster power is shown to follow a long, scale-free power law, with a distinct cutoff, i.e. a more rapid drop in probability at high power. We then show that the High Resolution Atmospheric Model (HIRAM) with prescribed sea surface temperatures (SST) at 2 resolutions accurately simulates these observed cluster power statistics. We also examine HIRAM output from middle and end-of-century simulations, finding large increases in the frequency of the most powerful clusters under a "business as usual" global warming scenario. These increases exceed those expected under simple Clausius-Clapeyron scaling of precipitation.

Here, we compare Special Sensor Microwave Imager (SSM/I) and Special Sensor Microwave Imager/Sounder (SSMIS) cluster power distributions with Tropical Rainfall Measuring Mission (TRMM) 3B42 data, to ensure consistency across satellite rain rate retrievals. We then examine cluster power distributions over the SSM/I-SSMIS observational record to check for changes in the frequency of the most powerful precipitation clusters in recent climate. Trends uncovered in the analysis of the satellite data record are next compared to an analysis of cluster power distributions from the National Centers for Environmental Prediction (NCEP) Reanalysis 2 observationally-constrained modeled precipitation dataset. We then analyze cluster power distributions from an ensemble of high resolution models from the Coupled Model Intercomparison Project Phase 5 (CMIP5) under the Representative Concentration Pathway (RCP) 8.5 global warming scenario. We i) check if the model ensemble adequately reproduces cluster power distributions in current climate in observations and in

HIRAM; ii) verify that coupled models yield end-of-century changes consistent with those simulated in HIRAM; and iii) conduct a time series analysis of the probabilities of clusters from the highest-power bins to inform expectations for detectability.

3.3 Data and Methods

Observational rain rate data are retrieved from the SSM/I and SSMIS platforms onboard polar orbiting Defense Meteorological Satellite Program (DMSP) satellites. The SSM/I platform flew onboard the F08, F10, F11, F13, F14, and F15 DMSP satellites from 1987-2009 (Wentz 2013). SSMIS data come from the F16 and F17 DMSP satellites, beginning in May 2004 (Wentz et al. 2012). Our goal is to use cluster power computed from the SSM/I-SSMIS time series as a reliable indicator of recent historical cluster power behavior because the period for which SSM/I-SSMIS data are available (1987-present) is longer than the period over which TRMM-3B42 data (1998-2015) are available, presenting a more complete observational record of tropical precipitation data.

SSM/I-SSMIS rain rate data are retrieved using the V7 algorithm (in mm hr^{-1}), are available twice daily, over oceans, at 0.25^0 x 0.25^0 latitude-longitude resolution (Wentz et al. 2012), and similar to Part I, we confine our time domain to 1 May to 30 September. Rain rates and other data retrieved from these platforms are highly inter-calibrated, with further details noted in Wentz et al. (1998, 2012, 2013) and Yan and Weng (2008). Since SSMIS swath width is 300 km wider than SSM/I swath width (NSIDC 2016), we also test SSM/I-SSMIS cluster power distributions for sensitivity to the swath width difference over the complete SSM/I-SSMIS platform overlap period (2004-2009) by comparing SSM/I, SSMIS, and SSMIS cluster power distributions that have had their swath width narrowed to match SSM/I swath width. On

average, each SSM/I swath is 16 pixels narrower than each SSMIS swath over the Tropics between 30^0S - 30^0N, so to match SSM/I and SSMIS swath widths, we run a simple procedure that masks eight pixels on each side of every SSMIS swath prior to running our clustering and binning procedures.

We first compare SSMIS cluster power distributions for 2004-2009, examining cluster power sensitivity to the same minimum rain rate thresholds used in Chapter 2. Then, we compare the cluster power distribution at the highest minimum rain rate threshold used in this study (0.7 mm hr^{-1}) from the TRMM-3B42 retrieval to SSM/I-SSMIS distributions at the same threshold retrieved over 2004-2009, assessing storm cluster behavior across multiple satellite rain rate retrievals. As noted in Chapter 2, TRMM-3B42 rain rate data (here, 2004-2009 only) are merged from sensors onboard the TRMM spacecraft and other satellites to provide 3-hourly rain rate retrievals (mm hr^{-1}) at 0.25^0 x 0.25^0 latitude-longitude resolution, over land and ocean (Huffmann et al. 2007; Huffmann and Blovin 2014; TRMM 2015). TRMM-3B42 rain rate retrievals from only 00 UTC and 12 UTC are included in this study, in order to optimize the comparison with twice-daily SSM/I-SSMIS data.

Next, we evaluate cluster power behavior in recent climate using an observationally-constrained model. Modeled precipitation flux data (kg m^{-2} s^{-1}) from the National Centers for Environmental Prediction (NCEP) Reanalysis 2 dataset present a data record extending back to 1979, so are compared against satellite retrievals to characterize trends in cluster power behavior in the historical period. NCEP Reanalysis 2 data are available every six hours at a horizontal resolution of approximately 2^0 Lat x 2^0 Lon (Kanamitsu et al. 2002), though only data from 00 UTC and 12 UTC are incorporated here.

Modeling center or group (institute ID)	CMIP5 model	Resolution (Lat x Lon)	Data Availability
National Center for Atmospheric Research (NCAR)	CCSM4	1.0 x 1.25	1979-2005, 2026-2045, 2081-2100
Centre National de Recherches Meteorologiques (CNRM)	CNRM-CM5	1.4 x 1.4	1979-2005, 2026-2045, 2081-2100
EC-EARTH consortium (EC-EARTH)	EC-EARTH	1.12 x 1.125	1979-2100
Met Office Hadley Centre (MOHC)	HadGEM2-ES	1.25 x 1.875	1979-2005, 2026-2045, 2081-2099
Institute for Numerical Mathematics (INM)	INM-CM4	1.5 x 2.0	1979-2005, 2026-2045, 2081-2100
Atmosphere and Ocean Research Institute (The University of Tokyo), National Institute for Environmental Studies, and Japan Agency for Marine-Earth Science and Technology (MIROC)	MIROC5	1.4 x 1.4	1979-2100
Meteorological Research Institute (MRI)	MRI-CGCM3	1.1 x 1.1	1979-2100

Table 3.1: CMIP5 modeling centers and models used, with specified spatial resolution and data availability.

Lastly, we examine if a suite of coupled CMIP5 models (Table 2.1), chosen for relatively high spatial (e.g., less than 2^0) and temporal (e.g., 3-hourly) resolution, exhibits changes in frequency and intensity of the most powerful precipitation clusters in recent, mid-century, and end-of-century climate under RCP8.5. In Chapter 2 we find that the portion of the distribution showing the most change corresponds to the events likely to have the most impact (i.e., highest cluster power), so we i) analyze if the probability of precipitation clusters from the highest-power bins increases in the future, ii) quantify the magnitude of such probability changes, and iii) determine when changes first become detectable (as a statistically significant linear trend) compared to climatology. As in Chapter 2, we only include cluster power data from 00 UTC and 12 UTC, follow the same clustering procedure and cluster power calculation, and confine our analysis to the Tropics (globally from 30^0N-30^0S) from 1 May to 30 September.

To calculate cluster power, we follow a similar contiguous precipitating pixel approach described in Peters et al. (2012) and Chapter 2, first masking cells not meeting the 0.7 mm hr^{-1}

minimum rain rate threshold. Contiguous precipitating cells with rain rates meeting this threshold then have their rain rates converted to the instantaneous latent heat release per grid cell, which are in turn integrated over a cluster to obtain cluster power, in units of gigawatts (GW). We convert rain rate into a measure of latent heat release as it quantifies the instantaneous amount of energy released over a storm and directly ties into the Earth's energy budget.

To ensure that we have enough counts for statistical analysis in the uppermost power bins, our binning procedure in building probability distributions is as follows. Bins are chosen with a nominal width that is constant in log space, so that the bin width increases smoothly as probabilities drop. The increments of cluster size are quantized to multiples of the minimum cluster size, so to ensure that the bin spacing is consistent with this, bin widths are adjusted to the integer multiple of the minimum cluster size that is closest to the nominal bin width. In practice this affects only the lower bins. After an initial binning with nominal log bin width of 0.2, the number of clusters in the highest-power non-zero bin in the historical period is examined. If the number of clusters in the highest-power non-zero bin in the historical period is less than an average of one cluster per year, we increase the nominal bin width slightly (roughly 1% in log space typically suffices) and redo the binning procedure, checking that the number of bins with nonzero counts is decreased by 1. Because probabilities are dropping steeply near the highest bin, the small shift of the bin boundaries is sufficient to increase cluster counts in the highest bin. We then apply the same bin boundaries to future climate runs of the same dataset. In practice, this simple adjustment procedure yields improved statistical significance for the highest bin for comparison between recent climate and future climate output.

3.4 Analysis

3.4.1 Cluster Power Distributions and Probability Trends for High-Power Clusters in Observations (Fig. 3.1-3.4)

We evaluate the current state of tropical cluster power behavior across multiple satellite retrievals (SSM/I, SSMIS, and TRMM-3B42) and an observationally constrained model (NCEP Reanalysis 2) in Fig. 3.1, investigating if cluster power distributions for recent climate mirror the general behavior described in Chapter 2. In Fig. 3.2 and 3.3, we examine the SSMIS retrieval for changes in the probability of the most powerful precipitation clusters resulting from the swath width difference between the SSM/I and SSMIS platforms. We first inter-compare rain rate percentiles from the SSM/I and matched-swath-width SSMIS datasets, then analyze probability densities from the highest-power bins for the SSM/I, SSMIS, and matched-swath-width SSMIS datasets. As shown in Chapter 2, the largest changes in cluster power behavior occur in the high-power bins beyond the cutoff. So, in Fig. 3.3 and 3.4, we perform a time series analysis of the probability density of clusters in the four uppermost high-power bins for SSM/I-SSMIS datasets and NCEP Reanalysis 2 output for which sufficient counts are available, describing any changes to the frequency of precipitation clusters in the most powerful bins.

Cluster power distributions (Fig. 3.1, bottom) from the SSMIS platform (F16) at multiple rain rate thresholds display little sensitivity while also having similar scale-free power law ranges and cutoffs as the TRMM-3B42 cluster power distributions in Chapter 2. In the middle set of curves, the observed cluster power distributions for SSM/I (F13), SSMIS, and matched-swath-width SSMIS datasets at the 0.7 mm hr^{-1} rain rate threshold all have the same scale-free power law range and cutoff, closely paralleling the TRMM-3B42 cluster power

distribution with a sharp drop in the frequency of precipitation clusters in the highest-power bins beyond 10^5 GW. Beyond the cutoff, the tail of the TRMM-3B42 distribution shifts towards higher power and includes two extra high-power bins compared to the SSM/I-SSMIS distributions. The TRMM-3B42 dataset contains merged rain rates from multiple platforms, so unlike SSM/I-SSMIS platforms, there are no gaps in spatial coverage that limit cluster area. This implies that TRMM-3B42 output includes larger clusters, which results in the TRMM-3B42 distribution containing two extra high-power bins.

SSM/I-SSMIS and TRMM-3B42 data records only extend back to 1987 and 1998, respectively. For a more complete picture of cluster power behavior in recent climate, we analyze cluster power behavior in the NCEP Reanalysis 2 precipitation dataset, whose data record begins in 1979. NCEP Reanalysis 2 cluster power distributions for 1979-2014 at the 0.7 mm hr^{-1} rain rate threshold (for entire timeframe and 7-8 year subsets) are plotted in the top set of curves in Fig. 3.1. For reference, the NCEP Reanalysis 2 cluster power distribution from 2004-2009 is re-plotted with the middle set of curves to compare with observed data. Because the NCEP Reanalysis 2 output has a comparatively coarse resolution, its scale-free, power law range begins at higher power and contains fewer bins than the observed scale-free, power law range. Even so, Reanalysis cluster power distributions qualitatively agree with observed data, with a slight shift in the cutoff towards higher power. Furthermore, we find little variation in cluster power behavior between 1979 and 2014, the implications of which will be further examined in Fig. 3.4.

SSM/I (F13) and matched-swath-width SSMIS (F16) rain rate retrievals for May-September 2004-2009 display a high degree of agreement, suggesting consistency of inter-calibration (Fig. 3.1 and 3.2), consistent with previous SSM/I-SSMIS calibration research

noted in Yan and Weng (2008) and Sun and Feng (2008). SSM/I-matched-swath-width SSMIS cluster power distributions closely parallel each other (Fig. 3.1), rain rate percentiles correlate highly (r = 0.9987, Fig. 3.2), and the least squares best-fit line through the rain rate percentiles is nearly one-to-one (Fig. 3.2), suggesting that the current inter-calibration should suffice for most purposes. Furthermore, we expect that that by matching SSMIS and SSM/I swath widths, we should be able to construct a complete time series of observed cluster power behavior since 1987.

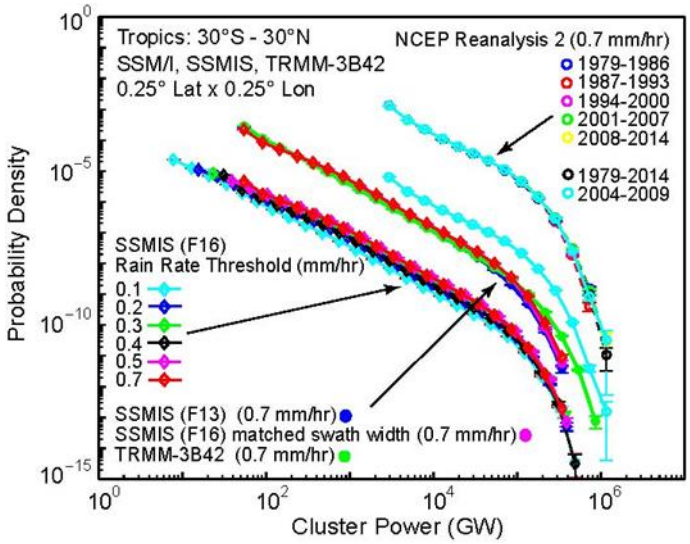

Fig. 3.1: (Bottom) Probability distributions of cluster power, i.e., precipitation integrated over clusters of contiguous pixels exceeding the specified rain rate threshold, from the SSMIS (F16 satellite) precipitation product over the Tropics for 1 May-30 September 2004-2009, shifted down one decade vertically for readability. (Middle) Comparison of cluster power probability distributions for the 0.7 mm hr^{-1} rain rate threshold from TRMM-3B42, SSM/I (F13 satellite), matched-swath-width SSMIS (F16 satellite), and NCEP Reanalysis 2 precipitation products, 1 May-30 September 2004-2009. (Top) NCEP Reanalysis 2 precipitation product cluster power probability distributions for the 0.7 mm hr^{-1} rain rate threshold for 1979-2014, subdivided into periods shown, shifted up two degrees vertically for readability.

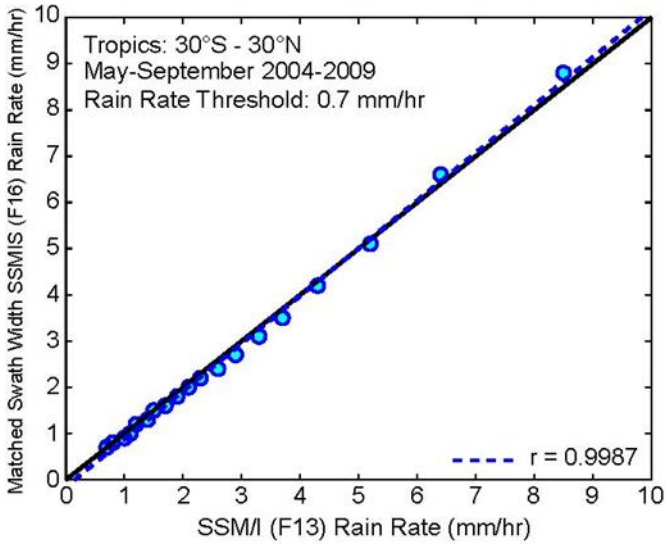

Fig. 3.2: Scatterplot of rain rate percentiles meeting the 0.7 mm hr^{-1} rain rate threshold from SSM/I (F13 satellite) and matched-swath-width SSMIS (F16 satellite) precipitation products, 1 May-30 September 2004-2009. The correlation coefficient between precipitation products, least squares best-fit line and one-to-one line are also plotted for reference (from 0 to 10 mm hr^{-1}).

Figure 3.3 contains overlapping probability densities broken out by the four highest-power bins for all satellites carrying the SSM/I and SSMIS platforms for 1987-2015. The gap between SSM/I and SSMIS time series indicates that the precision of inter-calibration needed to construct a continuous SSM/I-SSMIS time series of probability in these upper bins does not appear to be met by the current inter-calibration. It may also be noted that the swath width matching procedure appears to have a modest impact in connecting the SSM/I-SSMIS time series. When trends in the cluster probabilities in the four highest bins 17-20 are computed over the entire time series, each gives a statistically significant positive trend (by a Student's t-test at the 95% level). Thus a naïve blending of the satellite series might appear to give a positive trend. However, given the apparent calibration jump between the SSM/I and SSMIS time series for bins 17-19, this serves as a cautionary statement on the necessity of carefully examining the calibration. Probability trends for cluster probabilities for power within the highest bins 17-19 are computed separately for each of the SSM/I and SSMIS platforms; for

the short time series for the separate platforms, these trends fail to pass a Student's t-test at the 95% level. For the highest-power bin (bin 20), there is less calibration jump between the SSM/I and SSMIS time series. However, one should be duly cautious regarding the statistically significant increase in probability in this bin given the calibration issues noted in the others. A more careful inter-calibration of these satellites could potentially permit trend detection for cluster probabilities.

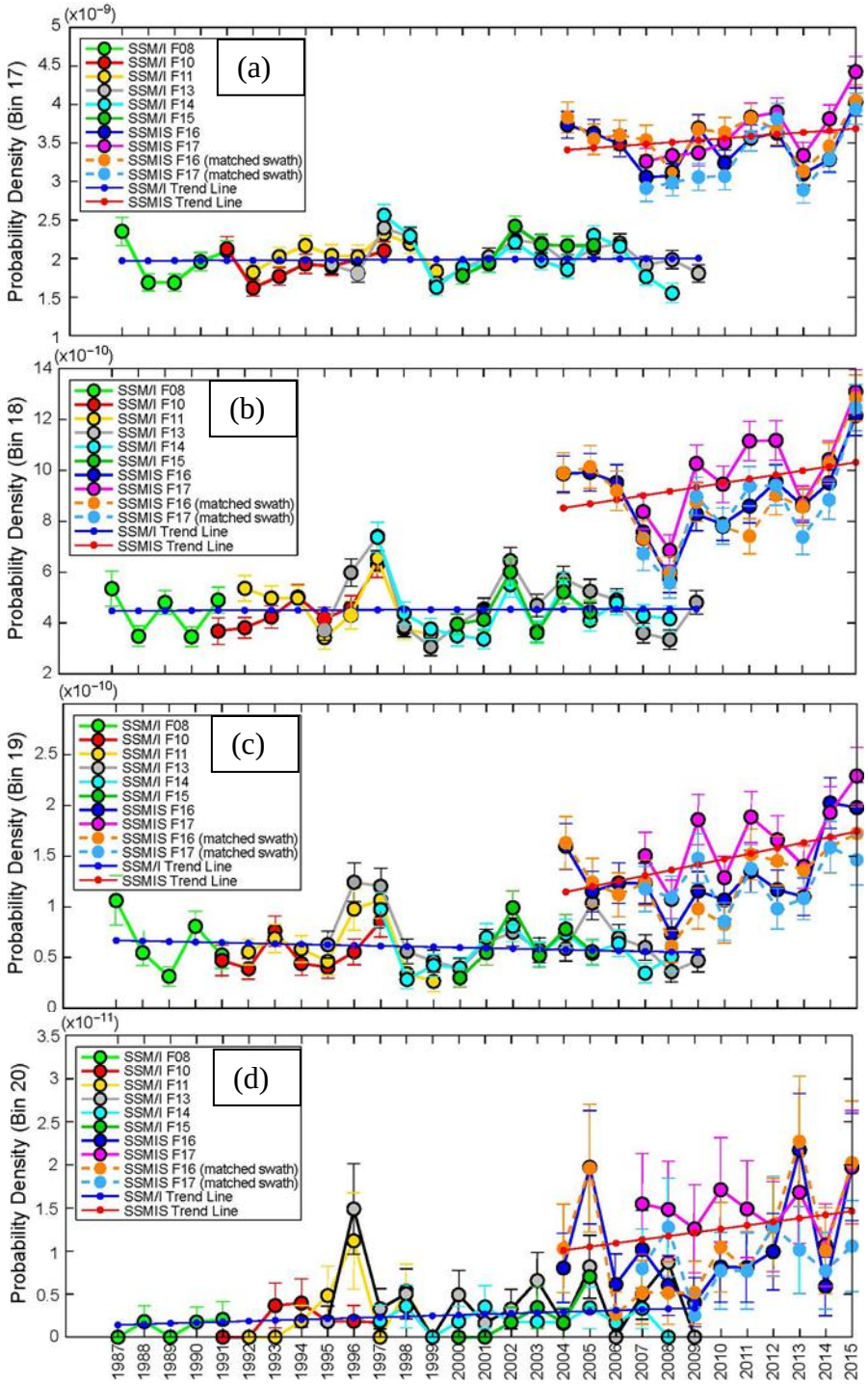

Fig. 3.3: Time series plots of probability densities from the four highest cluster power bins for which statistics can be computed (bins 17-20) for each SSM/I, SSMIS, and matched-swath-width SSMIS precipitation product for the 0.7 mm hr^{-1} rain rate threshold, 1 May-30 September 1987-2015. Also plotted are least squares best-fit trend lines for the SSM/I and SSMIS platforms.

In Fig. 3.4 we also check for an upward trend in the probability of high-power precipitation clusters in recent climate by analyzing time series plots of probability densities from four of the five highest-power bins using NCEP Reanalysis 2 model output. The time series from the highest-power bin (bin 14) is excluded due to insufficient storm counts over the observed period. The upward trend line in bin 10 (Fig. 3.4a), of approximately 15% increase over the 26 year period, passes a Student's t-test at the 95% level. However, the trends in bins 11-13 do not pass this test at the 95% level, possibly associated with the fewer counts per bin in these higher bins. For the signature seen in Chapter 2 in end-of-century runs, the expectation would be for consistency of trend among the high-power bins, i.e., consistency of the upward trend displayed in bin 10 with a corresponding increase in the probability of precipitation clusters in bins 11-13. While these results do not preclude tends being detectable in other measures, it does indicate difficulty in detecting significant trends for detailed breakdown of the changes in probability of high-power precipitation clusters in recent climate.

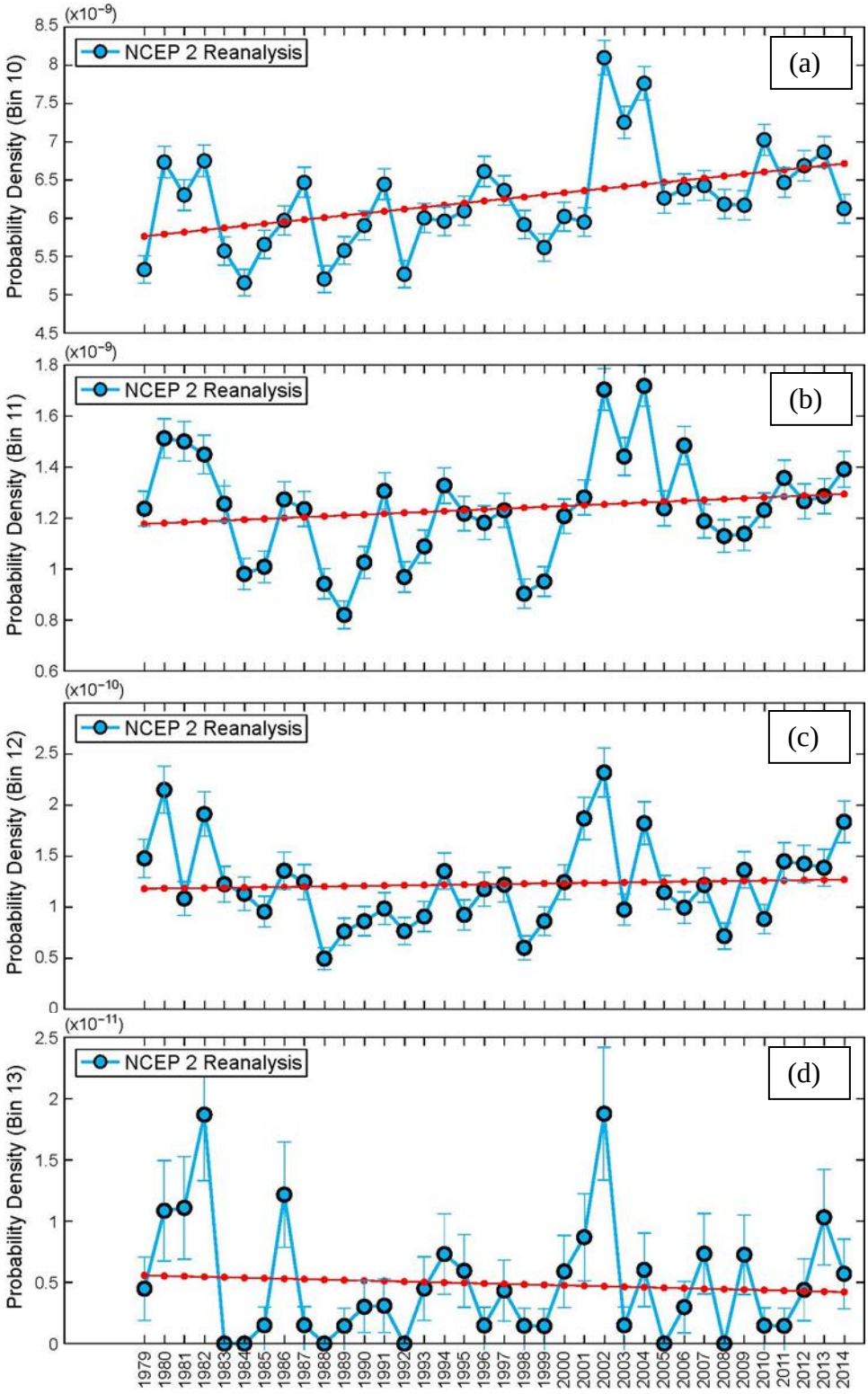

Fig. 3.4: Same as Fig. 3.3, but for the NCEP Reanalysis 2 precipitation product.

3.4.2 Cluster Power Distributions and Probability Trends for High-Power Clusters in CMIP5 Models (Fig. 3.5-3.8)

In Chapter 2 historical and future cluster power distributions from a high resolution atmosphere model at two horizontal resolutions (HIRAM-C360 and C180) are analyzed. When compared to observed (e.g., TRMM-3B42) cluster power statistics, cluster power distributions at both resolutions compare favorably with each other and observations, with a similar scale-free, power law range, cutoff near 10^5 GW, and sharp decrease in the probability of the most intense precipitation clusters thereafter. Additionally, the behavior of the HIRAM cluster power distributions shows little resolution dependence but in the region of greatest impact (e.g., the highest cluster power bins beyond the cutoff), high sensitivity to a minimum rain rate threshold. Without attempting to examine when a signal emerges, we also find that the probability of precipitation clusters from the region of greatest impact increases, relative to recent climate, by a factor ranging from 3 for the third highest-power bin to a factor of 20 for the highest-power bin by end-of-century. In Fig. 3.5-3.8, we investigate cluster power behavior from a suite of seven high resolution CMIP5 models under the RCP 8.5 scenario for recent, mid-century, and end-of-century climate. Figure 3.5 displays cluster power distributions from the model ensemble with their corresponding changes to the frequency of the highest-power precipitation clusters by middle and end-of-century, relative to recent climate, and Fig. 3.6-3.8 examine when a statistically significant signal emerges for the 3 CMIP5 models in our study that have a continuous time series of data available for 1979-2100.

Cluster power distributions in Fig. 3.5 indicate that our ensemble of CMIP5 models generally have similar scale-free, power law ranges, cutoffs, and sharp decreases thereafter as observations and HIRAM model output. There is a substantial increase in the frequency of clusters (up to an order of magnitude) with power in the highest bins by end-of-century, also

similar to HIRAM projections. Changes by mid-century are less clear. Three CMIP5 models (CNRM-CM5, INMCM4, and MIROC5) exhibit little to no change in cluster power behavior by mid-century, while the other models (HadGEM2-ES, CCSM4, EC-EARTH, and MRI-CGCM3) are more consistent with mid-century projections displayed by the HIRAM simulations in Chapter 2.

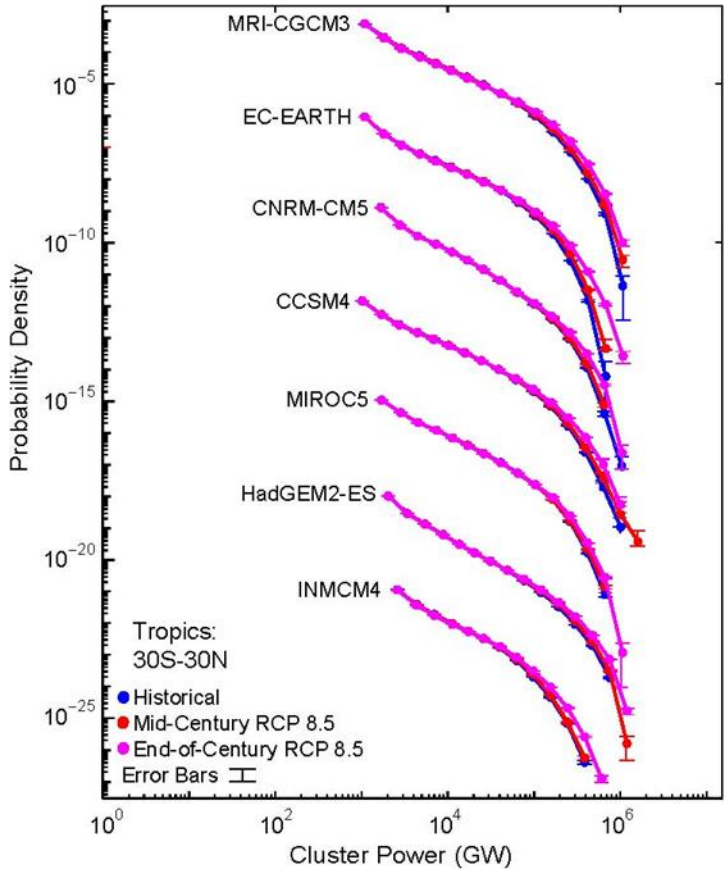

Fig. 3.5: Historical, mid-century, and end-of-century cluster power probability distributions from seven high-resolution CMIP5 models for the 0.7mm hr^{-1} rain rate threshold. For readability, all cluster power probability distributions except for MRI-CGCM3 have been shifted vertically down by 3 to 18 decades, respectively. Historical period: 1979-2005. Mid-century RCP 8.5 period: 2026-2045 (CNRM-CM5, CCSM4, HadGEM2-ES, INMCM4), 2025-2050 (MRI-CGCM3, EC-EARTH, MIROC5). End-of-century RCP 8.5 period: 2081-2100 (CNRM-CM5, CCSM4, HadGEM2-ES, INMCM4), 2075-2100 (MRI-CGCM3, EC-EARTH, MIROC5).

Additionally, the three models with continuous data through end-of-century (Fig. 3.6-3.8) have considerable spread as to when changes to the probability of the most intense storms become detectable. For the MRI-CGCM3 model (Fig. 3.6), a statistically significant upward trend (using a Student's t-test at the 95% level) emerges between 2020 and 2033. Bin 12 shows a statistically significant upward trend detectable by 2020, comparable to the trend that emerges by 2014 in bin 10 of the NCEP Reanalysis 2 dataset. Precipitation clusters having power falling within bins 12-14 become 2 (bin 12) to 4 times (bin 14) more frequent by end-of-century, relative to their historical mean values (1979-2014), and the frequency of storms from the highest-power bin (bin 15) increases by a factor of 7.

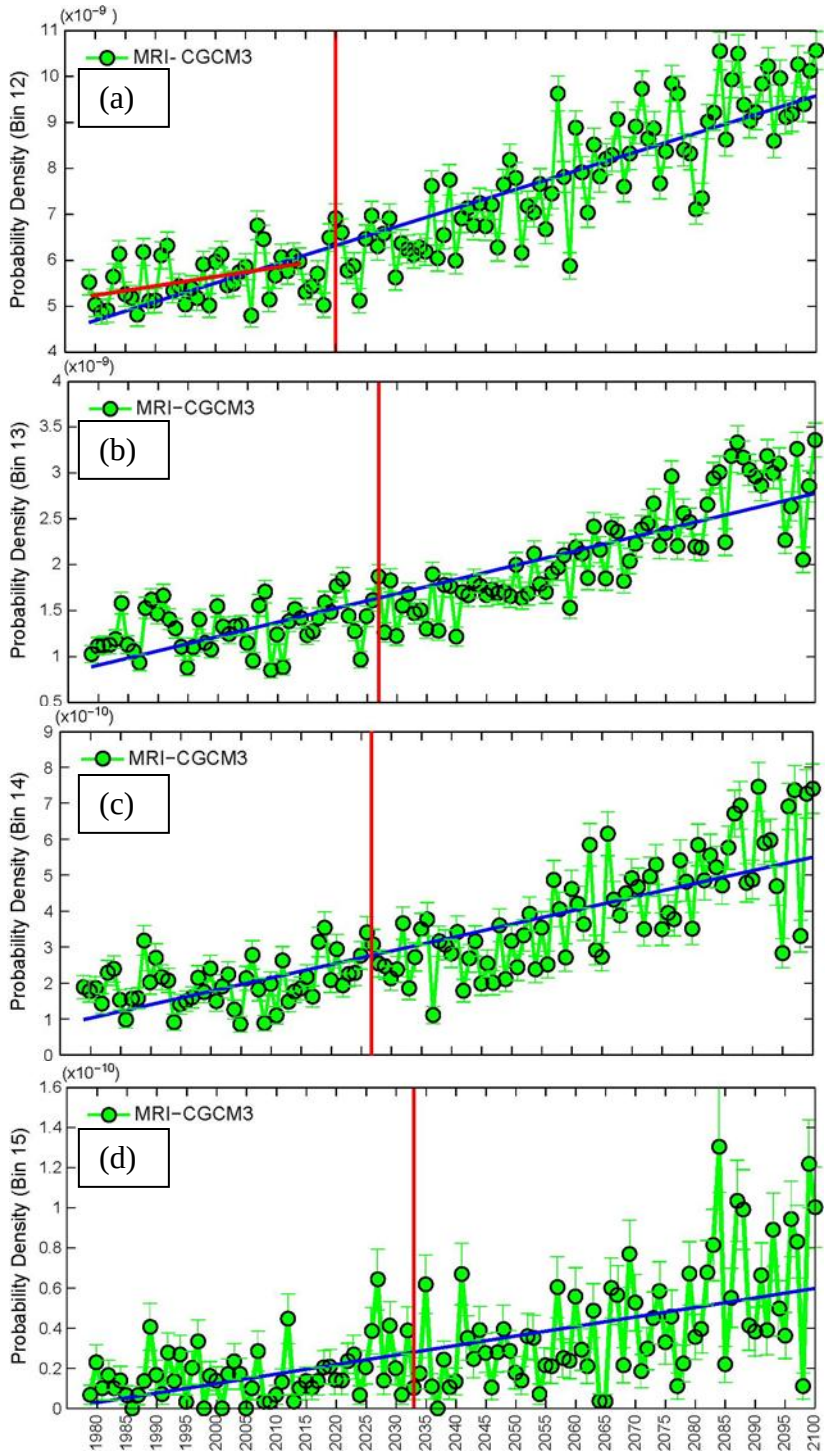

Fig. 3.6: Same as Fig. 3.4, except for MRI-CGCM3 modeled precipitation clusters for 1979-2100. Recent historical trend (if significant) shown in red, and year where trend becomes significant with all remaining years significant depicted as vertical red line. Trend from 1979-2100 shown in blue.

For the EC-EARTH model (Fig. 3.7), a statistically significant upward trend (also using a Student's t-test at the 95% level) emerges between 2004-2018 for bins 11-13, similar to the trends that emerge in bin 10 of the NCEP Reanalysis 2 dataset and bin 12 of the MRI-CGCM3 model. In the highest-power bin shown (bin 14), an upward trend is not significant until 2030. Modeled EC-EARTH storms with their power falling within bins 11-13 become 1.4 to 4 times more frequent by end-of-century, respectively, relative to their historical mean values, and precipitation clusters from the highest-power bin shown (bin 14) become 13 times more frequent. The end-of-century frequency increases for all MRI-CGCM3 and EC-EARTH bins shown in Fig. 3.6 and 3.7 fall above one standard deviation around their historical mean values, implying that the end-of-century increase in the frequency of high-power precipitation clusters is unprecedented compared to recent climate.

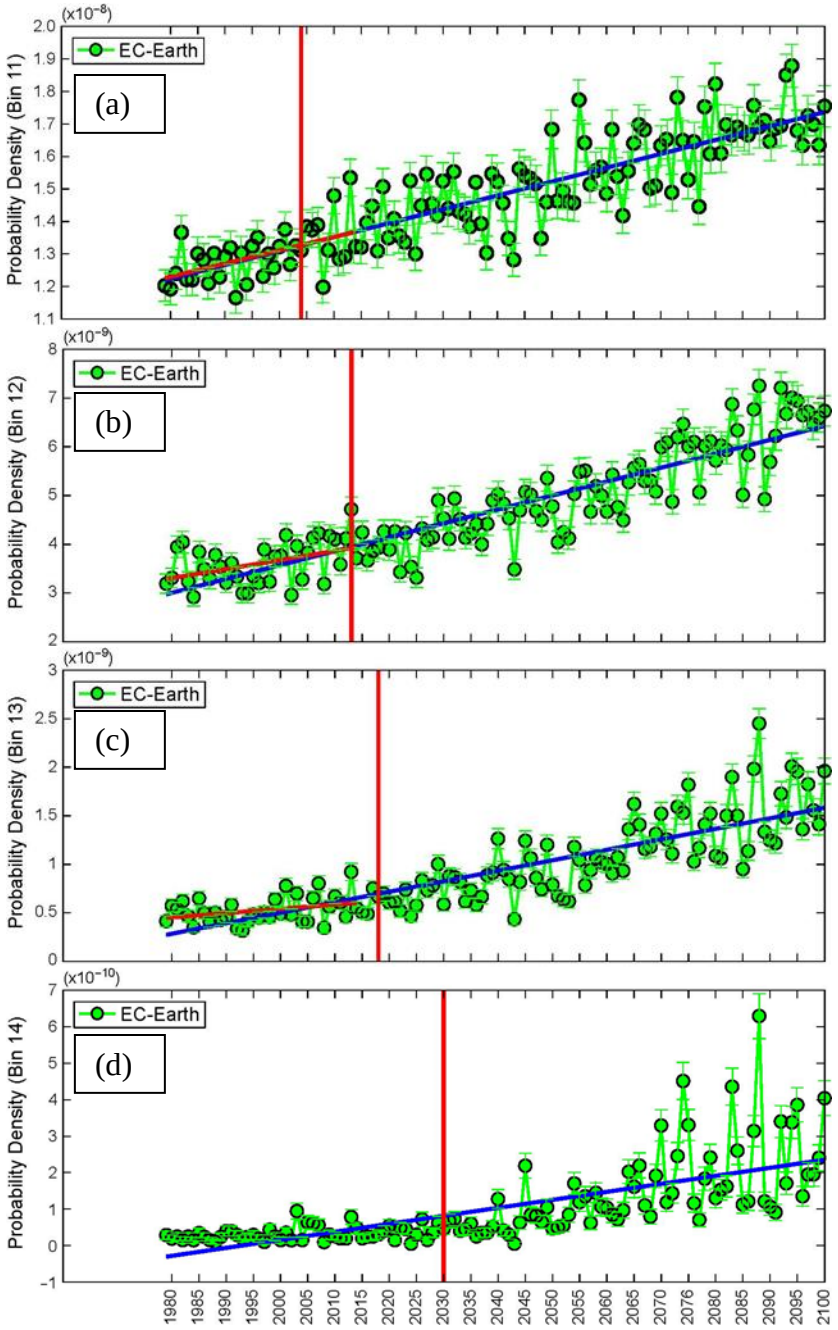

Fig. 3.7: Same as Fig. 3.6, but for EC-EARTH model.

The frequency of the most powerful precipitation clusters from the MIROC5 model (Fig. 3.8) show much greater interannual variability, compared to the EC-EARTH and MRI-CGCM3 output. The upward trends for MIROC5 do not become statistically significant until after 2060, possibly due in part to the large degree of interannual variability. The relative magnitude of the increased probability of powerful storms in the MIROC5 model only ranges from a factor of 1.16 to 1.51, respectively, less than the increases projected in the MRI-CGCM3 and EC-EARTH models. Additionally, only the trends from bins 11 and 12, not bins 13 and 14, fall above one standard deviation, relative to their historical mean.

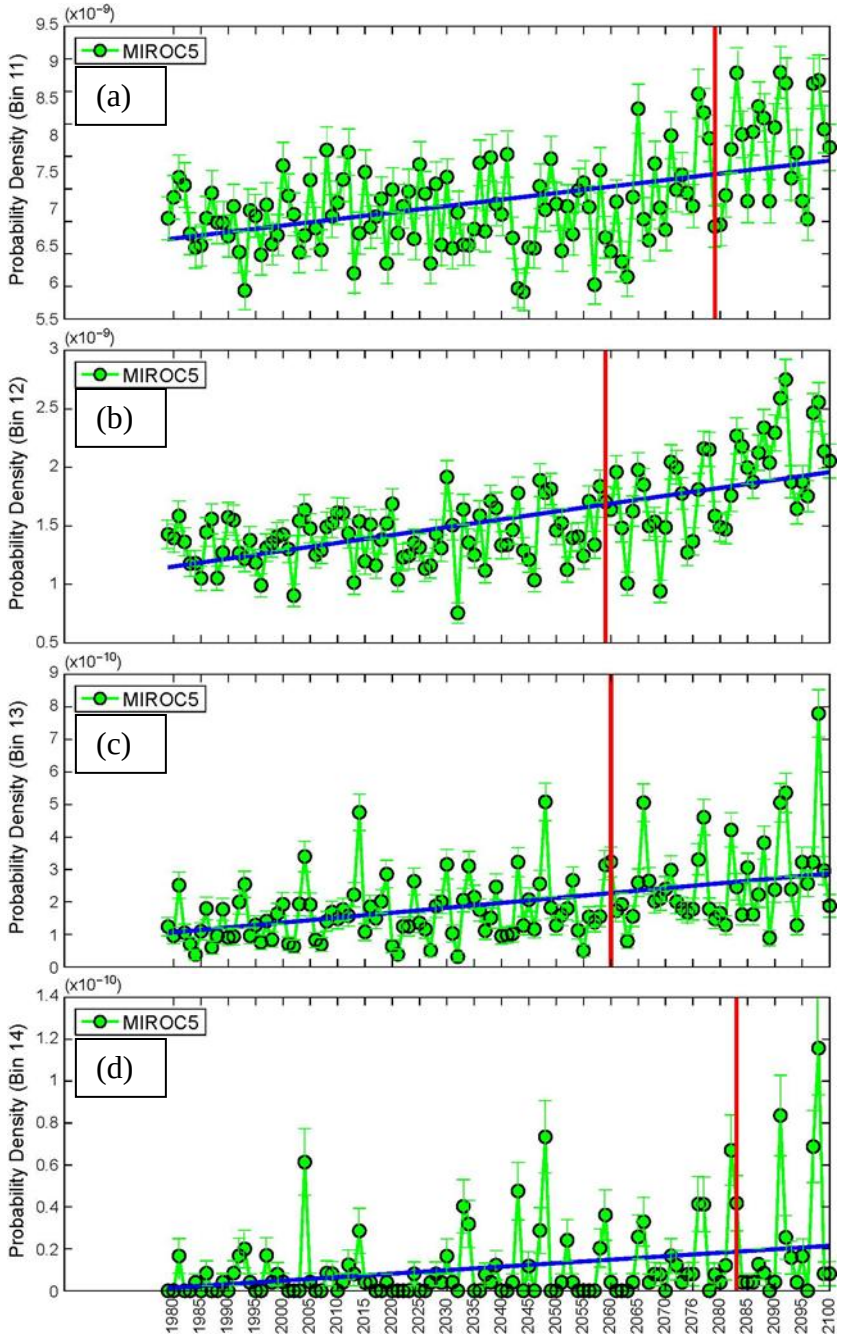

Fig. 3.8: Same as Fig. 3.6, but for MIROC5 model.

3.5 Discussion

Here we examine distributions of storm cluster power over the Tropics using satellite rain rate retrievals (SSM/I-SSMIS and TRMM-3B42) and NCEP Reanalysis 2 precipitation data, with SSM/I-SSMIS and TRMM-3B42 distributions, in general, closely paralleling each other. Specifically, SSM/I-SSMIS cluster power distributions show little variation by rain rate threshold and have the same scale-free power law region and cutoff at high cluster power as TRMM-3B42, indicating that gap width does not affect the cutoff. NCEP Reanalysis 2 cluster power distributions begin at higher power due to coarser resolution and cut off at slightly higher power than observations, but even so, approximate the same form as the observed cluster power distributions.

Since the SSM/I-SSMIS data record extends back to 1987, we also analyze SSM/I-SSMIS rain rate data for changes to storm cluster power behavior in recent climate. SSMIS swaths are approximately 300 km wider than SSM/I swaths, so to test cluster power statistics for sensitivity to swath width, we run a procedure where we narrow SSMIS swaths to match SSM/I swath width at the 0.7 mm hr^{-1} rain rate. The swath width calibration has only a modest impact, as SSM/I and matched-swath-width SSMIS rain rate percentiles are highly calibrated (e.g., the correlation coefficient between retrievals equals 0.9987) and have a least squares best-fit line that is nearly one-to-one. Despite the high degree of calibration, the probabilities of the most intense precipitation clusters from the four highest-power bins broken out into time series by satellite display a discontinuity between SSM/I, SSMIS, and matched-swath-width SSMIS retrievals, such that for the level of difference we are trying to detect here, the current SSM/I-SSMIS calibration is insufficient. Some of the highest-power bins in both the SSM/I-SSMIS and NCEP Reanalysis 2 datasets do show an increase in the probability of the most

powerful precipitation clusters in recent climate, but given the instrumentation, these trends may not be reliable. Improvements to SSM/I-SSMIS rain rate retrieval inter-calibrations and overlapping satellite instrumentation would be useful for detecting trends in cluster power behavior within the next couple of decades. Any gap in satellite coverage, especially with consistent instrumentation potentially hinders such efforts. Given the termination of the DMSP program, canceled launch of the F20 satellite, degradation of data from the F17 satellite and failure of the F19 satellite, data record continuity may be an important consideration.

Cluster power distributions from our ensemble of CMIP5 models begin at higher power than our observed datasets, and thus have shorter scale-free regions. Even so, all of the CMIP5 models reasonably reproduce the scale-free region with approximately the same exponent and cutoff as in observations here and in Chapter 2. By end-of-century, we see a consistent trend towards more frequent high-power precipitation clusters across all models, with the probability of precipitation clusters from the highest-power bin (for which statistics can be computed) increasing by up to an order of magnitude, relative to historical climate, matching HIRAM trends uncovered in Chapter 2.

Given that these models generally agree on end-of-century changes, we investigate the timeframe on which statistically significant increases in the probability of the most intense storms appear in the three models of our ensemble that have a continuous data record through end-of-century. A time series analysis of two of the three models with continuous data (MRI-CGCM3 and EC-EARTH) show a statistically significant increase in the probability of the most intense precipitation clusters in near future, even for these metrics that break down the probability trends as a function of storm size. On the other hand, the third model (MIROC5) does not display a detectable signal until after 2050. Interannual variability is much greater in

the MIROC5, which may affect detectability. Having more high resolution CMIP models with continuous data records extending through end-of-century would help narrow the uncertainty surrounding detectability.

References

Alexander, L. V., and Coauthors, 2006: Global observed changes in daily extremes of temperature and precipitation. *J. Geophys. Res. Atmos.*, **111**, D05109, doi: 10.1029/2005JD006290.

Allan, R. P., and B. J. Soden, 2008: Atmospheric warming and the amplification of precipitation extremes. *Science*, **321**, 1481-1484.

——, B. J. Soden, V. O. John, W. Ingram, and P. Good, 2010: Current changes in tropical precipitation. *Environ. Res. Lett.*, **5**, 1-7, doi:10.1088/1748-9326/5/2/025205.

Bowman, K. P., C. R. Homeyer, and D. G. Stone, 2009: A comparison of oceanic precipitation estimates in the tropics and subtropics. *J. Appl. Meteor. Climatol.*, **48**, 1335-1344, doi: 10.1175/2009JAMC2149.1.

Chen, Y., E. E. Ebert, K. J. E. Walsh, N. E. Davidson, 2013: Evaluation of TRMM 3B42 precipitation estimates of tropical cyclone rainfall using PACRAIN data. *J. Geophys. Res.*, **118**, 2184-2196, doi:10.1002 /jgrd.50250.

Easterling, D. R., G. A. Meehl, C. Parmesan, S. A. Chagnon, T. R. Karl, and L. O. Mearns, 2000: Climate extremes: Observations, modeling, and impacts. *Science*, **289**, 2068-2074, doi: 10.1126/science.289.5487.2068.

Hilburn, K. A., and F. J. Wentz, 2008: Mitigating the impact of RADCAL beacon contamination on F15 SSM/I ocean retrievals. *Geophys. Res. Lett.*, **35**, L18806, doi:10.1029/2008GL034914.

Huffman, G. J., and Coauthors, 2007: The TRMM multisatellite precipitation analysis (TMPA): Quasi-Global, multiyear, combined-sensor precipitation estimates at fine scales. *J. Hydrometeor*, **8**, 38–55, doi:10.1175/JHM560.1.

Huffman, G. J. and D. T. Blovin, 2014: TRMM and other data precipitation data set documentation. Accessed 30 November 2015. [Available online at ftp://meso-a.gsfc.nasa.gov/pub/trmmdocs/3B42_3B43_doc.pdf.]

Kanamitsu, M., W. Ebisuzaki, J. Woollen, S.-K. Yang, J. J. Hnilo, M. Fiorino, and G. L. Potter, 2002: NCEP–DOE AMIP-II Reanalysis (R-2). *Bull. Amer. Meteor. Soc.*, **83**, 1631–1643, doi:10.1175/BAMS-83-11-1631.

Kharin, V. V., F. W. Zwiers, X. Zhang, and G. C. Hegerl, 2007: Changes in temperature and precipitation extremes in the IPCC Ensemble of Global Coupled Model Simulations. *J. Climate*, **20**, 1419–1444, doi:10.1175/JCLI4066.1.

Kharin, V. V., F. W. Zwiers, X. Zhang, and M. F. Wehner, 2013: Changes in temperature and precipitation extremes in the CMIP5 ensemble. *Climatic Change*, **119.2**, 345-357, doi: 10.1007/s10584-013-0705-8.

Lenderink, G., and E. Van Meijgaard, 2008: Increase in hourly precipitation extremes beyond expectations from temperature changes. *Nature Geosci.*, **1(8)**, 511-514.

Mapes, B., R. Milliff, and J. Morzel, 2009: Composite life cycle of maritime tropical mesoscale convective systems in scatterometer and microwave satellite observations. *J. Atmos. Sci.*, **66**, 199–208, doi:10.1175/2008JAS2746.1.

McCollum, J. R., and R. R. Ferraro, 2003: Next generation of NOAA/NESDIS TMI, SSM/I, and AMSR-E microwave land rainfall retrievals. *J. Geophys. Res.*, **108(D8)**, 8382, doi:10.1029/2001JD001512, 2003.

National Snow and Ice Data Center (NSIDC), 2016: Special Sensor Microwave Imager (SSM/I). Accessed 1 February 2016. [Available at https://nsidc.org/data/docs/daac/ssmi_instrument.gd.html]

National Snow and Ice Data Center (NSIDC), 2016: Special Sensor Microwave Imager/Sounder (SSMIS). Accessed 1 February 2016. [Available at https://nsidc.org/data/docs/daac/ssmis_instrument/]

Peters, O., J. D. Neelin, and S. W. Nesbitt, 2009: Mesoscale convective systems and critical clusters. *J. Atmos. Sci*, **66.9**, 2913-2924, doi:10.1175/2008JAS2761.1.

Peters, O., A. DeLuca, A. Corral, J. D. Neelin, and C. E. Holloway, 2010: Universality of rain event size distributions. *Journal of Statistical Mechanics: Theory and Experiment*, **11**, 1-15, doi: 10.1088/1742-5468/2010/11/P11030.

Peters, O., K. Christensen, and J. D. Neelin, 2012: Rainfall and Dragon-Kings. *The European Physical Journal Special Topics*, **205.1**, 147-158, doi:10.1140/epjst/e2012-01567-5.

Sillmann, J., V. V. Kharin, F. W. Zwiers, X. Zhang, and D. Bronaugh, 2013: Climate extremes indices in the CMIP5 multimodel ensemble: Part 2. Future climate projections. *J. Geophys. Res. Atmos.*, **118**, 2473–2493, doi:10.1002/jgrd.50188.

Skok, G., J. Bacmeister, and J. Tribbia, 2013: Analysis of tropical cyclone precipitation using an object-based algorithm. *J. Climate*, **26**, 2563-2579, doi:10.1175/JCLI-D-12-00135.1.

Sun, N., and F. Weng, 2008: Evaluation of Special Sensor Microwave Imager/Sounder (SSMIS) environmental data records. *IEEE Transactions on Geoscience and Remote Sensing*, **46(4)**, 1006-1016, doi:10.1109/TGRS.2008.917368.

Tan, J., C. Jakob, W. B. Rossow, and G. Tselioudis, 2015: Increases in tropical rainfall driven by changes in frequency of organized deep convection. *Nature*, **519**, 451-460, doi:10.1038/nature14339.

Tebaldi C., K. Hayhoe, J. M. Arblaster, and G. A. Meehl, 2006: Going to the extremes: an intercomparison of model-simulated historical and future changes in extreme events. *Climatic Change*, **79**, 185–211, doi:10.1007/s10584-006-9051-4.

Tropical Rainfall Measuring Mission Project (TRMM), 2015: Daily TRMM and Others Rainfall Estimate (3B42 V7 derived), version 7. Goddard Space Flight Center Distributed Active Archive Center (GSFC DAAC). Accessed 01 July 2015. [Available online at http://disc.sci.gsfc.nasa.gov/datacollection/TRMM_3B42_daily_V7.html.]

Wentz, F. J., and R. W. Spencer, 1998: SSM/I rain retrievals within a unified all-weather ocean algorithm. *J. Atmos. Sci.*, **55**, 1613-1627.

Wentz, F. J., K. A. Hilburn, and D. K. Smith, 2012: Remote Sensing Systems DMSP SSM/I and SSMIS Daily Environmental Suite on 0.25 deg grid, Version 7. Remote Sensing Systems, Santa Rosa, CA. Accessed 01 Feb 2016. [Available online at www.remss.com/missions/ssmi.]

Wentz, F. J., 2013: SSM/I Version-7 Calibration Report. Remote Sensing Systems Report Number 011012, 46 pp, URL: http://images.remss.com/papers/rsstech/2012_011012_Wentz_Version-7_SSMI_Calibration.pdf

Wood, R., and P. R. Field, 2011: The distribution of cloud horizontal sizes. *J. Climate*, **24**, 4800-4816, doi:10.1175/2011JCLI4056.1.

Yan, B., and F. Weng, 2008: Intercalibration between special sensor microwave/imager sounder and special sensor microwave imager. *IEEE Transactions on Geoscience and Remote Sensing*, **46(4)**, 984-995, doi:10.1109/TGRS.2008.915752.

4 Precipitation Clusters in Boreal Winter Storm Tracks in Current Climate and Projected Changes Under Global Warming

4.1 Abstract

Probability and spatial distributions of the mass of water released in precipitation clusters (i.e., over contiguous precipitating grid cells) provide potentially useful metrics of changes in the most powerful mid-latitude storms during boreal winter under global warming. Observed probability distributions of cluster power from the Tropical Rainfall Measuring Mission (TRMM-3B42) rain rate product follow a scale-free power law range up to a distinct cutoff at high power, after which probabilities of the most powerful events decrease more rapidly. Simulated historical cluster power distributions from the High Resolution Atmospheric Model, seven 1- 2° resolution members of the Coupled Model Intercomparison Project Phase 5, and ten members of the National Center for Atmospheric Research Large Ensemble qualitatively capture the power law range and cutoff, although the cutoff occurs at lower power compared to observations. End-of-century changes in the frequency of large clusters from the highest-power bin relative to recent climate suggest that the frequency of the most intense storms will increase by factors ranging from 2 to 7. Spatial distributions of observed precipitation-weighted storm centroids with power exceeding 10^{12} kg H_2O hr^{-1} provide a baseline of high-power clusters in recent climate. Spatial distributions of these storm centroids in historical climate simulations agree well with observed spatial distributions. Simulated end-of-century centroid spatial distributions clearly show storm track changes, with an extension of the North Pacific storm track guiding more high-power storms onto the US West Coast in 8 of 9 models, and eastern North America exhibiting high-power storm increases in all nine.

4.2 Introduction

In Chapters 2 and 3 we assess storm cluster behavior over the Tropics during May-September in recent and future climate, using a variety of observational and model datasets. We find that distributions of storm cluster power (i.e. precipitation integrated over contiguous precipitating grid cells meeting a minimum rain rate threshold) are scale-free and follow a power law until a cutoff at high power. Beyond this cutoff, the frequency of the most intense precipitation clusters decreases rapidly. This pattern is consistent across all observed and modeled datasets we analyze. Furthermore, we find that the frequency of the most intense storms is projected to increase by up to an order of magnitude compared to recent climate across a suite of Coupled Model Intercomparison Project Phase 5 (CMIP5) global coupled climate models ($1\text{-}2^0$ resolution) and the High Resolution Atmosphere Model (HIRAM, $0.25\text{-}0.5^0$ resolution). Detectability of these changes in short satellite records of recent climate is uncertain, owing to uncertainties in observations and interannual variability.

In this chapter we address precipitation clusters over the Northern Hemisphere during boreal winter. Certain mid-latitude regions (e.g., California), receive much of their annual precipitation during boreal winter (defined here as January-March) (i.e., Cayan and Roads 1984; Chang et al. 2015), with the majority of the precipitation associated with frontal systems. The organization of the most intense precipitation into mesoscale clusters embedded within frontal systems has been noted in numerous observational studies since the 1960s (i.e., Nagle and Serebreny 1962; Elliot and Hovind 1964,1965; Kreitzberg 1964; Nozumi and Arakawa 1968; Kreitzberg and Brown 1970; Austin and Houze 1972; Hobbs et al. 1980; Houze and Hobbs 1982). These fronts connect to conveyor belts transporting large amounts of water vapor horizontally and vertically, in extreme cases sometimes referred to as atmospheric rivers

(Browning and Pardo 1973; Ralph et al. 2006; Ralph et al. 2011; Dettinger 2011; Dettinger et al. 2011; Stohl et al. 2008; Lavers et al. 2011; Lavers and Villarini 2013; Dacre et al. 2015). Changes to the locations and intensity of these storms can have large impacts. Frontal systems can be tracked by low pressure center positions or water vapor transport (Dacre et al. 2015; Lavers et al. 2016). The definition of precipitation clusters that we use in this study captures a consistent set of precipitation statistics associated with all of the above phenomena, from the mesoscale to synoptic scale, from which we can derive measures of both location and intensity changes.

There are consistent trends in climate change research describing changes in precipitation extremes under global warming. For example, at a global scale, wet areas are projected to get wetter and dry areas are projected to get drier (Meehl et al. 2007; Trenberth 2011; Collins et al. 2013; Maloney et al. 2014; Seager et al. 2014b), with more frequent and more intense extreme precipitation events depicted in numerous CMIP3 and CMIP5 studies (e.g., Tebaldi et al. 2006; Kharin et al. 2007, 2013; Sillman et al. 2013) by the end of the 21st Century. As for storm track and intensity changes under global warming, modeling studies by Hall et al. (1994) and Yin (2005) note poleward shifts in mid-latitude storm tracks, along with increased eddy kinetic energy (Hall et al. 1994) over the North Atlantic and increased baroclinicity and poleward shift in precipitation (Yin 2005).

At a regional scale, Neelin et al. (2013) describe the relationship between precipitation changes for California under global warming using output from 15 CMIP5 models, suggesting that an extension of the subtropical jet correlate with projected changes to the North Pacific storm track and California precipitation. Previous modeling studies (i.e., Held et al. 1989; Chen and Van den Dool 1997; Straus and Shukla 1997) also describe the relationship between the jet

stream, El Nino and the frequency over which storms are directed towards the California coast. Chang et al (2015) also finds that this relationship between the extension of the subtropical jet and West Coast precipitation holds true in interannual variability and under global warming, using band-passed-filtered sea level pressure variance of low pressure centers in observations and climate model simulations.

Here, the baseline behavior of Northern Hemisphere winter precipitation clusters is evaluated in observations and models, focusing especially on statistics of the most intense clusters and projections of how these change under global warming. We first build an observational climatology of precipitation cluster statistics using probability distributions from the Tropical Rainfall Measuring Mission (TRMM) 3B42 dataset. Since low pressure centers tend to be offset from precipitation maxima by hundreds of kilometers (Dacre et al. 2015), we also introduce a new metric, the centroid density, which maps the spatial distribution of the most intense winter precipitation clusters in recent climate. We then compare precipitation output from the HIRAM and the same suite of high resolution coupled CMIP5 models analyzed in Chapter 3, initially comparing how well the models capture observed cluster power statistics in recent climate. Next, we contrast probability distributions of cluster power in recent and end-of-century climate under the "business as usual"/Representative Concentration Pathway 8.5 (RCP 8.5) climate change scenario, analyzing for changes in the frequency and intensity of the most intense precipitation clusters under global warming. We also conduct a similar analysis of cluster power statistics in recent and future climate using model output from the National Center for Atmospheric Research Large Ensemble Community Project (NCAR LENS), reviewing probability distributions of cluster power from 10 simulations of the ensemble in an attempt to define the uncertainty on model variability and end-of-century

changes. Lastly, we examine maps of centroid density for the most powerful storms to see how the spatial distribution of the most intense winter precipitation clusters, and consequently storm tracks, change under global warming.

4.3 Data and Methods

As in Chapter 2, data from the Tropical Rainfall Measuring Mission (TRMM-3B42) form an observational baseline for comparison with numerical simulations of precipitation in recent and future climate. Rain rate data from the TRMM-3B42 dataset provide complete spatial coverage over land and ocean from 50^0S-50^0N on a 0.25^0 latitude-longitude grid at 3-hourly intervals in mm hr^{-1} in this study (Huffmann et al. 2007; Huffmann and Blovin 2014; TRMM 2015). As in Chapters 2 and 3, only data from 00/12 UTC January-March 1998-2008 greater than the 0.7 mm hr^{-1} rain rate threshold are incorporated into this study.

Modeling center or group (institute ID)	**CMIP5 model**	**Resolution (Lat x Lon)**	**Data Availability**
National Center for Atmospheric Research (NCAR)	CCSM4	1.0 x 1.25	1979-2005, 2081-2100
Centre National de Recherches Meteorologiques (CNRM)	CNRM-CM5	1.4 x 1.4	1979-2005, 2081-2100
EC-EARTH consortium (EC-EARTH)	EC-EARTH	1.12 x 1.125	1979-2005, 2075-2100
Met Office Hadley Centre (MOHC)	HadGEM2-ES	1.25 x 1.875	1979-2005, 2081-2099
Institute for Numerical Mathematics (INM)	INM-CM4	1.5 x 2.0	1979-2005, 2081-2100
Atmosphere and Ocean Research Institute (The University of Tokyo), National Institute for Environmental Studies, and Japan Agency for Marine-Earth Science and Technology (MIROC)	MIROC5	1.4 x 1.4	1979-2005, 2075-2100
Meteorological Research Institute (MRI)	MRI-CGCM3	1.1 x 1.1	1979-2005, 2075-2100

Table 4.1: CMIP5 modeling centers and models used, with specified spatial resolution and data availability.

Output from the High Resolution Atmosphere Model (HIRAM) (Zhao et al. 2009, 2010, 2011, 2012; Chen and Lin 2011; Held and Zhao 2011; Merlis et al. 2013; Villarini et al. 2014)

at 0.25^0 resolution (1998-2008 and 2086-2095) and the same suite of nominal $1\text{-}2^0$ resolution Coupled Model Intercomparison Project Phase 5 (CMIP5) models from Chapter 3 are compared with observed data to assess their skill in capturing cluster power behavior in current climate, then analyzed for changes under global warming under the Representative Concentration Pathway (RCP) 8.5 scenario. Model precipitation data are available at 3-hourly intervals, though like TRMM-3B42, only samples from 00/12 UTC are used here. See Table 4.1 for more model details.

To evaluate sensitivity of the sampling to natural variability and estimate the associated spread of end-of-century changes in cluster power and centroid density behavior, we also use precipitation data from the National Center for Atmospheric Research Large Ensemble Community Project (NCAR LENS). This ensemble uses the Community Earth System Model version 1 (CESM1), with version 5.2 of the Community Atmosphere Model (CAM5.2) as its atmospheric component (Kay et al. 2015). Precipitation data are available as 6-hourly averages at approximately 1^0 latitude-longitude resolution (Kay et al. 2015). We incorporate data from 10 ensemble members from 1990-2005 and 2071-2080 to simulate recent and future climate under the RCP 8.5 global warming scenario.

Cluster power here is also calculated using a contiguous precipitating pixel approach noted in Chapter 2 and Peters et al. (2012), with grid cells not meeting a minimum rain rate threshold of 0.7 mm hr^{-1} masked. Unlike Chapters 2 and 3, instead of converting to units of instantaneous latent heat release per grid cell, we display cluster power in units of the mass of water lost per hour integrated over a cluster (kg H_2O hr^{-1}). From Chapter 2, 1 GW is equivalent to 1.4×10^6 kg H_2O hr^{-1}, so we continue to refer to this as cluster power. We use these units

here because the integrated rate of water loss from precipitation can more useful for visualizing associated impacts along the West Coast, such as flooding and landslides.

Distributions of cluster power probability are first compared across observed and model datasets to establish a baseline of winter-time cluster power statistics and quantify changes in the frequency of the most powerful precipitation clusters under the RCP 8.5 global warming scenario. As noted previously, we need to ensure there are sufficient counts in the uppermost bins for statistical analysis. As in Chapter 3, our binning procedure in building probability distributions is as follows. Bins are chosen with a nominal width that is constant in log space, so that the bin width increases smoothly as probabilities drop. The increments of cluster size are quantized to multiples of the minimum cluster size, so to ensure that the bin spacing is consistent with this, bin widths are adjusted to the integer multiple of the minimum cluster size that is closest to the nominal bin width. In practice this affects only the lower bins. After an initial binning with nominal log bin width of 0.2, the number of clusters in the highest-power non-zero bin in the historical period is examined. If the number of clusters in the highest-power non-zero bin in the historical period is less than a user defined threshold (25 in this study), we re-define the highest-power non-zero bin around the 25 highest-power samples resulting from ranking the historical distribution. We then slightly adjust the nominal bin width of the highest-power non-zero bin, which is sufficient to increase cluster counts in the highest bin. We then apply this new bin width to the 4 high-power bins preceding the highest-power non-zero bin in future simulations of the same dataset, and also to new higher power bins that may emerge by end-of-century. We verify that results prior to re-binning are consistent with results after application of the binning adjustment procedure, which helps ensure statistical significance in comparing the highest-power bins in recent and future climate.

Lastly, precipitation-weighted storm centroids are computed for the most powerful precipitation clusters (defined as clusters with power greater than 10^{12} kg H_2O lost hr^{-1}). These centroids condense storm intensity and geographic location into one variable while ensuring that insignificant clusters do not interfere with our analysis, thus we analyze the spatial distribution of precipitation-weighted centroids as a metric for assessing storm track changes in recent and future climate. We define centroid density as the average annual number of precipitation-weighted centroids within 10^0 longitude and 5^0 latitude of each grid cell for each period analyzed. This spatial footprint is chosen to yield reasonably good statistics in terms of the number of centroids per year occurring in the footprint area, while still providing sufficiently detailed spatial information for meteorological and applications interpretation. Seasonal maps of centroid density are used to illustrate the spatial pattern of the winter storm tracks for the Northern Hemisphere in recent climate and their changes under global warming. These maps are constructed using the following procedure: first, maps plotting all the precipitation-weighted centroids for each year are built. Next, the number of centroids within 10^0 longitude and 5^0 latitude of each grid cell are counted for each year. Seasonal mean centroid density is thus the mean of the annual winter centroid density value for each grid cell for the historical and end-of-century periods.

4.4 Analysis

To account for spatial impacts of changes in cluster power, Figure 4.1 shows observed probability and spatial distributions (TRMM-3B42) of cluster power and high-power precipitation-weighted centroids above a minimum power threshold (10^{12} kg H_2O hr^{-1}) for the North Pacific, North American West Coast, eastern North America, and North Atlantic for

January-March 1998-2008. These regions (Table 4.2) are chosen for impacts and the relatively high number of precipitation-weighted centroids that occur in the region. It is important to note, however, that precipitation associated with these high-power centroids may extend outside these domains. Each region contains at least some ocean grid cells, as storms occur proximal to the coasts. The use of precipitation-weighted centroids is an observable metric oriented towards the atmospheric dynamics of precipitation that indicates where largest impacts associated with spatial changes to the storm track may occur, although it will not be a perfect match to specific land region considerations such as watershed boundaries. Mid-latitude cluster power distributions (Fig. 4.1a) reproduce a similar power law form as summertime tropical cluster power distributions noted in Chapters 2 and 3. In both seasons, least squares best fit exponents (extending to the cutoff at high cluster power) are similar to each other, ranging from -1.5 during summer to -1.48 during winter. Cluster power distributions during winter over mid-latitudes have a cutoff value approximately equal to 10^{13} kg H_2O hr^{-1}.

Domain	**Latitude ***	**Longitude**
North Pacific	32N-55N	140E-127W
North American West Coast	32N-55N	127W-120W
Eastern North America	30N-50N	90W-65W
North Atlantic	30N-55N	65W-10W
*TRMM-3B42 domains only extend to 50N		

Table 4.2: Boundaries for each domain analyzed in this study.

Figure 4.1b displays the seasonal mean observed centroid density of the most intense precipitation clusters over the Northern Hemisphere. Figure 4.1b suggests that most of the precipitation clusters meeting our minimum rain rate and cluster power thresholds (0.7 mm hr^{-1} and 10^{12} kg H_2O hr^{-1}) are concentrated over the northwest Pacific and northwest Atlantic, with secondary maxima over the West Coast of North America and eastern North America. Recall

that in our analysis here, precipitation-weighted clusters with power below 10^{12} kg H_2O hr^{-1} are masked. An analysis of the spatial distribution of precipitation-weighted centroids with power meeting a lower threshold (10^{10} kg H_2O hr^{-1}) shows a very similar pattern as the centroid density map shown in Fig. 4.1b, so is not displayed here.

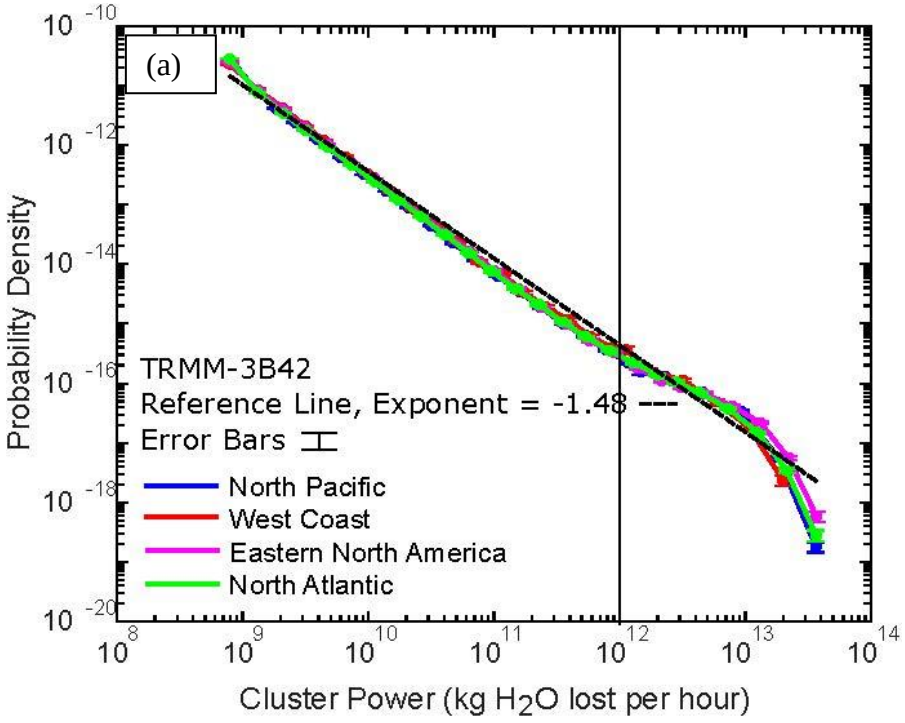

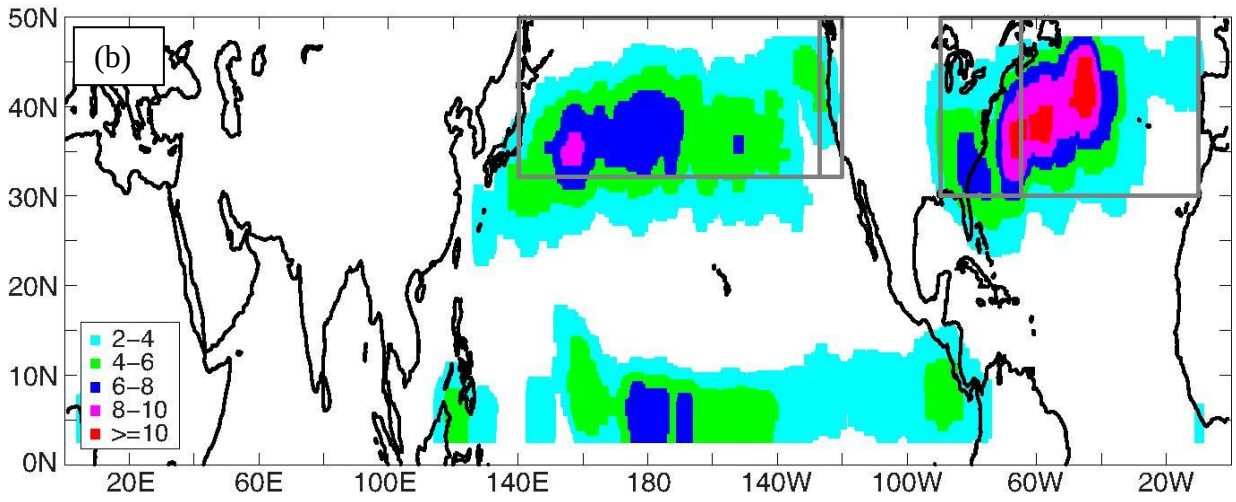

Fig. 4.1: (a) Probability distributions of cluster power, i.e., precipitation integrated over clusters of contiguous pixels exceeding a minimum rain rate threshold (0.7 mm hr^{-1}), expressed in units of mass of water lost per hour per cluster (kg H_2O hr^{-1}). (b) Spatial distributions of mean annual centroid density, i.e. the number of clusters meeting the specified rain rate and cluster power (10^{12} kg hr^{-1}) thresholds within 10^0 longitude and 5^0 latitude of each grid cell. Cluster power and centroid density are calculated from the TRMM-3B42 precipitation product, over the Northern Hemisphere, January-March 1998-2008.

Figure 4.2 shows simulated distributions of cluster power for each model in current and future climate for 4 regions of large impact, highlighting changes to the frequency of intense precipitation clusters under global warming, and the spread in projected changes between models and regions. Simulated cluster power distributions in Fig. 4.2 suggest that the suite of 9 models included in this study qualitatively reproduce the scale-free power law range found in observational cluster power distributions, with a sharp decrease in the frequency of the most intense precipitation clusters after a cutoff. However, the cutoff for most models lies between 2 and 3 x 10^{12} kg H_2O hr^{-1}, lower than the 10^{13} kg H_2O hr^{-1} cutoff value seen in observations. Also, as in Chapter 3, model probability distributions of cluster power begin at higher power with fewer bins than observations, owing to the finer resolution of observations.

Changes to the frequency of the most intense storms may appear small due to log-scaling of the axes in Fig. 4.2, but at high power, a clear signal indicating more frequent

intense storms by end-of-century emerges across all models and all regions, including unprecedented events beyond the historical highest-power bin. However, the magnitude of this frequency change does exhibit some variation among models. For the North Pacific, end-of-century projected changes in the probability of clusters from the highest-power bin in the historical period range from a factor of 2.2 in the MRI-CGCM3 to 7.4 in the EC-EARTH. Over the West Coast, probability changes from clusters with power in the highest-power historical bin range from a decrease by 24% in the MIROC5 to an increase by a factor of 6.5 in the HadGEM2-ES. Probability increases in the same bin over eastern North America are between factors of 1.65 (HIRAM) to 5.5 (MRI-CGCM3), and over the North Atlantic, between factors of 2.3 (HIRAM) and 6.5 (EC-EARTH). In general, the strongest end-of-century probability increases in the most powerful precipitation clusters emerge in output from the EC-EARTH and HadGEM2-ES models, while end-of-century projections in ensemble mean of the 10 members of the NCAR LENS model included here range between factors of 4 (eastern North America) to 5.3 (North Pacific).

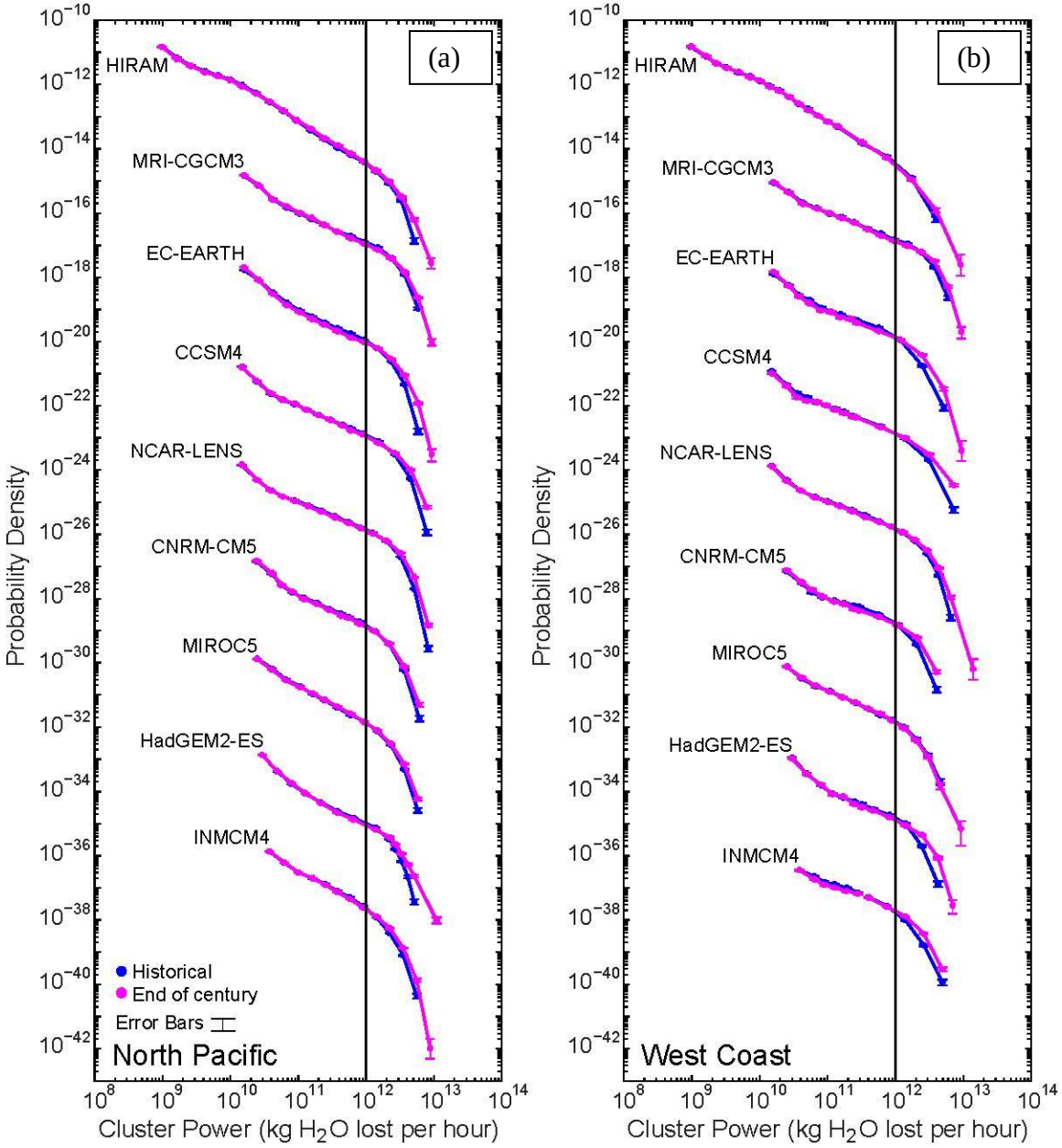
(a)
HIRAM
MRI-CGCM3
EC-EARTH
CCSM4
NCAR-LENS
CNRM-CM5
MIROC5
HadGEM2-ES
INMCM4
Historical
End of century
Error Bars
North Pacific
Probability Density
Cluster Power (kg H2O lost per hour)
(b)
West Coast

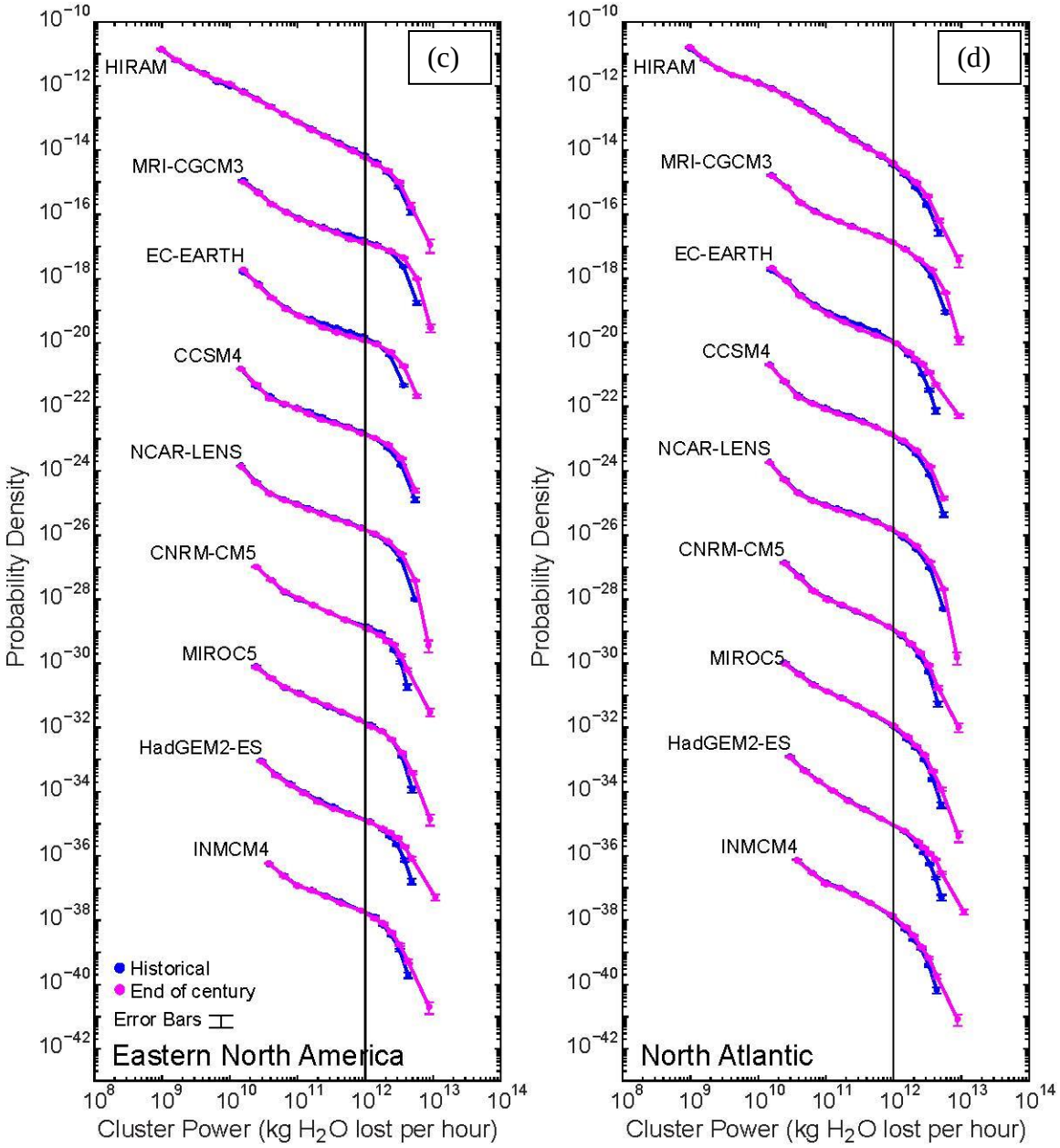

Fig. 4.2: As in Fig. 4.1a, broken out by region of interest with distributions from each model in the suite of models analyzed here. Simulations of cluster power in present climate are in blue while future simulations are in magenta. Historical period: 1979-2005, except HIRAM (1998-2008) and NCAR LENS (1990-2005). End-of-century RCP 8.5 period: 2071-2080 (NCAR LENS), HIRAM (2086-2095), 2081-2100 (CNRM-CM5, CCSM4, HadGEM2-ES, INMCM4), 2075-2100 (MRI-CGCM3, EC-EARTH, MIROC5).

Figure 4.3 explores a range of changes using the NCAR LENS dataset, checking for agreement between 10 ensemble simulations of recent and future climate. Distributions of cluster power from each ensemble member of the NCAR LENS dataset incorporated here

reproduce the end-of-century changes noted in Fig. 4.2. When each run is considered separately, there appears to be little spread between each historical and future simulation, suggesting limited climate system internal variability.

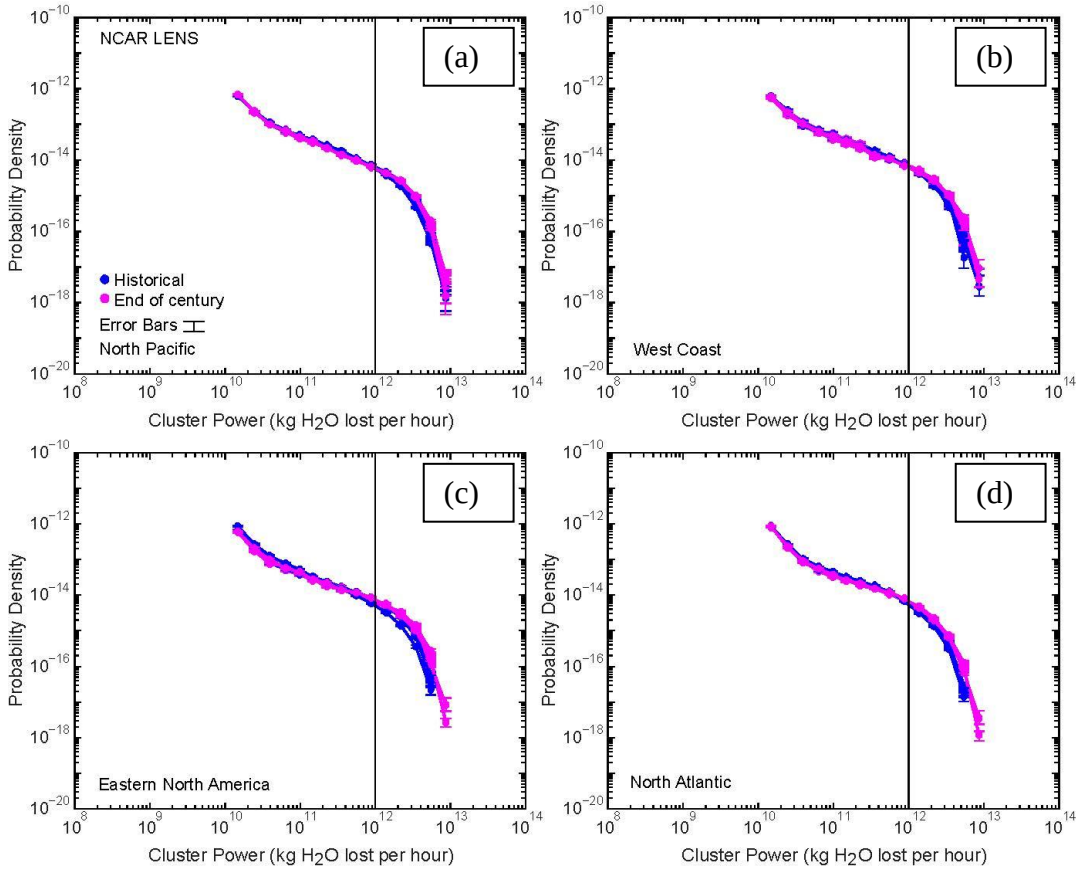

Fig. 4.3: As in Fig. 4.2, but for each simulation of the NCAR LENS dataset included in this study.

Figures 4.4-4.12 present maps of centroid density for each model member of this 9 model suite in recent climate (a), future climate (b), and the change in seasonal mean centroid density (c) by end-of-century relative to recent climate. The locations of centroid density maxima from the HIRAM in recent climate (Fig. 4.4a) appear to match with the locations of centroid density maxima in observations (Fig. 4.1b), implying that the HIRAM reasonably simulates the location of mid-latitude winter storm tracks over the Northern Hemisphere. The HIRAM does show fewer storms over the North Atlantic, more over the North Pacific, and

more along the equatorial West Pacific, however, than observations. End-of-century centroid density changes (Fig. 4.4a,b) tend to increase in the poleward parts of the storm track, and exhibit decreases in certain locations on the subtropical side. Over eastern North America and North Atlantic the poleward increases are quite consistent, with a slight north-eastward extension of the storm track in the Atlantic. Over the North Pacific, centroid density increases on the poleward side of the storm track in the central Pacific. On the subtropical edge of the storm track decreases may be noted on the western side of the basin, although increases occur north of Hawaii, while centroid density decreases over California and Oregon and the neighboring ocean. However, the North American West Coast poleward of Washington State, including British Columbia, exhibits centroid density increases. The slight increase over Canada and mixed changes over ocean may explain the slight end-of-century increase shown in Fig. 4.2, even though a negative signal appears to the south. Because the HIRAM differs over the US West Coast for the models discussed below, it is worth underlining that it has a shorter available time series: only 10 years for the end-of- century simulation.

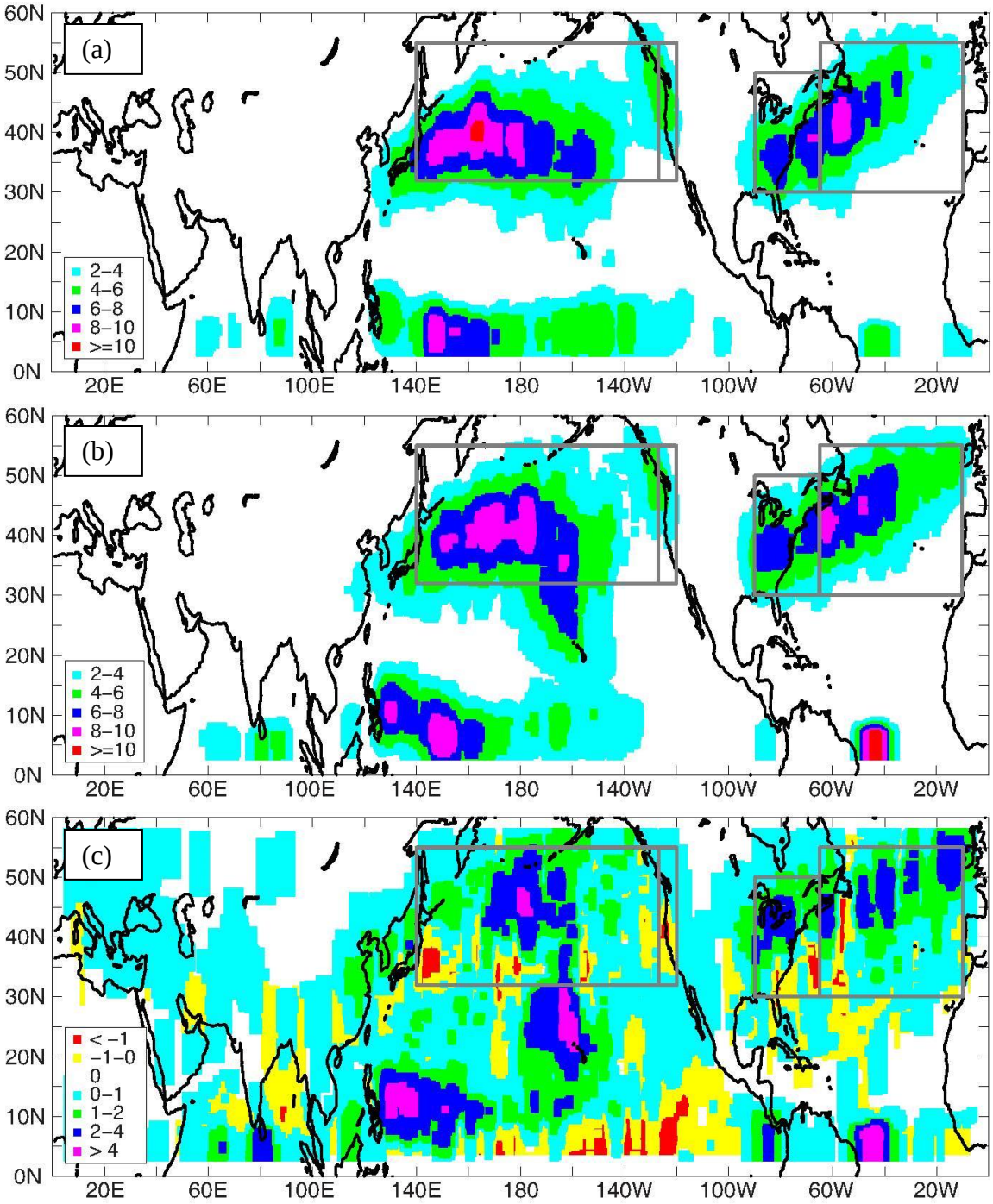

Fig. 4.4: As in Fig. 4.1b, but for HIRAM historical (a) and end-of-century (b) simulations. (c) Centroid density differences, i.e. the projected end-of-century change in mean centroid density for each grid cell, calculated by subtracting the mean centroid density for the historical period from the mean centroid density for the end-of-century period.

Storm track changes in the CCSM4 model (Fig. 4.5b,c) are more pronounced than in the HIRAM. The CCSM4 generally matches the location of storm tracks in observations (Fig.

4.1b) and the HIRAM (Fig. 4.4a). At end-of-century (Fig. 4.5b,c), a consistent increase in the centroid density of high-power storms may again be seen along the poleward side of the climatological storm tracks. Decreases on the subtropical margin of the storm tracks may also be seen, although they are less strong in the Atlantic, and in the Pacific tend to be more confined to the western part of the basin. Of particular note is the clear *eastward* extension of the North Pacific storm track over the eastern Pacific and onto US West Coast (unlike the HIRAM), with the frequency of the most intense clusters increasing by up to a factor of 6 (Fig. 4.2). The area of high centroid density over eastern North America and western Atlantic elongates compared to recent climate in addition to exhibiting substantial increases. Tropical decreases and increases may also be seen, although these tend to be less consistent among the models and are not the focus here.

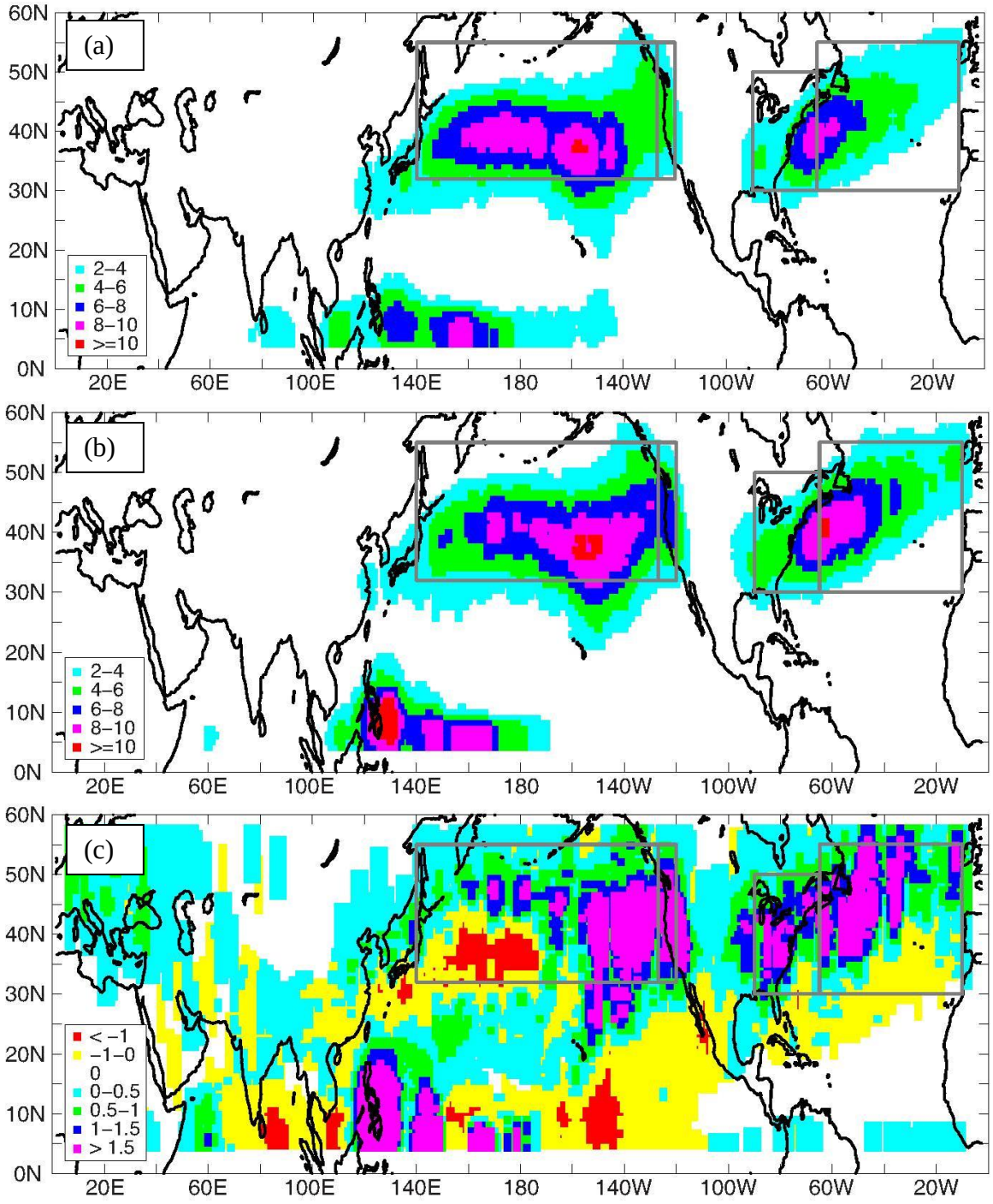

Fig. 4.5: As in Fig. 4.4, but for CCSM4 model.

Storm tracks and their changes under global warming in the CNRM-CM5 model (Fig. 4.6) generally mimic those found in the CCSM4, with a strong signal towards more high-power precipitation clusters hitting the West Coast by end-of-century. Changes over eastern North America and North Atlantic are less strong than in CCSM4, and the western Pacific tends to exhibit a larger region of decrease.

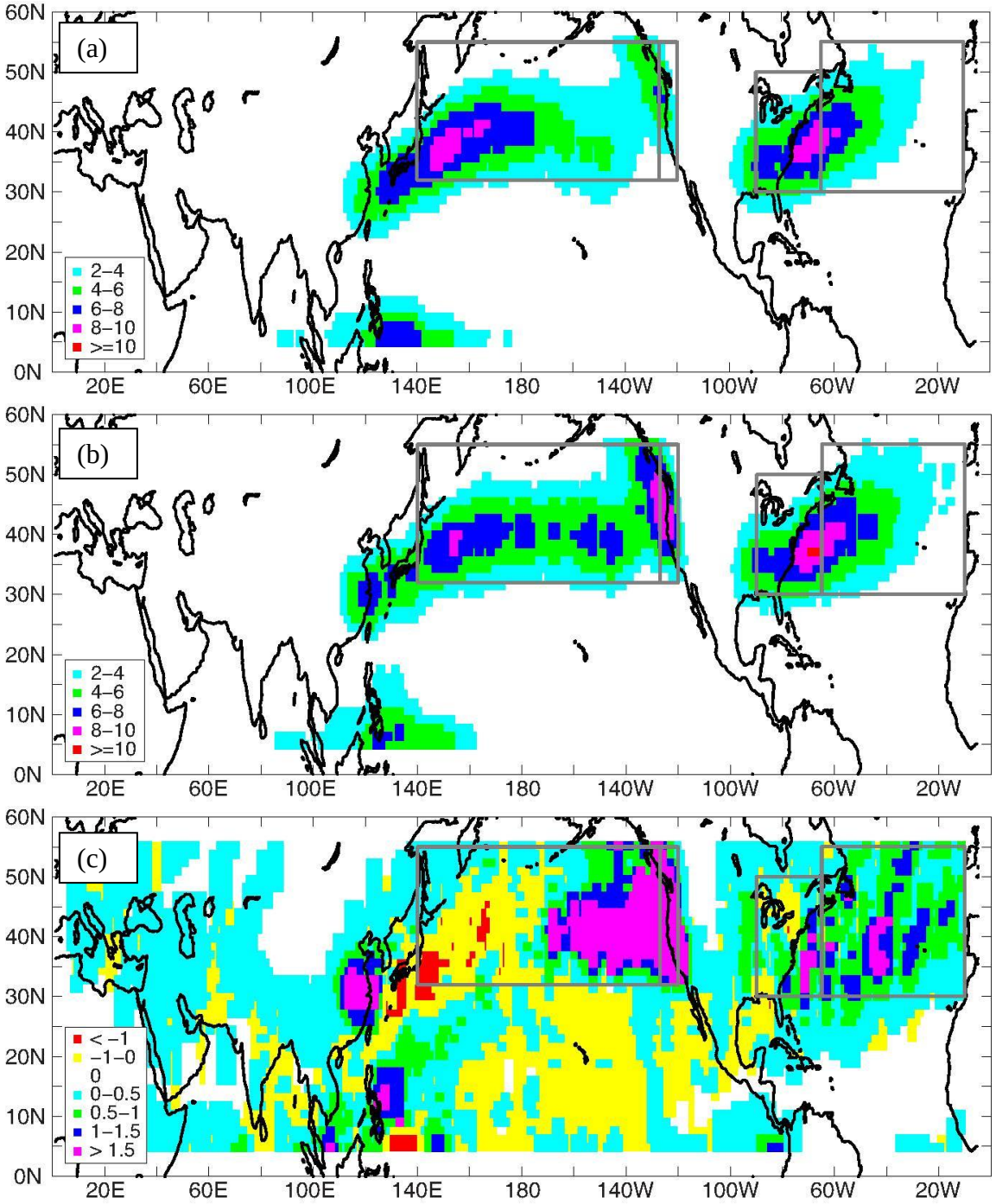

Fig. 4.6: As in Fig. 4.4, but for CNRM-CM5 model.

Historical storm tracks in the EC-EARTH model mirror modeled historical storm tracks in the HIRAM, CCSM4, and CNRM-CM5 models (Fig. 4.7a). Over the North Pacific, eastern North America, and North Atlantic, increases in the probability of high-power centroids by end-of-century are very pronounced (up to a factor of 7.4 over the North Pacific and 6.5 over the North Atlantic, Fig. 4.2), while areas of decreased high-power centroid coverage are confined to smaller areas near Hawaii, eastern Pacific, and central Atlantic. The projected sign of change over the US West Coast is positive (i.e., probabilities of the most intense clusters increase by up to a factor of 3.8, Fig. 4.2), with a small maxima over California, and much larger area of increase along the Pacific Northwest coast and offshore.

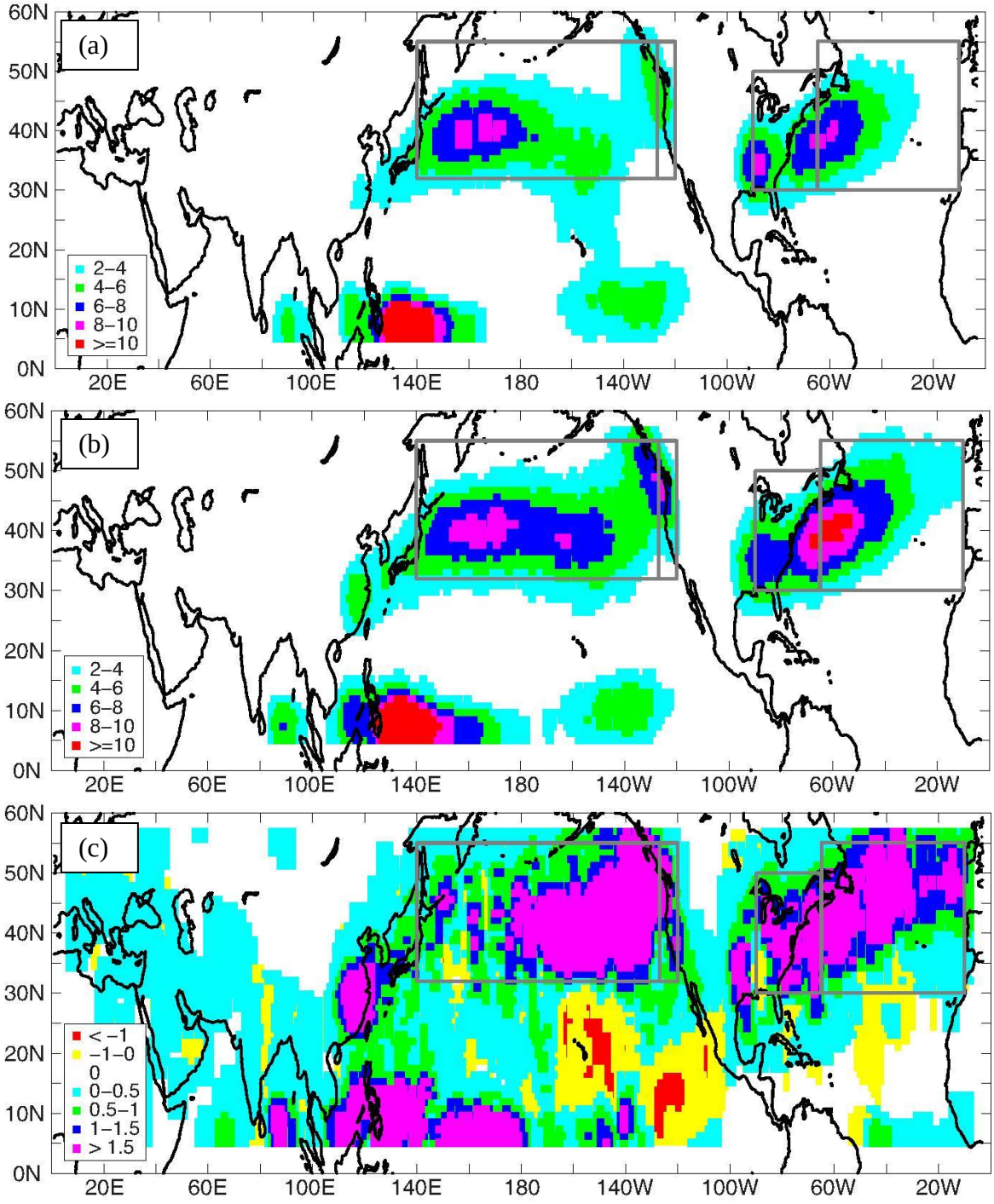

Fig. 4.7: As in Fig. 4.4, but for EC-EARTH model.

Historical storm tracks in the HadGEM2-ES model (Fig. 4.8a) generally match observations and the other models. By end-of-century, a large dipole appears over the northern Pacific (Fig. 4.8b,c). Decreases occur in the western Pacific subtropical margin of the storm track between Hawaii and northeastern Asia. Increases in centroid density occur along the poleward portion of the storm track (i.e., probability increases of the strongest storms by up to a factor of 6.4, Fig. 4.2), and large increases associated with an eastward extension over the eastern Pacific and US West Coast (up to a factor of 6.5, Fig. 4.2). Changes in the probability of intense storms over eastern North America are confined to the eastern half of the region, and are more pronounced (as in the EC-EARTH model, Fig. 4.7c) over the North Atlantic, especially around Newfoundland.

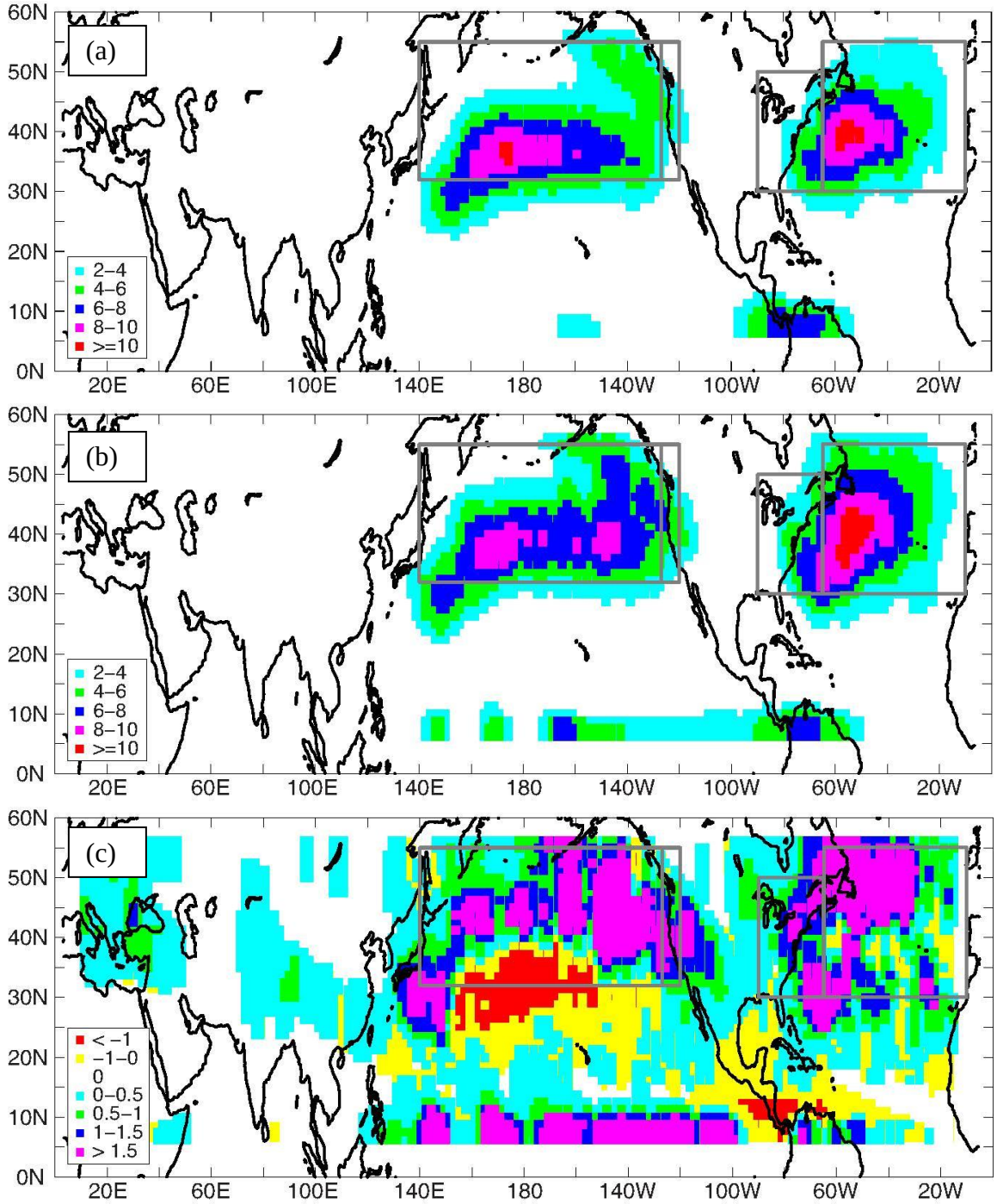

Fig. 4.8: As in Fig. 4.4, but for HadGEM2-ES model.

While historical mid-latitude storm tracks in the INMCM4 (Fig. 4.9a) generally align with the set of observed and modeled storm tracks analyzed in Fig. 4.3-4.8, end-of-century changes over eastern North America and the Atlantic are much less pronounced. An increase in centroid density over the American Great Plains does not appear in any other model here. The immediate area over Japan and east of Japan exhibit decreases in intense storms, while the northeastern Pacific, British Columbia, and Pacific Northwest are projected to see more frequent intense storms (i.e., probabilities of the strongest storms increase between a factor of 2.5 to 3).

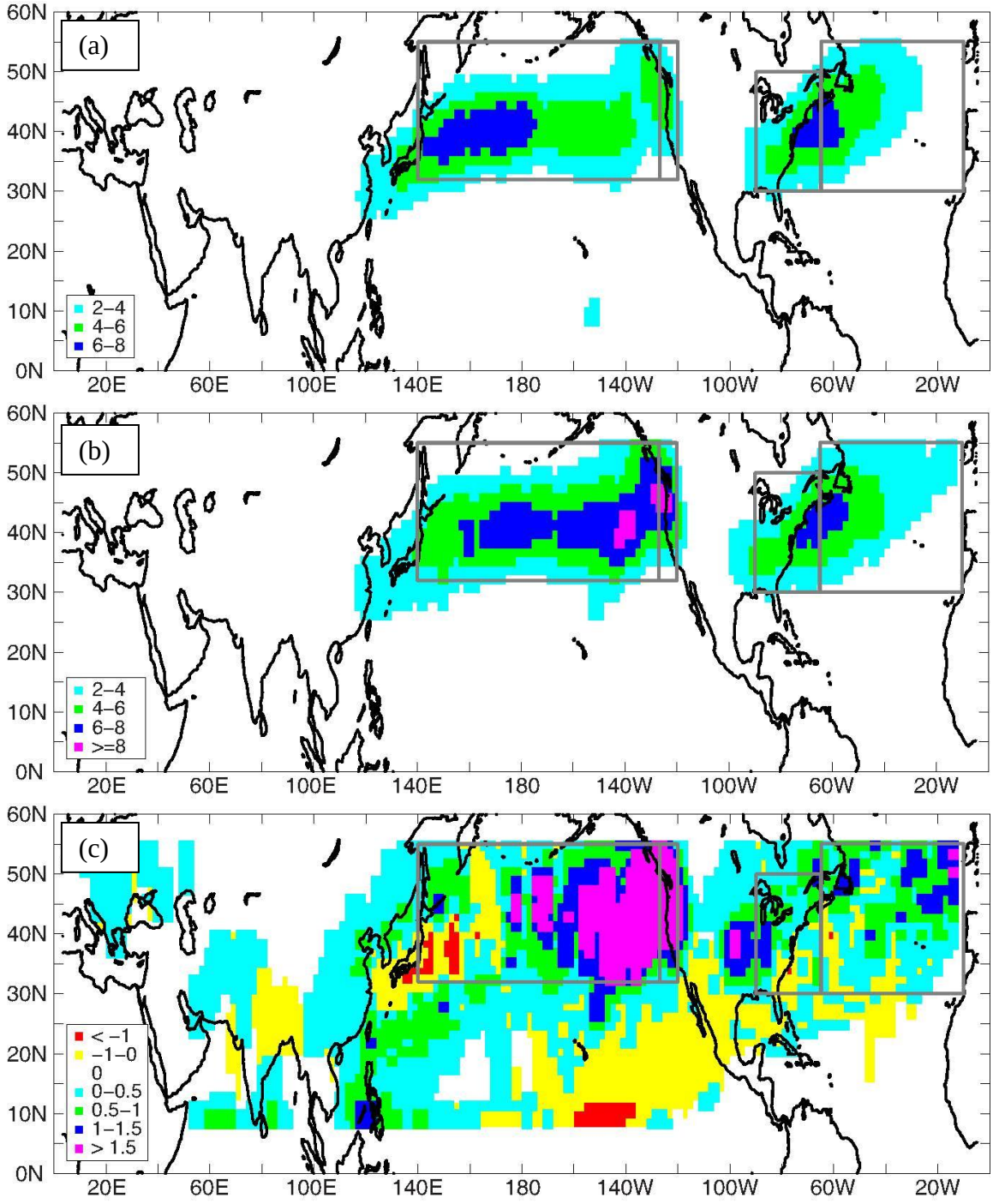

Fig. 4.9: As in Fig. 4.4, but for INMCM4 model.

As with the other models incorporated in this study, the MIROC5 (Fig. 4.10a) qualitatively captures the spatial patterns of centroid density noted previously. Little to no change is seen over eastern North America, while over the West Coast, this measure of storm frequency is projected to decrease by end-of-century over the Pacific Northwest, but increase over British Columbia (Fig. 4.10b,c). Additionally, there is a sharp decrease in centroid density over the eastern Pacific and increase over the western Pacific.

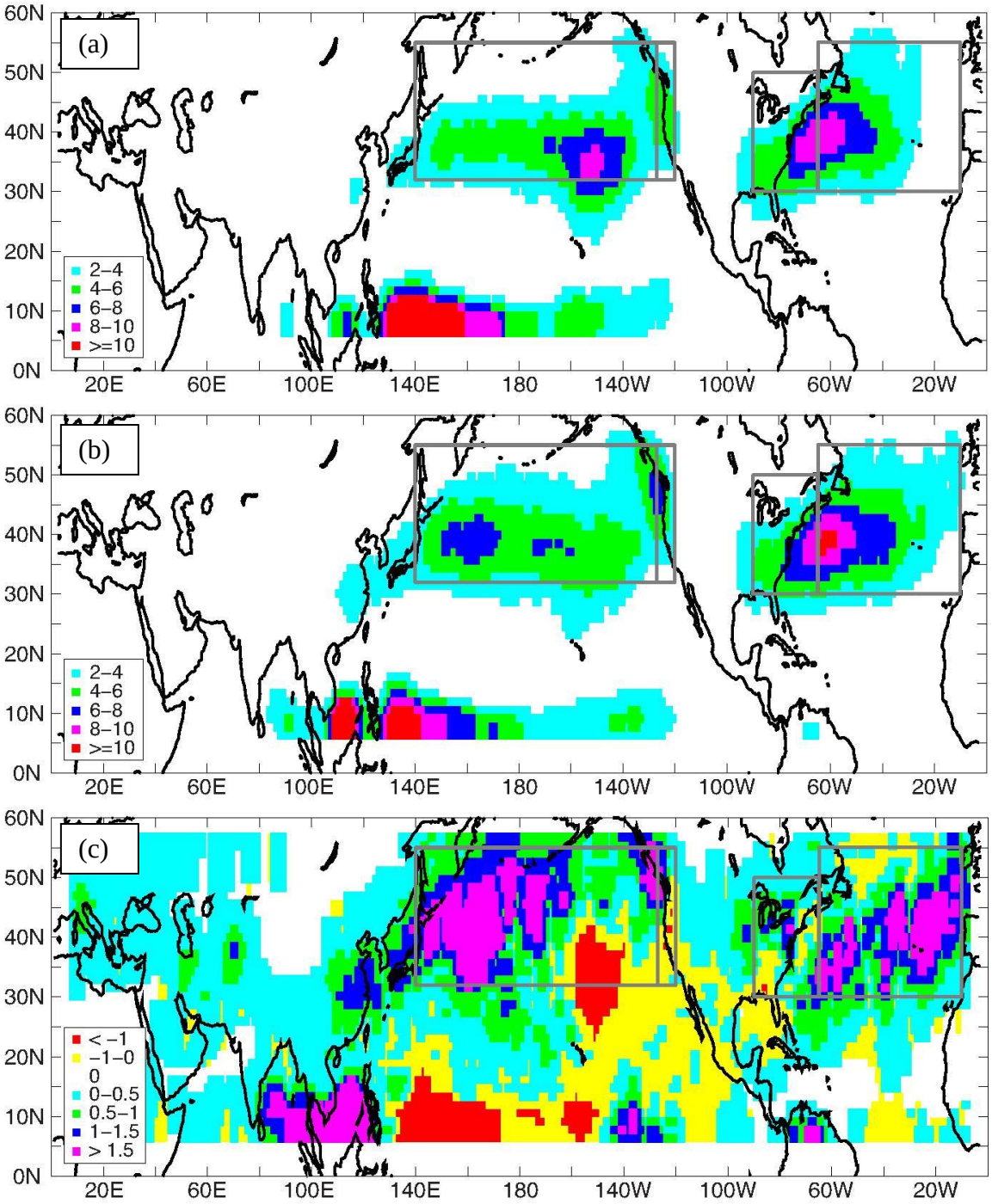

Fig. 4.10: As in Fig. 4.4, but for MIROC5 model.

Historical storm tracks are accurately captured by the MRI-CGCM3 model (Fig. 4.11a) when compared to observations and the other models shown here, although the region of high centroid density near the US West Coast extends a little too far south approaching California. End-of-century changes in the storm track steer more storms over California and eastern North America (i.e., probabilities of the most intense storms increase up to a factor of 5.5, Fig. 4.2). Meanwhile, significant decreases are shown over the central Pacific, and subtropical eastern Pacific. The Atlantic signal is more complex, but clear increases are seen over eastern North America.

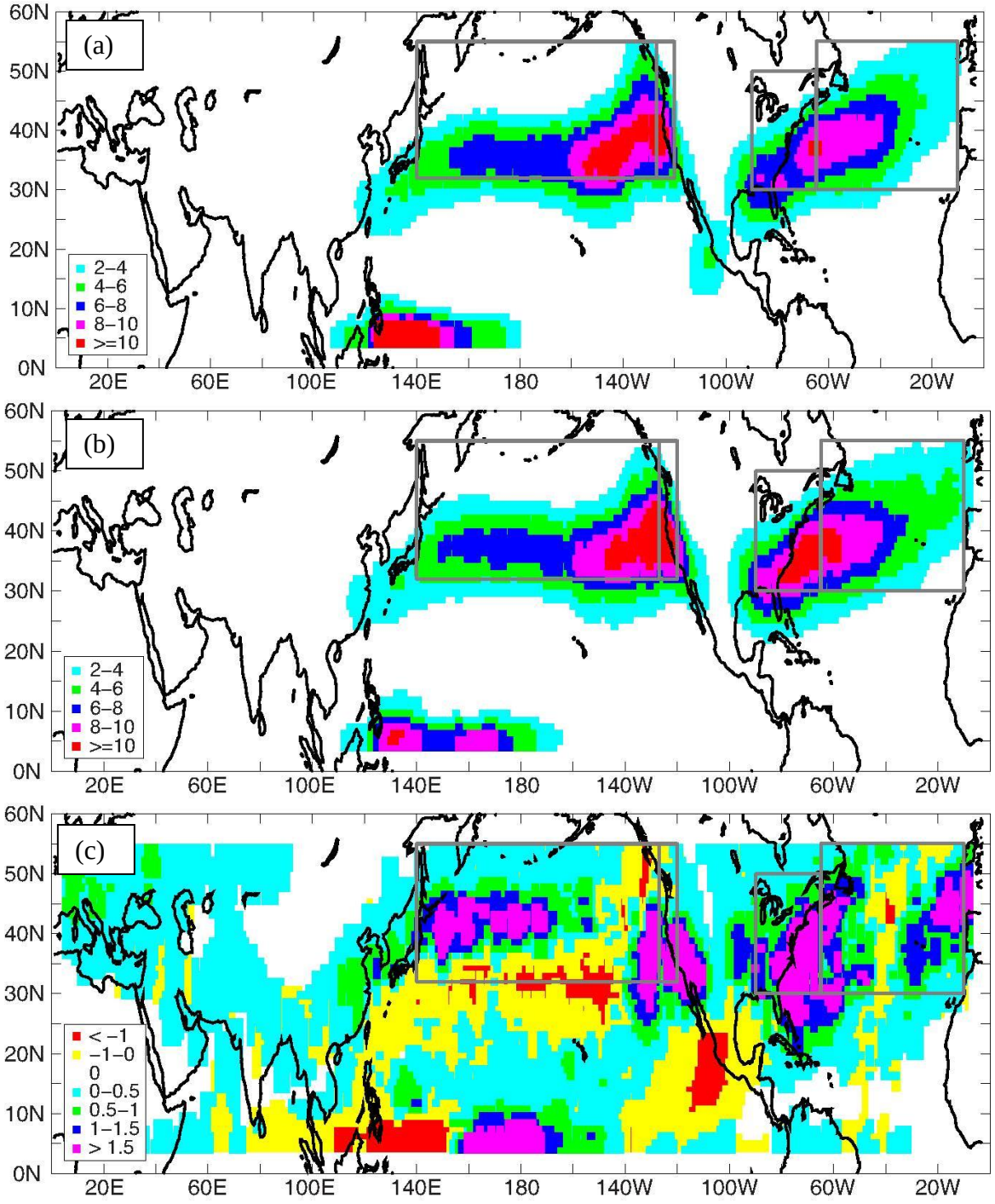

Fig. 4.11: As in Fig. 4.4, but for MRI-CGCM3 model.

Lastly, the NCAR LENS ensemble mean (Fig. 4.12a) appears to accurately simulate storm tracks in current climate compared to observations (Fig. 4.1b) and the models we analyze here. Centroid density maxima match with observations, and large positive changes in the number of high-power clusters north of 40^0N over the Pacific (up to a factor of 5.3, Fig. 4.2), over land along the West Coast (up to a factor of 4.2, Fig. 4.2), and over the eastern US, stretching across the Atlantic (up to a factor of 4.2, Fig. 4.2). Decreases in centroid density are seen over the subtropics.

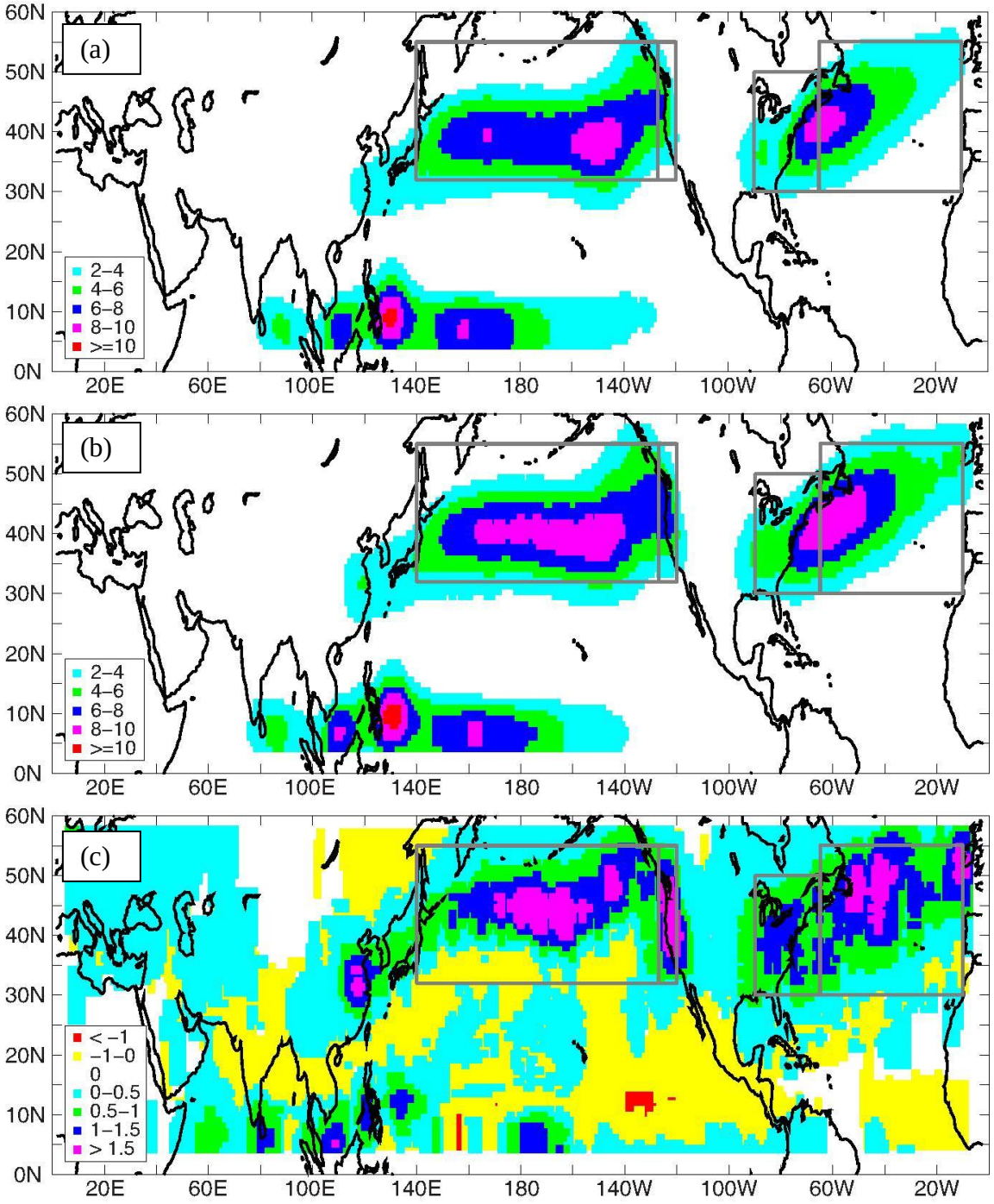

Fig. 4.12: As in Fig. 4.4, but for the ensemble mean of 10 members of NCAR LENS precipitation dataset.

4.5 Discussion

Probability distributions and spatial patterns of precipitation cluster power (defined here as the integrated mass of water released over a cluster per hour) are analyzed for boreal winter using TRMM-3B42 satellite precipitation data. We find that winter cluster power distributions, like their May-September Tropical counterparts in Chapters 2 and 3, also approximately follow a long, scale-free power law range, with a cutoff at high power and sharp decrease thereafter in the frequency of the most intense storms. The least-squares best-fit exponent over the power law range up to the cutoff is -1.48, similar to the -1.50 exponent noted in Chapter 2. The winter probability distributions have their cutoff near 10^{13} kg H_2O hr^{-1}. This is larger than a typical cutoff value for the Tropics of 1.4 x 10^{11} kg H_2O hr^{-1}. In mid-latitudes, a slight enhancement of probability density may be noted just prior to the cutoff, i.e., a hint of preferred scale, roughly corresponding to synoptic scale storms.

We then compare simulated cluster power probability distributions in recent climate to observations and evaluate changes in projected end-of-century distributions under RCP 8.5 as a measure of storm track changes under global warming, using precipitation data from the HIRAM, 7 coupled climate models from the CMIP5 experiment, and the ensemble mean of 10 simulations from the NCAR LENS project. For the historical period, all models qualitatively reproduce the shape and form found in observations, albeit with lower cutoff values near 2-3 x 10^{12} kg H_2O hr^{-1}. Cluster power distributions from each of the 10 LENS simulations of recent climate (using 16 year samples) and end-of-century climate (using 10 year samples) do not display much spread, suggesting that climate system internal variability is modest for decadal samples. With the exception of HIRAM, which has 10 years available for end-of-century, at least 26 years in the historical period and 20 years for end-of-century are used for evaluating

the models. Under RCP 8.5, there is a clear trend towards more frequent intense precipitation clusters, with probability density of extreme events increasing by up to a factor of 7.4 by end-of-century for the highest-power bin in the historical period for which statistics can be computed across all domains examined. Mean projected probability density increases for the highest-power bin range from a factor of 4.4 for the North Pacific, 3.4 for the West Coast, 3.5 for eastern North America, and 3.9 for the North Atlantic.

Annual seasonal mean centroid density maps (i.e., maps of the number of precipitation weighted centroids associated with precipitation clusters meeting the 10^{12} kg H_2O hr^{-1} threshold found within a certain distance of each grid cell) over the Northern Hemisphere illustrate the locations over which the most powerful precipitation clusters tend to congregate. In observations, the highest centroid density values and consequently, the most intense mid-latitude storms in this precipitation cluster metric are concentrated across the North Pacific between 25-50^0N from Japan to the western edge of North America, and from east of the Mississippi River, across the eastern seaboard of the United States, with a maxima along the Gulfstream. The concentration of powerful precipitation clusters in these regions aligns with typical mid-latitude storm tracks.

Maps of modeled annual seasonal mean centroid density, when compared with observations, characterize how well the models depict mid-latitude winter storm tracks and where the end-of-century projected increases in intense precipitation clusters noted previously occur. Each model qualitatively reproduces historical winter storm track locations, though there are some differences in how elongated the storm tracks are compared to observations as well as the number of precipitation clusters associated with each storm track. End-of-century and centroid density difference maps (i.e., differences between end-of-century and historical

yearly seasonal mean centroid density per grid cell) clearly indicate storm track shifts, with trends generally matching with a wet-get-wetter and dry-get-drier pattern and increases over each of the 4 regions investigated here. For the North American West Coast and eastern North America, there is a tendency for substantial increases in the number of high-powered precipitation clusters, as at least 8 of 9 models show higher centroid density values and frequency increases of the most intense storms up to a factor of 6.5 (as noted in their respective cluster power probability distributions). However, there is some variation in exactly where the storm track changes occur within these domains.

References

Austin, P. M., and R. A. Houze Jr., 1972: Analysis of the structure of precipitation patterns in New England. *J. Appl. Meteor,* **11,** 926–935.

Browning, K. A., and C. W. Pardoe, 1973: Structure of low-level jet streams ahead of mid-latitude cold fronts. *Quart. J. Roy. Meteor. Soc.*, **99**(422), 619–638, doi:10.1002/qj.49709942204.

Cayan, D. R., and J. O. Roads, 1984: Local relationships between United States West Coast precipitation and monthly mean circulation parameters. *Mon. Wea. Rev.*, **112**, 1276–1282, doi:10.1175/1520-0493(1984)112,1276:LRBUSW.2.0.CO;2.

Chang, E. K., C. Zheng, P. Lanigan, A. M. Yau, and J. D. Neelin, 2015: Significant modulation of variability and projected change in California winter precipitation by extratropical cyclone activity. *Geophys. Res. Lett.*, **42(14)**, 5983-5991.

Chen, J. H., and S. J. Lin, 2011: The remarkable predictability of inter-annual variability of Atlantic hurricanes during the past decade. *Geophys. Res. Lett.*, **38**, L11804, doi:10.1029/2011GL047629.

Chen, W. Y., and H. M. Van den Dool, 1997: Asymmetric impact of tropical SST anomalies on atmospheric internal variability over the North Pacific. *J. Atmos. Sci.*, **54**, 725–740.

Collins, M., and Coauthors, 2013: Long-term climate change: projections, commitments and irreversibility, in Climate Change 2013: *The Physical Science Basis. Contribution of Working Group I to the Fifth Assessment Report of the Intergovernmental Panel on Climate Change*, edited by T. F. Stocker et al., Cambridge Univ. Press, Cambridge, U. K., and New York.

Dacre, H. F., P. A. Clark, O. Martinez-Alvarado, M. A. Stringer, and D. A. Lavers, 2015: How do atmospheric rivers form? *Bull. Amer. Meteor. Soc.*, **96**, 1243–1255, doi:10.1175/BAMS-D-14-00031.1.

Dettinger, M. D., 2011: Climate change, atmospheric rivers, and floods in California—A multimodel analysis of storm frequency and magnitude changes. *J. Amer. Water Resour. Assoc.*, **47**, 514–523.

——, F. M. Ralph, T. Das, P. J. Neiman, and D. R. Cayan, 2011: Atmospheric rivers, floods and the water resources of California. *Water*, **3**, 445–478, doi:10.3390/w3020445.

Elliott, R. D., and E. L. Hovind, 1964: On convection bands within Pacific Coast storms and their relation to storm structure. *J. Appl. Meteor.*, **3**, 143–154, doi:10.1175/1520-0450(1964)003,0143: OCBWPC.2.0.CO;2.

——, ——, 1965: Heat, water, and vorticity balance within frontal zones. *J. Appl. Meteor.*, **4**, 196-211, doi: 10.1175/1520-0450(1965)004<0196:HWAVBI>2.0.CO;2.

Hall, N. M. J., B. J. Hoskins, P. J. Valdes, and C. A. Senior, 1994: Storm tracks in a high-resolution GCM with doubled carbon dioxide. *Quart. J. Roy. Meteor. Soc.*, **120**, 1209 – 1230.

Held, I. M. and M. Zhao, 2011: The response of tropical cyclone statistics to an increase in CO2 with fixed sea surface temperatures. *J. Climate*, **24**, 5353-5364, doi:10.1175/JCLI-D-11-00050.1.

——, S. W. Lyons, and S. Nigam, 1989: Transients and the extratropical response to El Nino. *J. Atmos. Sci.*, **46**, 163–174.

Hobbs, P. V., T. J. Matejka, P. H. Herzegh, J. D. Locatelli, and R. A. Houze, 1980: The mesoscale and microscale structure and organization of clouds and precipitation in midlatitude

cyclones. I: A case study of a cold front. *J. Atmos. Sci.*, **37**, 568–596, doi:10.1175/1520-0469(1980)037,0568:TMAMSA.2.0.CO;2.

Houze, R. A. J., and P. V. Hobbs, 1982: Organization and structure of precipitating cloud systems. *Advances in Geophysics*, Vol. 24, Academic Press, 225–315.

Huffman, G. J., and Coauthors, 2007: The TRMM multisatellite precipitation analysis (TMPA): Quasi-global, multiyear, combined-sensor precipitation estimates at fine scales. *J. Hydrometeor.*, **8**, 38–55, doi:10.1175/JHM560.1.

—— and D. T. Blovin, 2014: TRMM and other data precipitation data set documentation. Accessed 30 November 2015. [Available online at ftp://meso-a.gsfc.nasa.gov/pub/trmmdocs/3B42_3B43_doc.pdf.]

Kay, J. E., and Coauthors, 2015: The Community Earth System Model (CESM) large ensemble project: A community resource for studying climate change in the presence of internal climate variability. *Bull. Amer. Meteor. Soc.*, **96**, 1333–1349, doi:10.1175/BAMS-D-13-00255.1.

Kharin, V. V., F. W. Zwiers, X. Zhang, and G. C. Hegerl, 2007: Changes in temperature and precipitation extremes in the IPCC Ensemble of Global Coupled Model Simulations. *J. Climate*, **20**, 1419–1444, doi:10.1175/JCLI4066.1.

——, and M. F. Wehner, 2013: Changes in temperature and precipitation extremes in the CMIP5 ensemble. *Climatic Change*, **119.2**, 345-357, doi:10.1007/s10584-013-0705-8.

Kreitzberg, C. W., 1964: The structure of occlusions as determined from serial ascents and vertically-directed radar. *Rep. AFCRL-64-26*, Air Force Cambridge Research Laboratory, Bedford, MA, 121 pp.

——, and H. A. Brown, 1970: Mesoscale weather systems within an occlusion. *J. Appl. Meteor.*, **9**, 417–432, doi:10.1175/1520-0450(1970)009,0417:MWSWAO.2.0.CO;2.

Lavers, D. A., R. P. Allan, E. F. Wood, G. Villarini, D. J. Brayshaw, and A. J. Wade, 2011: Winter floods in Britain are connected to atmospheric rivers. *Geophys. Res. Lett.*, **38**, L23803, doi:10.1029/2011GL049783.

——, and G. Villarini, 2013: The nexus between atmospheric rivers and extreme precipitation across Europe. *Geophys. Res. Lett.*, **40**, 3259–3264, doi:10.1002/grl.50636.

——, D. E. Waliser, F. M. Ralph, and M. D. Dettinger, 2016: Predictability of horizontal water vapor transport relative to precipitation: Enhancing situational awareness for forecasting western U.S. extreme precipitation and flooding. *Geophys. Res. Lett.*, **43**, 2275–2282, doi:10.1002/2016GL067765.

Maloney, E. D., and Coauthors, 2014: North American climate in CMIP5 experiments. Part III: Assessment of 21st century projections, *J. Clim.* , **27**, 2230–2270, doi:10.1175/JCLI-D-13-00273.1.

Meehl, G., and Coauthors, 2007: Global climate projections. *Climate Change 2007: The Physical Science Basis*, S. Solomon et al., Eds., Cambridge University Press, 747–845.

Merlis, T. M., M. Zhao, and I. M. Held, 2013: The sensitivity of hurricane frequency to ITCZ changes and radiatively forced warming in aquaplanet simulations. *Geophys. Res. Lett.*, **40**, 4109-4114, doi:10.1002/grl.50680.

Nagle, R. E., and S. M. Serebreny, 1962: Radar precipitation echo and satellite cloud observations of a maritime cyclone. *J. Appl. Meteor.*, **1**, 279–295, doi:10.1175/1520-0450(1962)001,0279: RPEASC.2.0.CO;2.

Neelin, J. D., B. Langenbrunner, J. E. Meyerson, A. Hall, and N. Berg, 2013: California winter precipitation change under global warming in the Coupled Model Intercomparison Project phase 5 ensemble. *J. Climate*, **26**, 6238–6256, doi:10.1175/ JCLI-D-12-00514.1.

Nozumi, Y., and H. Arakawa, 1968: Pre-frontal rainbands in the warm sector of sub-tropical cyclones over the ocean. *J. Geophys. Res.*, **73**,487-492.

Peters, O., K. Christensen, and J. D. Neelin, 2012: Rainfall and Dragon-Kings. *The European Physical Journal Special Topics*, **205.1**, 147-158, doi:10.1140/epjst/e2012-01567-5.

Ralph, F. M., P. J. Neiman, G. A. Wick, S. I. Gutman, M. D. Dettinger, D. R. Cayan, and A. B. White, 2006: Flooding on California's Russian River: Role of atmospheric rivers. *Geophys. Res. Lett.*, **33**, L13801, doi:10.1029/2006GL026689.

——, and M. D. Dettinger, 2011: Storms, floods and the science of atmospheric rivers. *Eos, Trans. Amer. Geophys. Union*. **92**, 265–272, doi:10.1029/2011EO320001.

Seager, R., J. D. Neelin, I. Simpson, H. Liu, N. Henderson, T. Shaw, Y. Kushnir, and M. Ting, 2014b: Dynamical and thermodynamical causes of large-scale changes in the hydrological cycle over North America in response to global warming. *J. Climate*, **27**, 7921–7948.

Sillmann, J., V. V. Kharin, X. Zhang, F. W. Zwiers, and D. Bronaugh, 2013: Climate extremes indices in the CMIP5 multimodel ensemble: Part 1. Model evaluation in the present climate. *J. Geophys. Res. Atmos.*, **118**, 1716-1733, doi:10.1002/jgrd.50203.

——, 2013: Climate extremes indices in the CMIP5 multimodel ensemble: Part 2. Future climate projections. *J. Geophys. Res. Atmos.*, **118**, 2473–2493, doi:10.1002/jgrd.50188.

Stohl, A., C. Forster, and H. Sodemann, 2008: Remote sources of water vapor forming precipitation on the Norwegian west coast at 60°N - A tale of hurricanes and an atmospheric river. *J. Geophys. Res.*, **113**, D05102, doi:10.1029/2007JD009006.

Straus, D. M., and J. Shukla, 1997: Variations of midlatitude transient dynamics associated with ENSO. *J. Atmos. Sci.*, **54**, 777–790

Tebaldi C., K. Hayhoe, J. M. Arblaster, and G. A. Meehl, 2006: Going to the extremes: An intercomparison of model-simulated historical and future changes in extreme events. *Climate Change*, **79**, 185–211. doi:10.1007/s10584-006-9051-4.

Trenberth, K. E., 2011: Changes in precipitation with climate change. *Climate Res.*, **47**, 123–138, doi:10.3354/cr00953.

Tropical Rainfall Measuring Mission Project (TRMM), 2015: Daily TRMM and Others Rainfall Estimate (3B42 V7 derived), version 7. Goddard Space Flight Center Distributed Active Archive Center (GSFC DAAC). Accessed 01 July 2015. [Available online at http://disc.sci.gsfc.nasa.gov/datacollection/TRMM_3B42_daily_V7.html.]

Villarini, G., D. Lavers, E. Scoccimarro, M. Zhao, M. Wehner, G. Vecchi, T. Knutson, and K. Reed, 2014: Sensitivity of tropical cyclone rainfall to idealized global scale forcings. *J. Climate*, **27**, 4622-41, doi:10.1175/JCLI-D-13-00780.1.

Yin, J. H., 2005: A consistent poleward shift of the storm tracks in simulations of 21st century climate. *Geophys. Res. Lett.*, **32**, L18701, doi:10.1029/2005GL023684.

Zhao, M., I. M. Held, S. J. Lin, and G. A. Vecchi, 2009: Simulations of global hurricane climatology, interannual variability, and response to global warming using a 50-km resolution GCM. *J. Climate*, **22**, 6653-6678, doi:10.1175/2009JCLI3049.1.

——, ——, and G. A. Vecchi, 2010: Retrospective forecasts of the hurricane season using a global atmospheric model assuming persistence of SST anomalies. *Mon. Wea. Rev.*, **138**, 3858-3868, doi:10.1175/2010MWR3366.1.

——, ——, 2011: An analysis of the effect of global warming on the intensity of Atlantic hurricanes using a GCM with statistical refinement. *J. Climate*, **23**, 6382-6393, doi:10.1175/2010JCLI3837.1.

——, 2012: TC-permitting GCM simulations of hurricane frequency response to sea surface temperature anomalies projected for the late-twenty-first-century. *J. Climate*, **25**, 2995-3009, doi: 10.1175/JCLI-D-11-00313.1.